Department of Precision and Microsystems Engineering

Developing a microfluidic device incorporating submicron topographies for studying bone regeneration

Abhishek Sharma

Report no : MNE 2018.026
Coaches : Dr. L. Sasso, Dr. E.L. Apachitei
Professor : Prof. dr. U. Staufer
Specialisation : Micro and Nano Engineering
Type of report : Master thesis
Date : September 13, 2018

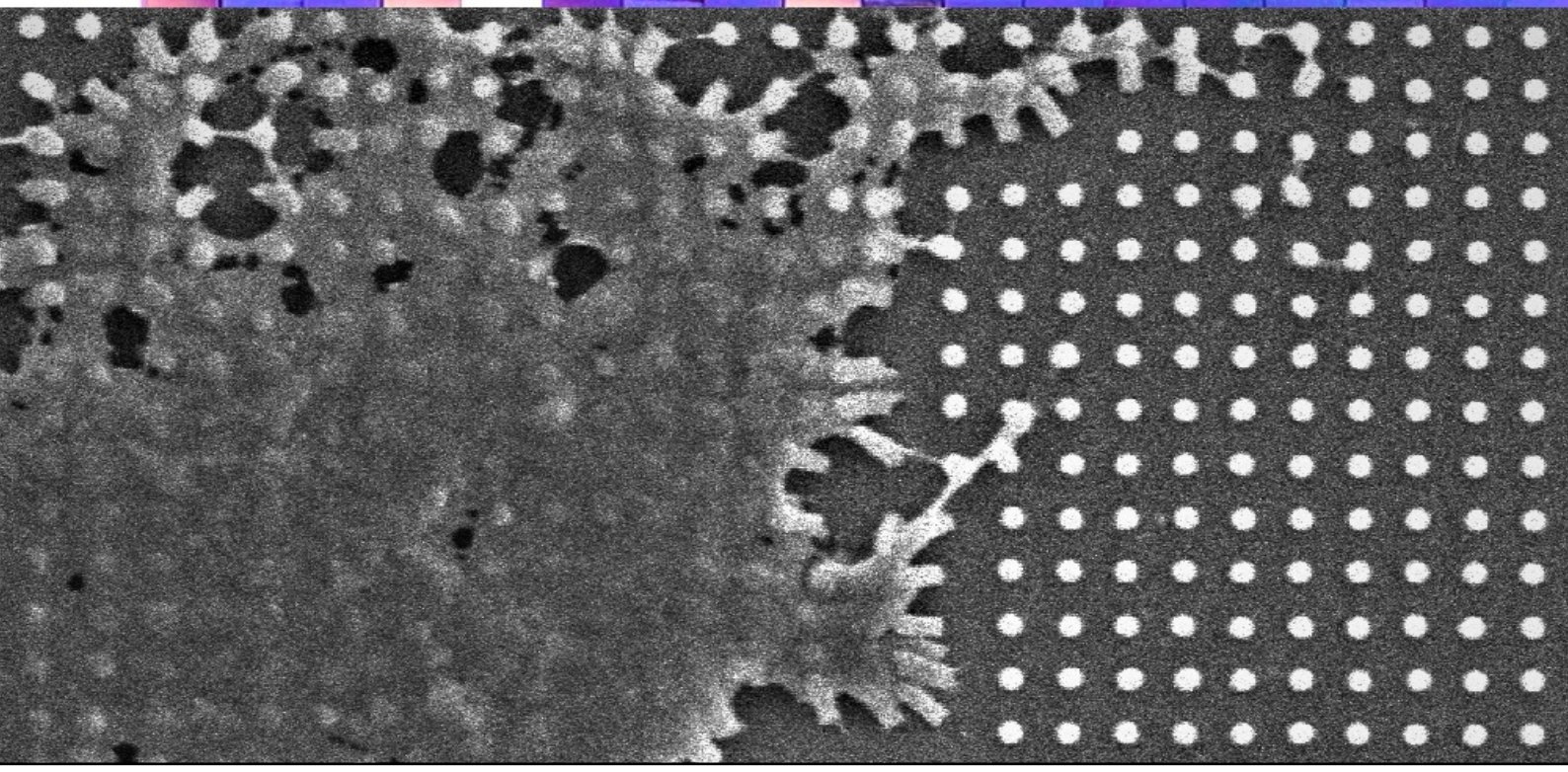

Developing a microfluidic device incorporating submicron topographies for studying bone regeneration

by

Abhishek Sharma

to obtain the degree of Master of Science
at the Delft University of Technology,
to be defended publicly on Tuesday September 13, 2018 at 13:00 PM.

Student number: 4589637
Project duration: September 4, 2017 – September 13, 2018
Thesis committee:

Prof. dr. U. Staufer,	3mE-PME, TU Delft, chair
Dr. L. Sasso,	3mE-PME, TU Delft, supervisor
Dr. E. L. Apachitei,	3mE-BME, TU Delft, supervisor
Prof. dr. A. van Keulen,	3mE-PME, TU Delft
Dr. M. Mastrangeli,	EWI-ECTM, TU Delft

An electronic version of this thesis is available at `http://repository.tudelft.nl/`.

TU Delft

Preface

Bone is a complex organ in the human body that possesses the ability to renew and remodel itself throughout lifetime. Fracture healing is the most common phenomenon where one gets to witness this regenerative capacity of the organ. However, not all fractures heal completely. For instance, 13% tibial fractures lead to an incomplete healing or reunion of the tissue. Severe injury, genetic factors, and bone diseases are known to inhibit full regeneration. Biomaterials that can allow and encourage new bone formation (osteogenesis) at the site of injury are currently being developed. Making these biomaterials as efficient as a natural bone is challenging and serves a major area for research today. Organ-on-Chip (OOC) based platforms, aim at mimicking the tissue microenvironment within a microfluidic chip to understand the factors that affect tissue regeneration. These are preferred owing to their small sizes, laminar flow of culture medium, high throughput, small reagent quantities used, and reduced dependency on animal studies.

Topography is one major factor that affects bone regeneration at macro, micro, and nano scales. Among these, submicron/nanotopography is known to affect regeneration down to sub/cellular level by activation of receptor-ligand type of interactions. Features of varying dimensions have been shown to induce osteogenesis with no optimal pattern being reported so far. Controlled multiscale topography is a key aspect of topographical microenvironment and poses a major challenge in terms of fabrication and upscaling. The two photon polymerisation (2PP) process allows producing topography of submicron size in a spatially and dimensionally controllable fashion. In comparison to the commonly used, mask based lithography techniques, the method can possibly allow producing multiscale features with ease. The 2PP method is typically known for fabricating micro-sized structures but remains unexplored for producing features in the submicron/nano scale.

This study aimed at creating uniform submicron pillar based topographies using the 2PP process and integrating them into a microfluidic device for studying their effect on bone regeneration. Upon identifying and adopting optimal materials (resin and substrate), feature writing strategy, and writing parameters the printed submicron patterns have been upscaled to the mm scale. A method for assessing the uniformity of these patterns was devised that can allow estimation of pillar dimensions. These topographies were also incorporated on the surface of 3D printed structures in a single step to demonstrate the possibility of multiscale printing using the 2PP process. Finally, the patterns were integrated in a Polydimethylsiloxane (PDMS) based microfluidic chip 3D printed using stereolithography. The pillars integrated in the microfluidic device showed no signs of delamination when they were subjected to varying flow rates, thus reinforcing their suitability for a dynamic cell culture. The patterns also increased the hydrophilicity of the substrate, an effect known to promote cell attachment. Preliminary experiments with human mesenchymal stem cells (hMSCs), dynamically cultured in these microfluidic devices and imaged for a period of up to 5 days, depicted a healthy, spread morphology with no major signs of cytotoxicity.

In conclusion, this study marks a step towards printing controlled submicron topographies using 2PP that can be upscaled (both spatially and dimensionally) and incorporated into biocompatible microfluidic chips. These devices can be used by biologists and engineers to systematically manipulate the cellular/tissue microenvironment and optimise it to achieve the 'ideal' regeneration conditions in the future.

Abhishek Sharma
Delft, September 2018

Contents

List of Figures vii

List of Tables ix

1 Introduction 3
- 1.1 The bone tissue . . . 3
- 1.2 The need for studying bone regeneration . . . 4
- 1.3 The remedy: Bone grafts . . . 4
  - 1.3.1 Natural grafts . . . 4
  - 1.3.2 Artificial grafts . . . 5
- 1.4 Conclusions . . . 5
- 1.5 Topography and bone regeneration . . . 6
  - 1.5.1 Nanotopography and its role . . . 6
- 1.6 Microfluidic devices for studying bone regeneration . . . 6
- 1.7 Conclusions . . . 9
- 1.8 Problem statement . . . 9
- 1.9 Methods for Micro/nanofabrication . . . 10
- 1.10 Conclusions . . . 12
- 1.11 Multi-photon polymerisation . . . 13
  - 1.11.1 Concept . . . 13
  - 1.11.2 Resolution control in 2PP . . . 13
  - 1.11.3 Setup . . . 14
  - 1.11.4 Materials . . . 15
- 1.12 Application of 2PP in cell-based studies . . . 15
  - 1.12.1 Conclusions . . . 16
- 1.13 Research goals . . . 18
- 1.14 Proposed approach . . . 18
  - 1.14.1 Topography production and characterisation . . . 18
  - 1.14.2 Topography upscaling and uniformity assessment . . . 18
  - 1.14.3 Fabricating the microfluidic device . . . 19
  - 1.14.4 Integrated device characterisation . . . 19
- 1.15 Milestones . . . 20
- 1.16 Risks . . . 20

2 Paper 23

3 Supplementary information 39
- 3.1 Enhancing the interface strength . . . 39
  - 3.1.1 Enhanced interface allows better surface detection . . . 39
  - 3.1.2 Pattern quality: Conventional to DiLL (fused silica) . . . 40
  - 3.1.3 Effect of ITO coating on fused silica glass . . . 40
- 3.2 Writing mode and tilt correction strategy . . . 41
  - 3.2.1 Transition from Galvo to Piezo writing mode . . . 41
  - 3.2.2 Tilt correction and its effect . . . 42
- 3.3 Parametric optimisation in DiLL mode . . . 43
  - 3.3.1 Scaling of pillar dimensions with writing parameters . . . 43
  - 3.3.2 Effect of writing parameters on pattern uniformity . . . 43

A Fabrication of topography **47**
A.1 Writing modes and configurations . . . 47
A.2 Conventional configuration . . . 47
A.2.1 Galvo writing mode . . . 47
A.2.2 Piezo writing mode . . . 48
A.3 DiLL mode . . . 50
A.4 New methods of enhancing interface amplitude . . . 50
A.5 Effect of temperature and humidity . . . 51
A.6 Varying pillar interspacing . . . 52
A.7 Measuring uniformity of patterned areas (and Image analysis) . . . 53
A.7.1 Image analysis in MATLAB . . . 54
A.8 Effect writing direction on pattern uniformity . . . 55
A.9 Effect of tilt correction method: Linear and Parabolic . . . 56
A.10 Effect of update rate. . . . 57
A.11 Large scale patterning on sheets . . . 57
A.12 Large scale patterning on scaffolds . . . 58
A.13 Viewing patterns under an inclined beam. . . . 59
A.14 Trying to mimick a controlled disorder pattern . . . 59

B Microfluidic device **61**
B.1 Mould design . . . 61
B.2 Clamp design . . . 61
B.3 Connections . . . 63
B.4 PDMS preparation . . . 63

C Preliminary Biological Studies **65**
C.1 Optical Imaging . . . 66
C.1.1 I: ITO coated fused silica . . . 66
C.1.2 N: Fused silica glass . . . 69
C.2 SEM Imaging . . . 74
C.2.1 I-T . . . 75
C.2.2 N-SH. . . . 75
C.2.3 IC, NC . . . 76
C.2.4 N-T . . . 76

D Nanoscribe Protocols **79**
D.1 Printing in Galvo mode: Parametric Sweep . . . 79
D.2 Printing in Piezo mode . . . 80
D.3 Tilt correction in Piezo mode . . . 81

E Other factors affecting bone regeneration **83**
E.1 Cell types involved . . . 83
E.2 Biomaterials . . . 84
E.3 Young's Modulus (E) . . . 86
E.4 Porosity . . . 86
E.5 Culture medium and growth factors . . . 87

F More about the 2PP process **89**
F.1 Concept. . . . 89
F.2 Tuning Young's modulus using 2PP . . . 89
F.3 Popular acrylate based resins used in 2PP. . . . 89

Bibliography **93**

List of Figures

1.1 Bone morphology at macro (a), micro (b) and nanoscale (c). Reproduced from [2] 3
1.2 Different cell types in the bone matrix. Reproduced from [9] 4
1.3 Steps involved in the bone fracture healing mechanism. Reproduced from [15] 4
1.4 A microfluidic device to study the effect of micro-dot topography on bone-regeneration. Reproduced from [45] 7
1.5 The distribution of energy absorption in the voxel during 2PP (referred to here as TPP) vs. single photon polymerisation (1PP). Note the dependence of energy on $(Intensity)^2$ for 2PP. Reproduced from [79] 13
1.6 Effect of laser power (LPE) on voxel size (a); and effect of exposure time (b) on the longitudinal and lateral size of the voxel. Reproduced from [81] 14
1.7 The setup for a two-photon polymerisation machine. Reproduced from [84] 14
1.8 The proposed process flow across various milestones (to the left of red brackets) for the study and the sub-tasks comprising each milestone. 21

3.1 Average interface detection error decreases with increasing signal amplitude 40
3.2 Increase in pattern uniformity upon transition conventional to DiLL configuration 41
3.3 Increase in pattern quality on using ITO coated fused silica (by about 15%) in comparison to a normal fused silica substrate 41
3.4 Increase in pattern quality due to the tilt correction in allowed Piezo mode while this is not the case in the Galvo mode. In figure (b), the sample has been corrected for tilt. 42
3.5 Variation in pillar dimensions at the stitching boundaries of pattern (printed via Galvo mode) with optical image in (a) and a zoomed in SEM image in (b). At boundaries, the Galvo scanner finishes scanning a particular block and starts printing a new one causing the pronounced variation in dimensions. 42
3.6 Selecting points for tilt measurement. All dimensions in mm 43
3.7 Increase in pattern quality on correcting the sample tilt. In this case, this is done for IP-Dip and ITO glass combination. 43
3.8 Parametric study of pillars with laser parameters 44
3.9 Parametric study of pillars dimension scaling with interface distance 44
3.10 Change in pattern optical image with laser power in Piezo writing mode. The change in pattern colour depicts a variations in pillar dimensions. For smaller pillar dimensions (towards right), the pattern uniformity decreases. 44
3.11 Decrease in pattern uniformity with increasing interface distance in Piezo writing mode 45

A.1 Varying pillar diameters as a function of laser power in the conventional mode (IP-L 780) for galvo and piezo writing 48
A.2 Distortion of pillars with increasing scan speed in Galvo mode during conventional wiriting . . 49
A.3 Variation in pillar diameters over larger areas in galvo writing mode and conventional configuration 49
A.4 Printing in DiLL mode using galvo and piezo modes 50
A.5 Printing on a layer of PVA using piezo writing method in DiLL configuration 50
A.6 Printing on substrate sputtered with a layer of Gold-Palladium mixture 51
A.7 Effect of temperature and humidity on patterning (DiLL mode, Galvo writing, LP = 9 mW and scan speed = 1000 μm/s) 51
A.8 Obtaining pillar dimensions via scaling from a high resolution image 55
A.9 Printing in DiLL mode using different writing directions 56
A.10 Linear versus parabolic tilt compensation 56
A.11 Effect of update rate on patterning in piezo mode (pulsed setting) 57
A.12 Effect of update rate on patterning in piezo mode (pulsed setting) 57

A.13 Effect of update rate on patterning in piezo mode (pulsed setting) 58
A.14 Writing patterns on sheets written in different directions 58
A.15 Upscaling patterns on a scaffold 59
A.16 Results obtained on trying controlled disorder pattern printing 59

B.1 Mould design used for the microfluidic study 62
B.2 Clamp design used for the microfluidic delamination study of pillars 63
B.3 PDMS removal damaging the pattern. Scale bar is 200 μm 64

C.1 Schematic of the PDMS channel used 65
C.2 Schematic of the sample (I and N) used for preliminary study. Sample N only could be bonded using air plasma 66
C.3 Delaminated scaffold reflecting a specific wavelength when submurged in the culture medium 66
C.4 Cells on pattern for sample I-T 75
C.5 Cells on sample N-SH 76
C.6 Increase in pattern quality correcting the sample tilt 76
C.7 Cell growth in sample N-T with erased pattern 77
C.8 Increased Cell concentration in inlet and outlet of channel 77

D.1 Parametric sweep in Galvo mode. The figures in left show 9 blocks with each block printed for different interface distances and slicing/hatching distances. The middle figure contains a zoomed in block where in the laser power and scan speed are varied within this block. The right figure shows individual pillar arrays printed for each of these parameters. 79
D.2 Parametric sweep in Piezo mode. The left images depicts blocks that are different from each other based on interface distance and repetition (to check for reproducibility). The images on the right show a zoom in of one of these blocks wherein the laser power and time of exposure are being varied. 80
D.3 Nanoscribe code generated 2 mm×2 mm pattern using stitching patterns over large area. This is done by printing a small area (sub-area) of 100 μm × 100 μm first. While printing this small constituent area, the piezo element is moved in x and y directions. To print a new sub-area, the stage is moved in x and y and the piezo element is brought back to the original (0,0,0) position. 81
D.4 Tilt measurement methodology. This firstly involved mapping 36 points and plotting them in Excel or MATLAB, as shown in (a,b). Then the variation of tilt angles is calculated along x for different ordinates and similarly along y for different abscissa (c,d). The average of these tilt values yield the tilt angles in$x$ and y directions. 81

E.1 Differentiation of Mesenchymal stem cells into different lineages. Reproduced from[54] 83

F.1 The effect of laser power on the material's Young's modulus (E). Reproduced from [164] 90

List of Tables

1.1 Mechanical properties of the cortical and cancellous bones. (Reproduced from [1]) 4
1.2 Major works carried out in the manufacturing of such microfluidic devices incorporating nanotopography 7
1.3 Commonly used methods for fabricating Nanotopographies 10
1.4 Comparing various topography fabrication techniques 12
1.5 2PP applications in Life-sciences based applications 15

3.1 Refractive indices of optical media in 2PP at 780 nm 39
3.2 Interface signal amplitudes and their scaling with difference in refractive indices $|\Delta n|$ 39
3.3 Correlating interface strength to the error in surface detection. The error measurement was performed twice. 40
3.4 Laser powers used for printing in Figure 3.10 44
3.5 Interface distance values used for printing in Figure 3.11 45

A.1 Patterns obtained at varying interspacings, interface distances, and laser parameters 53
A.2 Measuring pattern uniformities. The scale bar for each figure is 100 μm 53
A.3 Effect of writing direction on patterns shown in Figure A.9 56
A.4 Writing directions for sheets written in Figure A.14 58
A.5 Patterns observed under peripheral lighting condition of the microscope (IF = Interface distance) 60

C.1 Sample description for biological studies 65
C.2 Optical images of cells on galvo written flat sheets for ITO coated glass. Figures on the right depict the optical images of these features. 67
C.3 Optical images of cells on topography for ITO coated glass 68
C.4 Optical images of cells on control sample (without anything printed on it) for ITO coated glass . 69
C.5 Optical images of cells on sheet for fused silica glass 71
C.6 Optical images of cells on printed topography for fused silica glass 73
C.7 Optical images of cells on control area for fused silica glass 74

E.1 Different biomaterials and fabrication techniques for bone scaffolds 84

F.1 Commonly used 2PP resins 90

Acknowledgements

Many people helped me out during the project whether it be during the lab phase, planning, or even writing and organising my ideas. The thesis wouldn't have been possible in the form it is now without all these contributions. I want to thank my family, friends and colleagues for help inside and outside of the university. My coaches Luigi Sasso and Lidy Apachitei helped me shape the project since the very beginning until the very end. All the ideas, improvements, and help along the way was indispensable. Thanks to Paola Fanzio for training me on the Nanoscribe and helping out during the lab meetings. The biological studies in this project wouldn't have been possible without the help from people at Erasmus Medisch Centrum, Rotterdam. Thanks Bram van der Eerden, Shuan Zhang, Bastiaan Tuk, and Marijke Schreuders-Koedam for helping with the cell studies. I'd also like to thank Richard Pleeging for suggesting the initial idea for clamp making. Thanks to Cristina Varone, Eleonoor Verlinden,and Mahdiyeh Goushki for trainings and help with the lab equipment. The lab administrators Rob Luttjeboer, Spiridon van Veldhoven, Patrick van Holst, and Harry Jansen made all the lab work possible without delays. Lastly, thanks to all the members of the Polymer Microfabrication group and the Micro and Nano engineering group for the great ideas and discussions during the year.

1 Introduction

1.1. The bone tissue

The bone consists of two parts at the macroscopic scale: the outer *cortical bone* made up of bundled osteons stacked together and the inner *cancellous bone* made of a series of interconnected bone marrow filled trabeculae [1–3]. At the micro-scale, the tissue is made up of osteons consisting of layers of collagen fibres bundled as concentric cylinders around the Harversian canal containing blood vessels and nerves [2]. At the nanoscale, the collagen fibrils are located with a periodicity of about 67 nm and the collagen molecules within these fibrils at a gap of about 40 nm [2]. Nano-Hydroxyapatite crystals are embedded in these gaps between the collagen molecules [2, 3]. The trabecular bone is highly porous (50-90% porosity) [1, 4] while the cortical bone is only about 3-12% porous [1, 5, 6]. Fig.1.1 (reproduced from [2]) depicts the bone morphology at various length scales.

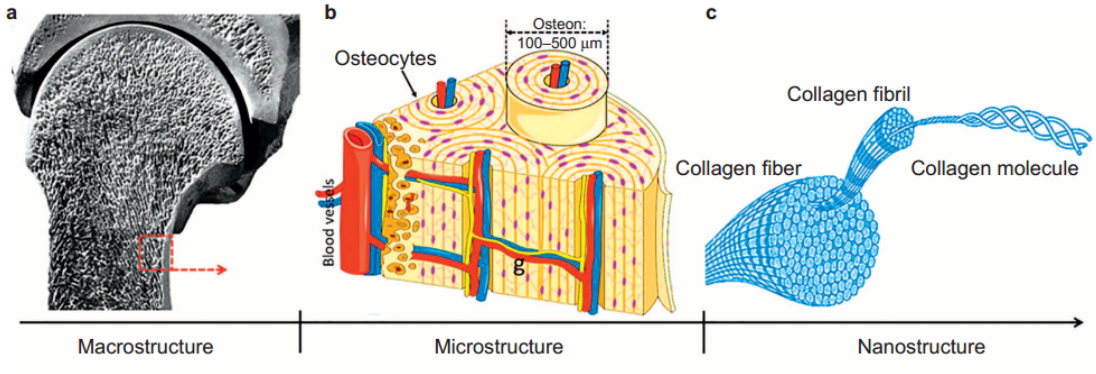

Figure 1.1: *Bone morphology at macro (a), micro (b) and nanoscale (c). Reproduced from [2]*

The 4 main types of cells (making up about 10% of the total volume) embedded in the bone matrix are the osteoblasts, osteoclasts, osteocytes and the bone lining cells [1, 3, 7]. The bone marrow in the trabecular region is the major source of Mesenchymal stem cells (MSCs) in the tissue. Osteoblasts are responsible for the bone formation and produce the extra-cellular matrix (ECM) [1, 3]. Osteoclasts are the multinucleated cells responsible for the resorption of bone while osteocytes are responsible for the mechanical sensing of load and micro-fractures [1, 3]. Bone lining cells are found in the inactive or non-remodelling part of the bone [7]. The main bone cell types haven been depicted in fig. 1.2. The ECM is composed of an organic part consisting of Collagen type 1 (90% of organic phase) along with traces of other non-collagenous proteins (5%) while the inorganic part is made up of hydroxyapatite crystals that provide toughness and strength to the tissue [3, 8]. The mechanical properties of the bone are summarised in table 1.1

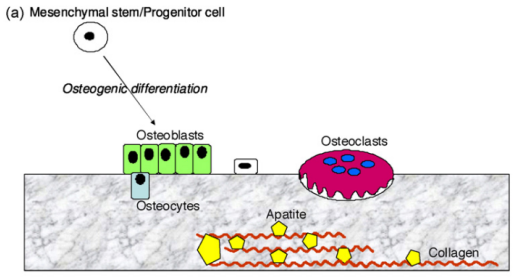

Figure 1.2: *Different cell types in the bone matrix. Reproduced from [9]*

Table 1.1: *Mechanical properties of the cortical and cancellous bones. (Reproduced from [1])*

Property	Cortical bone	Cancellous bone
Compressive strength (MPa)	100-230	2-12
Tensile strength (MPa)	50-150	20-30
Young's modulus (GPa)	7-30	0.05-0.5

1.2. The need for studying bone regeneration

The bone is one of the organs in the human body that possesses the ability to renew and remodel itself throughout lifetime [10]. It is interesting to know that most bone injuries heal themselves without the formation of a scar/fibrous tissue, thus restoring them to normalcy [10–12].The typical fracture healing mechanism begins with inflammation and formation of hematoma leading to the recruitment of MSCs towards the site of injury [12]. This is followed by angiogenesis, chondrogenesis, and osteogenesis as the MSCs differentiate into the osteogenic lineage [12, 13]. The next phase involves a soft callus formation which hardens as it matures [12, 13]. The bone thus begins to mineralise and remodel in the final stage of fracture healing [12].The schematic of the bone healing mechanism is shown in fig1.3. The bone tissue keeps renewing and dissolving based on its environment and location. Fracture healing is the most common phenomenon where one gets to witness this regenerative capacity of the tissue. However, not all fractures result in a complete reunion. About 13% of tibial fractures for example, lead to incomplete or insufficient reunion especially in cases where the injury is severe and requires large amounts of bone regeneration [10, 14]. Various bone diseases such as avascular necrosis, osteoporosis, fibrous dysplasia, infections or those caused due to genetic factors also require bone regeneration that can't be naturally corrected by the body [1, 2, 10]. Cases such as these would thus need external aid/treatments to overcome complications and restore full functionality of the tissue.

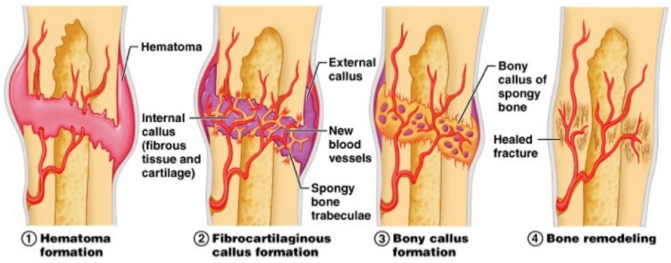

Figure 1.3: *Steps involved in the bone fracture healing mechanism. Reproduced from [15]*

1.3. The remedy: Bone grafts

1.3.1. Natural grafts

The current methods applied to augment bone regeneration involve bone grafts. Autologous bone grafts are taken from another part of the patient's body and transplanted at the site of injury [1, 10, 13]. There is a limited risk of infection but leaves the patient with two injuries to heal instead of one [1]. Allogeneic bone grafts involve the use of a bone sample from another human but leads to chances of rejection, infection and transmission of diseases [10, 13]. Xenogeneic bone grafts are derived from another species such as bovines

and thus pose a higher risk of rejection and infection than its allogenic counterpart [16].

1.3.2. Artificial grafts

Artificial bone graft substitutes are currently one of the most commonly used methods today owing to the ease of tuning their properties and a lower risk of infection or rejection [1–3, 10, 13]. They can be composed of natural as well as synthetic biomaterials. The former includes biomaterials such as collagen, chitosan, silk and elastin. while the latter can include metals (such as Titanium and Tantalum), polymers (such as Polycaprolactone, Polylactic acid, polyglycolic acid), ceramics (such as bioglass, Calcium Phosphate, corals) and composites (such as Calcium Phosphate-Polyester composites) [3, 9, 10]. These artificial graft biomaterials acts as scaffolds for the bone-cells and provide the necessary physical and bio-chemical cues for bone-growth and(or) osteogenesis [2, 3]. An ideal bone substitute material should be:

- *Bio-inert:*
  In a sense that it is not cytotoxic and does not elicit an unwanted foreign body response in the organ environment. This is a basic requirement for any biomaterial to be used as a graft material, *in-vitro* or *in-vivo* [3, 17]

- *Osteoconductive:*
  These biomaterials allow the bone-cells to grow and proliferate on their surface. Titanium for example, also used widely as a bone implant material, is known to promote bone growth. The main requirement here is to provide a surface for attachment of cells and extra-cellular proteins [3, 13, 18].

- *Osteoinductive*:
  These biomaterials induce osteogenesis and thus encourage immature cells (progenitor cells and stem cells) to differentiate into the osteogenic lineage [3, 13, 18].

1.4. Conclusions

- The *Gold standard* for bone-regeneration is thus an autologous graft since it meets all the above requirements simultaneously [10, 19–23]. Fabricating a graft is thus challenging and combines expertise in biology, chemistry and engineering.

- Osteoconductive biomaterials supplemented with appropriate osteoinductive growth factors, stem/progenitor cells and other physical/biochemical cues are thus being researched today [3, 24] to realise the so called *Diamond concept* to regenerate the bone tissue and support vascularisation [1, 10].

- The real challenge however, lies in making these bone-substitute biomaterials as efficient as their gold counterpart: the autograft [10, 19]. Bringing the diamond standard at par with the gold one requires the study of various factors that affect bone regeneration and constitute its microenvironment so that these can be modelled into a test device.

1.5. Topography and bone regeneration

In general, topography (at various scales) affects cell attachment, morphology, proliferation, differentiation and migration [25–27]. Macro, micro as well as nanotopographies can influence the regeneration phenomenon [28]. Macrotopography (above 100 μm) [26], Microtopography (0.1-100 μm) [29, 30]and Nanotopography (1-100 nm) influence the cells at colony, individual and ligand/proteomic levels respectively [31]. It can thus be understood that macro and micro topographies and geometries allow accumulation of cells or "*pile-up*" thus leading to the formation of bone nodules in selective areas while nanopatterns can allow molecular interactions when spacings are below a certain threshold value [26, 32]. Thus macrotopography can be used to tune the bone shape and vascularisation while the microtopography could regulate cell morphology, attachment, proliferation and arrangement (by providing physical cues/geometries for arrangement) and nanotopography can influence ligand and protein arrangements [28].

1.5.1. Nanotopography and its role

It is interesting to manipulate the bone regeneration mechanism using nanotopography since this would help in understanding the molecular interactions within the cell in the near future. Nanotopographical features ranging over 17-25 nm[33] to 100 nm or more (nanotube diameter) [34] have shown to induce osteogenesis. There isn't an optimal nanopattern for bone regeneration in literature that can be used for inducing osteogenesis due to highly scattered findings which further necessitates it's study in a systematic manner. Incorporating such nanoscale features into a microdevice would require *multi-scale manufacturing approaches* while aiming at cutting down costs and manufacturing times simultaneously [35]. It has been found that nanotopography plays a major role in deciding the fate of the stem cells (differentiation) and their behaviour [31]. Dalby et al. for the first time showed that a controlled disorder of nanotopographical features led to an enhanced osteogenic differentiation in comparison to a flat or an ordered square feature arrangement in absence of any osteogenic medium [36]. The cells showed large focal adhesion sizes, an organised cytoskeleton and a polygonal shape. Typical methods employed for generating such nanopatterns include nanoimprinting using moulds fabricated via beam based lithography, mask anodization, physical vapour deposition and electron beam evaporation [36–44]. Some of these have been discussed later in section 1.9.

Dobbenga et al. drew some important conclusions in their review; pointing out that at about 15 nm pillar height, the maximum expression of osteogenic markers is observed [31]. The cell attachment in these cases was characterised by a long and dense network of filopodia. An interesting observation made is the consistency in these results independent of the substrate material used. It would therefore be interesting to study the effect of different biomaterials using the same topography. They also pointed out that there is not enough data on the effect of nanopillar diameter or the nanopit depth on osteogenic differentiation. A spacing of less than 70 nm in the nanopattern is usually needed to induce clustering and osteogenesis on the substrate [2, 26]. The effect of nanotopography feature size in presence of osteogenic media (such as Dexamethasone and β-glycerophosphate) as well as comparing osteogenesis for different substrate biomaterials with similar topography also needs to be researched thoroughly.

1.6. Microfluidic devices for studying bone regeneration

In place of conventional cultures, the use of microfluidic devices to study the fracture healing mechanisms has been growing over the years and forms a part of the broader Organ-on-a-chip (OOC) concept. An OOC system uses a microfluidic platform to culture living cells while attempting to simulate the tissue or organ level physiology [46]. These have been developed for an array of applications such as drug screening, stem cell differentiation, tissue engineering, immunology, separating different cell types, studying functionalised surface and the like [47]. Microfluidic models are chosen in such studies owing to their small feature sizes leading to laminar flows, being able to closely monitor and control the cell microenvironment (bio-chemical as well as physical), high throughput allowing multiple experiments on the same chip, the use of small reagent quantities and cell aspirate volumes (and thus the ease of obtaining them), the ability to create a dynamic or static culture environment (a choice which is not available in a conventional cell culture), allowing real-time imaging and reducing dependency on animal studies [45, 47, 48]. An ideal microfluidic device should fulfil the following basic criteria:

1. Biocompatibility
2. Allows conveniently adding/flushing out different media, vary flow rates etc.

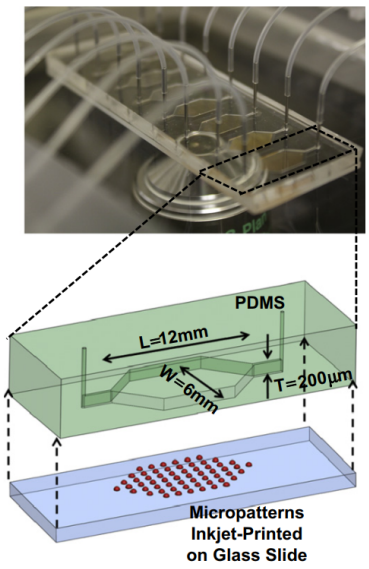

Figure 1.4: *A microfluidic device to study the effect of micro-dot topography on bone-regeneration. Reproduced from [45]*

3. Is Leak proof
4. Allows imaging of cells conveniently
5. Is Easy to fabricate and assemble

A typical microfluidic device for bone-regeneration is shown in Fig.1.4 and reproduced from [45]. Here, micropatterns fabricated via inkjet printing were used to study bone regeneration. This can act as a model design for the current bone regeneration study. In the last decade, there has been quite a lot of research done on microfluidic cell cultures that incorporate micro and nanopatterned substrates to mimick the micro/nanotopographical microenvironment. Table 1.2 summarises some of the works depicting the use of microfluidic devices integrated with micro/nanofabricated features for cell based studies. These can pave the way in realizing such a device for studying bone regeneration and simulating the various factors involved in it. For example, Lee et al. reported mineralised 3D bone tissue formation (after day 16) in their microfluidic device in presence of osteogenic media (DEX and glycomethasone) wherein the osteoblasts first spread all over the base (day 4) of the device and then began migrating to the top and side walls (day 7) [45].

Table 1.2: *Major works carried out in the manufacturing of such microfluidic devices incorporating nanotopography*

Pattern and fabrication	**Channels and fabrication**	**Application**	**References**
50 nm diameter, 400 nm high pillars and 50 nm wide, 200 nm high grooves with 200 nm pitch Poly Urethane Acrylate Nanopillars fabricated via UV assisted Capillary moulding	PDMS microchannels 550 μm wide, 40 μm high. Sealing with Oxygen plasma treatment	Separating cancer and healthy cells	[48]

Table 1.2 – *Continued from previous page*

Electron beam lithography to create a PMMA master mould with nanogratings of 350 nm width, 700 nm pitch, and 280 nm depth followed by soft lithography using PDMS. Different PDMS nanopatterns stitched onto a common PDMS layer.	Microchannels 2 cm long, 500 μm wide, 53 μm deep via photolithography and soft lithography/ mould replication. Bonding the channel layer onto the substrate layer via "Stamp and Stick" method	Studying adhesion, spreading and migration of human mesenchymal stem cells	[49]
Silica nanobeads of diameters 100-1150 nm deposited onto a glass coverslip.	PDMS microchannels of length 14 mm, width 4 mm and height 50 μm produced via photolithography of SU8 onto Silicon followed by replica moulding using PDMS. Channel and substrate layers bonded using oxygen plasma treatment	Capturing CD4+ T cells onto functionalised surfaces under continuous flow	[50]
50 μm dots separated by 150 µm via inkjet printing on a glass slide	Microchannels 200 μm deep, 800 μm wide, 6 cm long on PDMS by Photolithography on Silicon wafer followed by soft lithography replica moulding; oxygen plasma treatment to bond substrate to channel layer	Studying the effect of an antibiotic drug on osteoblasts in presence of bacteria	[45]
20 nm diameter pores, 50 nm deep fabricated via anodization of pure aluminium	Microchannels 70 μm deep, 1 cm long, 1000 μm wide in PDMS fabricated via photolithography on Silicon followed by Soft lithography mould replication; the two layers pressed together	Monitoring protein binding to lipid layers	[51]

Table 1.2 – *Continued from previous page*

Nanopits (500*500 nm- 1*1 μm pits, 1-2 μm apart) arrays using Electron beam lithography followed by Reactive ion etching for passing pattern onto fused silica substrate	Nanochannel (100 nm deep, 450 μm long, 50 μm wide) using UV contact lithography and etching; cover with fused silica chip by quartz-quartz bonding	Pressure driven transport of DNA molecules	[52]

1.7. Conclusions

- Realising the diamond concept of bone regeneration to be able to heal severe bone injuries or diseases more efficiently would be highly dependent on an understanding of the effect that topography plays at the cellular level.
- The main aim is to generate submicron and nanostructures in order to probe the effect of substrate topography at the cellular or molecular level. This size range has also been chosen to fill in the research gaps and establish a trend for the effect of feature size on cell behaviour.
- The submicron and nanoscale features affecting bone regeneration when integrated into microfluidic cultures, can help effectively mimick the tissue microenvironment. Microfluidic environments help reduce reagent quantities needed, ensure a laminar flow, involve small feature sizes, and reduce dependency on animal studies.

1.8. Problem statement

The aim of this study is to design and fabricate such a submicron/nanoscale topography-integrated microfluidic device which can be used by biologists to study the fracture healing (bone regeneration) microenvironment. The device can further help researchers identify the optimal feature sizes that can encourage osteogenesis. The fabricated devices may also be modified to incorporate additional factors (such as substrate Young's modulus, multiscale topographies, different cell types, 3D porosities, growth factors etc.) in the future. Numerous challenges such as selecting appropriate materials and methods for topography, microfluidic device, and the method of device assembly need to identified and solved while meeting the device requirements stated in section 1.6.

1.9. Methods for Micro/nanofabrication

As discussed in section 1.5, topography plays a key role in influencing the stem cell behaviour. The bone regeneration based microfluidic cell culture device would need a topography that

1. Is highly controllable (size, layout, geometry)
2. Is of submicron/nanoscale dimensions
3. Is easy to pattern on large areas (upscalable)
4. Is biocompatible
5. Involves reasonably low fabrication times
6. Can be prototyped rapidly
7. Does not entail very high fabrication/processing costs

An array of techniques have been developed for fabricating submicron/nanoscale patterns and features for semiconductor, biomedical or microfluidic applications. A number of works list the fabrication techniques employed for fabricating such features and their application in cell culturing based studies [49, 53–57]. Table 1.3 lists these techniques, the basic principle behind them, the typical resolution, their advantages and shortcomings.

Table 1.3: *Commonly used methods for fabricating Nanotopographies*

Technique	**Method Description**	**Resolution**	**Advantages**	**Drawbacks**	**References**
Electron beam lithography (EBL)	Directing high energy electron beam onto a resist (PMMA for example) followed by transfer of the pattern into the substrate	Sub 5 nm (3-5 nm linewidth recorded in PMMA resist; 2 nm feature size with 10 nm pitch in Hydrogen Silsesquioxane resist)	Very high resolution; wide variety of shapes possible; controlled topographies	Expensive equipment; low throughput (in case of maskless production); masked features are not truly 3D	[58, 59]
Nanoimprint lithography (NIL)	Mould preparation using Electron beam lithography or Reactive ion etching followed by imprinting into thermoplastic resin	Sub 10 nm (6 nm holes recorded)	High replicability; low cost (only for the imprinting step)	Need for a master mold that entails high cost; not a truly 3D method	[60, 61]
Multi-photon polymerisation (MPL)	Using multiple photons to excite the atoms to excite atoms in a resin leading to polymerisation reaction	100 nm but sub 50 nm with improved focusing and scanning equipment recorded	High resolution; truly 3D features produced; high scan rate possible over larger areas	Slower than techniques such a NIL and beam based lithography (with masks); lack of variety in photoinitiators	[62–64]

Table 1.3 – *Continued from previous page*

Anodization	Certain pure metal (such as Ti, Al) undergoes anodization reaction to form a nanoporous oxide layer which can be used as a template itself or be functionalised and deposit other materials	10 nm pore diameters	High resolution; low costs involved; no sophisticated equipment needed	Lack of control over topography shape and order	[65]
Colloidal Lithography (CL)	Using a layer of colloidal particles on a substrate an etching or deposition mask (in combination with chemical etching, sputtering, reactive ion etching etc.)	Sub 100 nm	Large area patterning possible; Inexpensive; Easy replication	Lack of control over topography geometry and spatial arrangement; difficulty in producing colloidal particles of required size and shape as well as their storage	[66, 67]
Focussed Ion Beam Lithography (FIB)	Using a beam of Ions (from Hydrogen, Helium, Gallium etc.) onto a substrate (with or without a mask) to implant ions, remove material or locally add material via Chemical vapour deposition; PMMA is the commonly used resist	5 nm feature size, spacing of 20 nm	Better resolution than EBL as backscattering is negligible	Expensive equipment and low throughput in case of direct writing method; expensive masks	[68, 69]
Polymer demixing	Blend of polymers undergo phase separation when spin coated onto a substrate followed by annealing	Islands of PMMA that are sub 50 nm high	High resolution; high throughput; low costs	Control over topography is limited; not for 3D patterns	[70]
Photolithography (PL)	Using low wavelength light to shine through a photomask onto a photoresist followed by development	$1-2\mu m$ but below 400 nm using additional changes/lower wavelengths	High throughput, popular for semiconductor processes	Low resolution using conventional instrumentation; expensive masks; true 3D shapes not viable	[67]

Table 1.3 – *Continued from previous page*

Scanning-Probe Lithography (SPL)	Individual addition or removal of atoms/molecules to/from the substrate using Atomic force microscope (AFM) or Scanning tunnelling microscope (STM) tips	Less than 1 nm to transfer individual atoms using STM; 50 nm using AFM tip for transferring group of molecules or nanoparticles (Dip Pen Lithography)	Extremely precise pattern generation; patterning variety of materials; manipulation as well as imaging using the same instrument	Extremely low throughput; expensive and sophisticated equipment/ environment	[69, 71]
X-Ray Lithography (XL)	Using X-rays to pattern a substrate with or without a mask and a resist layer	30 nm	High resolution (better than Optical lithography)	High equipment cost; expensive masks and low throughput for maskless process; Masked method does not allow truly 3D structures	[72, 73]
Block Copolymer Lithography (BCL)	Self-assembly of copolymer layers followed by physical and chemical treatments	sub 10 nm	High resolution; low production times and costs; simple instrumentation	Lack of variety and control over patterns; 3D shapes difficult to produce	[71, 74]

1.10. Conclusions

Multiphoton polymerisation meets the above mentioned topographical requirements to an appreciable extent; most importantly due to the ease of controlling and varying the topography geometry, size, spatial arrangement and material's mechanical properties (to an extent) conveniently. Even though the process may not be as fast as NIL or beam based methods, it is quicker in terms of producing large varieties of batches. Self assembly methods are insufficient when it comes to topography control, property tuning and producing truly 3D structures. Hence multiphoton polymerisation (2 Photon Polymerisation in most cases) shall be employed for fabricating the submicron/nano features. The different techniques have been compared in table 1.4. It can be seen that 2PP outperforms the other techniques overall.

Table 1.4: *Comparing various topography fabrication techniques*

Technique	**Resolution**	**Topography control**	**3D structure fabrication**	**Time**	**Large area patterning**	**Cost**
Beam based process (EBL, XL, FIB, PL)	++ (EBL, FIB); - (XL, PL)	+ +	-	- (maskless); + + (masked)	- - (maskless); + + (masked)	- -
NIL	+	+ +	-	+ +	+ +	+ +
MPL	+	+ +	+ +	+	+	+
Self assembly (Anodization, Polymer demixing, BCL, CL)	+ +	-	-	+	+ +	+ +
SPL	+ +	+ +	-	- -	- -	- -

1.11. Multi-photon polymerisation

1.11.1. Concept

Multi-photon polymerisation, also called direct laser writing or maskless writing involves the use of a mode locked near infrared femtosecond laser to focus multiple ultrashort pulses of photons (usually two, hence called *two-photon polymerisation* and referred to as 2PP henceforth) onto a photo-sensitive material [75–77]. The material (a photoinitiator) is usually sensitive to wavelengths in the ultraviolet region (around 400 nm) and undergoes a polymerisation reaction in the exposed regions. This photoresist material may become soluble or insoluble (and thus called positive or negative resist respectively) with respect to the developing agent. The method is usually used to reach feature sizes much below the diffraction limit of light, up to sub 100 nm resolution and thus can be considered superior to similar printing technologies such as UV-stereolithography, inkjet printing and laser sintering in this respect. Today 2PP is being employed in an array of applications such as bioengineering, photonics, microfluidics and metamaterials [75, 78, 79].

The non-linear interaction of the laser with resist material results in the polymerisation occurring only in the focal spot volume rather than along entire path of the beam, as in the case of single photon polymerisation [77]. The energy absorbed in 2PP is proportional to the square of the beam intensity and obeys Gaussian distribution with respect to the position (r) from the centre of focus according as shown in figure 1.5. There is a threshold energy (in the order of a few *nJ*) to polymerise the material. The shaded area in figure 1.5 receiving energy above this value represents the polymerised volume. Too high energies may however lead to boiling-off of the resin [77]. The focal volume (or $voxel$) is an ellipsoid with the axial (AXR) and lateral resolutions (LR) expressed via equations 1.1 and 1.2 respectively.

$$AXR \propto \sqrt{\frac{I_0}{I_{th}} - 1} \tag{1.1}$$

$$LR \propto \sqrt{ln\left(\frac{I_0}{I_{th}}\right)} \tag{1.2}$$

Here I_0 and I_{th} represent the maximum and threshold intensities respectively.

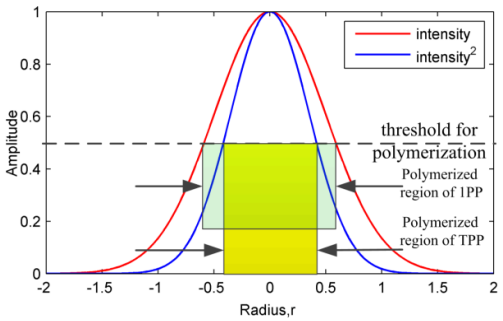

Figure 1.5: *The distribution of energy absorption in the voxel during 2PP (referred to here as TPP) vs. single photon polymerisation (1PP). Note the dependence of energy on* $(Intensity)^2$ *for 2PP. Reproduced from [79]*

1.11.2. Resolution control in 2PP

The voxel diameter increases with increasing power, pulsewidth and exposure time (controlled using the scanning speed or the shutter) while an opposite effect is seen for the increasing numerical aperture of the objective lens [77, 80]. This effect can be employed to achieve small feature sizes however, the structures become susceptible to laser fluctuations and lose strength at low laser powers [63, 75]. Structural shrinkage and repolymerisation of the resin from close by structures due to thermal effects have also been employed to produce smaller features [62]. The axial feature size is more than the lateral one due to the ellipsoid shape of the voxel undergoing shrinkage [63, 77]. Adding of a quenching molecule to the resin or using a more sensitive resin with lower threshold energy also helps in providing a better(smaller) resolution but may affect the strength of the fabricated structure due to insufficient crosslinkage [75, 78, 79]. The effect of laser power and time of exposure on the size of voxel is shown in Figure 1.6.

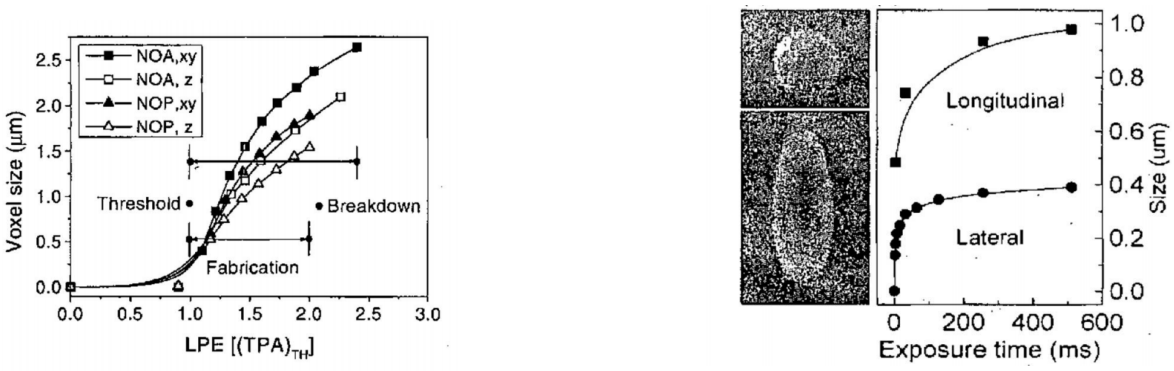

Figure 1.6: *Effect of laser power (LPE) on voxel size (a); and effect of exposure time (b) on the longitudinal and lateral size of the voxel. Reproduced from [81]*

.

1.11.3. Setup

The setup for 2PP usually involves a Titanium Sapphire based femtosecond laser (also to be used in this study, from Nanoscribe GmbH, Germany) operating in the near infrared region of about 780 nm since the photoinitiators are sensitive in the UV region of about 400 nm [82]. The pulse width is about 150 fs with a 100 MHz repetition rate [83]. Ytterbium based lasers are also popular [75]. This is followed by tuning the incident power, using a scanner for fast writing and focussing using the objective lens while the sample is mounted onto the stage [76]. The shutter controls the exposure time (governing the number of pulses received by the objective). A 3 degrees of freedom piezoelectric translational stage (in X, Y, Z) maybe be employed to move a few hundred microns (Piezo mode) or instead, the X-Y motion of the beam may be controlled using a galvanometric scanner while the Z motion is controlled via the stage (Galvo mode) [75, 76, 84] as shown in figure 1.7. An oil immersion based objective may be used to achieve a high resolution on transparent substrates while the Dip-in Laser Lithography (DiLL) configuration involving the objective to be in direct contact with the photoresist can be used write on opaque surfaces. The real-time imaging is performed using a CCD camera. The piezo mode allows a much larger range of movement than the galvo mode but a much lower writing speed (up to 1000 times, 200 mm/s vs. 300 µm/s in case of the Nanoscribe) [78, 82]. There are two different commonly used methods of writing, commonly termed as Pin-point scanning mode (PSM) and the Continuous scanning mode (CSM) [63, 79]. The PSM mode has a longer exposure time than the CSM mode as a result of the slow response of the shutter involved [79].

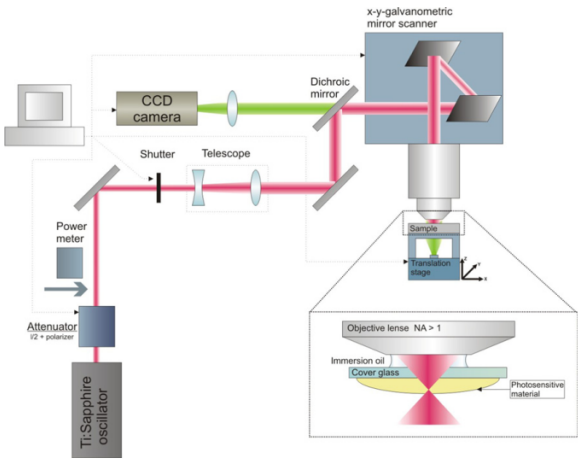

Figure 1.7: *The setup for a two-photon polymerisation machine. Reproduced from [84]*

1.11.4. Materials

A variety of materials including metal particles, polymers, ceramics and hybrid materials can be linked using 2PP in the presence of appropriate initiators. However, polymer resins are most commonly used due to the ease of tuning their chemistry to achieve appropriate properties.The commonly used resins can be classified based on the chemistry involved in the reaction into the following types [75, 76]:

- *Acrylates*: These generate free radicals upon photo-illumination and are used in the liquid state. Acrylates undergo a substantial shrinkage in volume. The acrylate based resists provided by Nanoscribe include IP-L 780, IP-DIP, IP-S, and IP-G. Among these IP-L 780 and IP-Dip are known for their high resolution printing capability.
- *Photoacidic resins*: These include epoxy based resins such as SU8 which undergo cationic polymerisation upon polymerisation and a post-baking step. It is quite popular within the conventional photolithography based systems.
- *Hybrid resins*: These are usually organically modified Silicates and belong to the class of hybrid organic-inorganic resins. They are prepared via Sol-gel method and are thermally and chemically more stable, optically transparent and mechanically robust. Ormocomp®is a commonly used hybrid resin especially popular in cell based studies.

Ormocomp®has a proven biocompatibility thus making it useful for cell based studies. IP-L resist has been found to be biocompatible too for fibroblasts [85] but this needs to be verified for human MSCs. IP resists have a higher modulus of elasticity (than Ormocer®) thus making them more suitable as a bone-regeneration substrate (see Appendix F.2).

1.12. Application of 2PP in cell-based studies

Nava et al. fabricated scaffolds using 2PP to culture bone marrow derived MSCs that were cultured in an α-minimal medium, changing the medium twice a week [86]. The substrates were sterilised using de-ionised (DI) water and ethanol mixture followed by a UV treatment. They observed increased cell proliferation on the scaffolds than the control group (plain glass). Basu et al. used 2PP to produce protein crosslinked structures in the form of micro/sub-micron topography in presence of Rose Bengal photoinitiator and studied its effect on the morphology of human dermal fibroblasts [87]. Marino et al. fabricated micro ridges to study the morphology of neural cells and observed neurites aligned along the ridges thus indicating differentiation [88]. Ovsianikov et al. used a PEG diacrylate (PEGda) resin in presence of Irgacure and Micheler's Ketone initiators and found them to be cytotoxic [89]. Ageing these in aqueous media reduced the cytotoxicity considerably. Colorectal carcinoma cells were used to test the biocompatibility of IP-DIP resin fabricated microneedles coated with Iron by and were found appropriate for the intended application [90]. Spagnolo et al. fabricated a cage like microstructure to study the effect of pore size on the invasion of cancer infested epithelial cells into the cage [85]. They found the IP-L material to be cytocompatible which suggests its use for prospective life sciences based applications. Features as small as 300 nm have also been fabricated using IP-L and IP-G resists and coated with TiO_2 to culture osteoblast like cells [83]. Thus 2PP isn't new to fabricating structures for cell based studies. These studies have been summarised in Table 1.5.

Table 1.5: *2PP applications in Life-sciences based applications*

Application/ Description	**Material**	**Parameters**	**Feature sizes employed**	**References**
2PP fabricated scaffolds to culture MSCs; imaging using gold sputtering for SEM	Irgacure photoinitiator (1%) + SZ2080 resist	1.5 mm/s scan speed; 12 mW power	Height of scaffold = 30 μm; Length and width = 90 μm; horizontal spacing of 10-30 μm between lines; vertical spacing of 15 μm	[86]
To confine embryonic stem cells in a 2PP fabricated cage. Cells maintain pluripotency gene	Irgacure photoinitiator (1%) + SZ2080 resist	Same as in [86]	Same as in [86]	[91]

Table 1.5 – *Continued from previous page*

Crosslinking Fibronectin (FN), Bovine serum albumin (BSA) and Fibrinogen (FG) proteins using 2PP to study the morphology of human dermal fibroblasts	FN, FG, BSA, Rose Bengal	Laser power ranging from 30-50 mW	Parallel lines 200 μm long, 600 nm wide with varying pitch of 10-40 μm	[87]
Using 2PP to fabricate submicron patterning structures to study neural cell behaviour; imaging using SEM and AFM	Ormocomp resin coated on glass coverslip	50 μm/s writing speed; 10 mW laser power	Ridges with 2.5, 5 and 10 μm spacings; roughness of 3.20 ± 0.28 nm and height and width of 658 ± 29 nm and 482 ± 24 nm respectively	[88]
Polyethylene Glycol (diacrylate) scaffolds fabricated via 2PP for testing cytotoxicity on mouse fibroblasts	PEGda with Micheler's Ketone or Irgacure photoinitiators	Minimum resolution using 20-30 mW laser power and 200 μm/s scanning speed	200 nm minimum lateral resolution	[89]
$Ti0_2$ coated (using Atomic layer deposition) micropillars that are interconnected using thinner structures and cultured with SaOs-2 osteoblastic type cells	IP-L, IP-G; prebake IP-G at 100°C for 1 h; develop using isopropanol or 1-methoxypropan-2-yl acetate	10-20 mW laser power; 100 μm/s scan speed	Pillars of 5 μm diameter, 13 μm height with smaller elliptical rods of lengths 780 nm and 300 nm along semi major and minor axis respectively	[83]
3D cage like microstructures fabricated using IP-L photoresist to study the invasion of cancer tumour cells into pores of the structure	IP-L resist; develop using Isopropanol	4-16 mW laser power; 30 μm/s scan speed	60 μm high pillars; 10 μm diameter; mesh of 2.5, 5 and 10 μm pitch	[85]
Microneedles fabricated via 2PP using IP-dip resist; sputter coated with Iron; Use of TEM and SEM for material and structural characterisation	IP-Dip resist; coating using Iron	15 mW laser power	diameter 630 ± 15 nm; pitch 12 μm; aspect ratio 1:10	[90]

1.12.1. Conclusions

- 2PP allows submicron/nanofabrication with a spatial control of topography while allowing 3D writing.
- The *structural resolution* obtained is dependent on a number of process parameters involved in the 2PP process.
- A variety of *materials* exist that are suited for 2PP based applications. These were mentioned in section 1.11.4 and compared in table F.1. This provides with the flexibility of choosing the most favourable material for a bone healing based study. Many 2PP based materials have been used in cell based studies. The biocompatibility of some of these materials also needs to be verified.
- 2PP alone can thus be used to vary the following factors affecting bone regeneration:
  - (Bio)material
  - Surface topography: spatial arrangement, size, and geometry
  - Feature dimensionality (for printing multiscale features)

- 2PP materials have been widely used for cell studies. IP-L 780, IP-Dip, and Ormocomp®are largely known to be biocompatible.
- 2PP fabricated structures have not been integrated into microfluidic chips to the best of our knowledge. This can be however be seen for other micro/nanofabrication methods.

1.13. Research goals

This study aims to mimick the bone tissue (topographical) microenvironment through the means of a microfluidic device instead of a conventional static cell culture. To realise this, the following tasks need to accomplished within the study:

1. 2D Submicron/nanoscale feature production. Printing at the 2D scale marks the first step towards utilizing and assessing the 2PP process capabilities at a submicron scale. This involves finding
    - the required laser parameters
    - Materials (resin and substrate)
    - Printing configuration DiLL or conventional
2. The produced features need to be reproducible. These should also be upscalable to larger areas. A scheme for morphologically characterising feature dimensions and quantifying the pattern reproducibility/uniformity also needs to be decided.
3. Fabricating and assembling the microfluidic device. This needs to be done keeping the device requirements mentioned in section 1.6 in mind. Within these the most important requirement stands in terms of making these devices biocompatible. Appropriate materials and fabrication methods need to be looked at for the same. Integrating the patterns into the microfluidic device is a major component within assembly process.
4. Evaluating the device for gauging its performance. This should include a preliminary test using stem cells to demonstrate the proof-of-concept and assess the biocompatibility of the system. A topography needs to be characterised for delamination to check if it can withstand the flow rates applied within the device.

1.14. Proposed approach

This section explains the basic design and fabrication strategies proposed in order to realise the various research goals listed in section 1.13.

1.14.1. Topography production and characterisation

This would involve using the 2PP fabrication system from Nanoscribe GmbH. The topography design used in this study would begin with the well known pillar based structures as in the state of the art designs [31]. The IP photoresists that are provided by the manufacturer would be suitable for such an application. Obtaining the minimum feature size would possibly involve carrying a parametric sweep of the 2PP process parameters (such as laser power, speed of writing etc.). Different resins (in various configurations) and writing modes (Piezo, DiLL) within 2PP may also be compared to decrease feature sizes.

Morphological characterisation

Imaging the topography: Non-conducting polymer structures involve the use of Platinum or Gold sputtering for imaging using the Scanning electron microscope (SEM) [86]. Structures of sub-100 nm should be possible to be imaged using a high-resolution SEM however, if it is problematic, an AFM may also be employed for the same. The sputter coating would add a few nm thickness to the structures but that should not be problematic for sub-micron structures. It is also important to measure the percentage uniformity of these pillars and the print repeatability using some form of image analysis.

1.14.2. Topography upscaling and uniformity assessment

Upscaling may involve scaling the patterns in terms of area or even dimensionality. The latter points towards a possibility of printing over 3D structures to produce multiscale topographies. The former case: expanision of topographies area-wise is the primary goal since one of the major problems concerning nanotopographical features for cell culturing microfluidic devices is the inability to reproduce these patterns on a large scale, or in other words, *scaling up the patterned area* without affecting the pattern quality [49].
The ability of 2PP to pattern the substrate on a large scale needs to be evaluated (for areas atleast more than $300\times300\mu$m, since above these dimensions, a stitching operation is needed). This should involve adopting a 'stitching' strategy wherein small areas are repeatedly printed over different location on the substrate. It

is of utmost importance that these submicron patterns be reproducible. Hence, printing on a large scale area should produce patterns that show a good uniformity. Uniformity may be quantified using standard deviation in pillar dimensions, or obtaining percentage of the area that has pillars within a certain size range. To realise this uniformity analysis over a large area, image analysis using MATLAB and Image-J may be used to reduce manual workload and the number of measurements.

Wettability analysis

Since hydrophilic substrates are preferred for cell attachment [92], the wettability of such a substrate with upscaled topography on it needs to be determined using a liquid drop analyser setup. This would help in quantifying the surface wettability of the substrate layer.

1.14.3. Fabricating the microfluidic device

The microfluidic device would consist of a channel layer and a flat substrate layer. The susbtrate layer shall contain the 2PP printed features on it. The following sections deal with the various aspects of device fabrication.

Channel layer fabrication

Poly(dimethylsiloxane) (PDMS) is one of the most commonly used microfluidic material due to its low cost, biocompatibility, ease of fabrication and bonding, curing via heat and high optical transparency [49]. It also meets the basic requirements of the microfluidic device (see section 1.6), thus making it suitable for this study. TOPAS may also be used in case a higher transparency is desired.
Mold replication can be used for manufacturing the channel layer. The mould (negative) can be prepared either through processes like *3D printing or photolithography* since these are polymer friendly, entail low fabrication times and are widely popular. They have a micrometer level resolution which is good enough for the fabricating the microchannels. However, high precision 3D printing (via *stereolithography*) would be preferable in this case due to the ease of rapid prototyping and its ability to produce complex designs 3D.

Substrate layer

The patterns written via 2PP shall be incorporated on to the substrate layer. 2PP shall be used to produce structures over a glass coverslip. The pillars can be directly printed on glass. Glass is chosen since it is transparent in the near infrared region (for 2PP), possesses good adhesion to the photoresist, and can also allows imagining using microscopes (optical/fluorescent).

Device assembly

The channel and substrate layers need to be bonded together to achieve a leak-proof sealing. *Oxygen/air plasma treatment* is commonly used to bond PDMS layers together or PDMS to a glass substrate. Applying such a treatment to glass makes it hydrophilic and thus increases its bioactivity. Yang et al. [49] also pointed out that such a treatment may damage the topography or alter the chemistry of the substrate and thus influence cell behaviour upon culturing. In their work, they used the "*Stamp and Stick*" technique developed by Satyanarayana et al. [93] wherein uncured PDMS or a UV curable polymer is used to stick the channel and substrate layers together. This also provides with a much higher bond strength while preserving the nanostructures and their chemistry. The damage caused to the topography by Oxygen/air plasma needs to be evaluated during experimentation.

1.14.4. Integrated device characterisation

The microfluidic device can be possibly evaluated using the following methods:

Delamination of Structures

The fabricated submicron/nanostructures need to be able to withstand the flow generated shear forces in the microfluidic device/*in-vitro*. The delamination depends on the fluid flow rate, the adhesive forces between the structures and the substrates, the structural strength of the structures as well the spatial arrangement and geometry of the structures.

Preliminary biological studies

This section briefly explains the generally adopted methods of carrying out the cell based studies in order to biologically evaluate the device. The knowledge of such protocols can help in determining the appropriate device characterisation methods and associated risks. The cell culturing protocols involve:

- **Cell suspension preparation**: MSCs derived from bone marrow or adipose aspirates may be used for such studies depending upon the availability. Adipose derived stem cells have been known to possess higher ability to differentiate into osteoblasts than those derived from bone marrow aspirates. The cells would then be multiplied in a suitable medium and stored until seeding into the microfluidic device.

- **Making the device biocompatible**: The device must first be sterilised before culturing by autoclaving, UV exposure or treating with ethanol followed by washing with a Phosphate buffered solution(PBS) [45, 49]. Ethanol seems to be a viable option since the other two may adverselt affect the structures.

- **Cell culturing in the device**: The cells (a specified number) need to be injected into the microfluidic device using a syringe pump for a precise dosage. This may be followed by a static or dynamic culturing using appropriate media (osteogenic or non-osteogenic) and the established biological protocols. The cells are cultured in the device under a suitable external environment using an incubator that mimics the mamallian physiological environment (usually 5% CO_2, 37°C) [90].

- **Imaging**: The cells can be observed via SEM by freeze drying them and coating them with a thin layer of gold to study their morphology and observe the matrix calcification. The mineralisation of the matrix can also be analysed using Energy dispersive spectroscopy (EDS). The optically transparent channel and substrate layers should allow optical microscopy with ease.

1.15. Milestones

The process flow discussed in section 1.14 to realise the research goals of the study are depicted in Fig. 1.8. The flow involves 3 main milestones (or phases) namely the fabrication and upscaling of topography (**Milestone 1**), the device fabrication and assembly (**Milestone 2**), and lastly, the device characterisation (**Milestone 3**).

1.16. Risks

The risks associated with each of them and their mitigation are described below. A risk with a higher probability of occurrence and may pose a significant hindrance has been labelled as 'HR' while the other have been denoted with a 'LR' label.

1. **Topography fabrication and characterisation**

    - **Unable to reach the 'nano' scale (HR)**: It may be possible that the feature size does not go below a few hundred nm. This can be solved by either looking for alternative techniques such as anodization which don't allow full control over the topography or continuing to use 2PP with a sub-micron resolution but with full control over the topography. Pyrolysing the structures may also shrink them to some extent but may also damage them.

    - **Poor uniformity of upscaled patterns (HR)**: It is quite possible that the reproducibility of features at such small scale is poor due to laser fluctuations, vibrations etc. Alternative techniques for nanofabrication may be considered or printing may be continued for larger feature sizes. The latter solution would in-turn serve as an optimisation problem requiring a balance between maximum uniformity and minimum feature size.

    - **Pattern size too small for droplet (HR)**: It is possible that during the surface wettability analysis, the liquid drop being used is much larger than the patterned area. A smaller sized droplet may be created using an AFM hollow cantilever for the same.

    - **Difficulty in imaging using SEM (HR)**: The nanoscale features may be difficult to image using a tungsten filament based SEM. In that case, a field emission SEM (FESEM) with a higher resolution capability may be used.

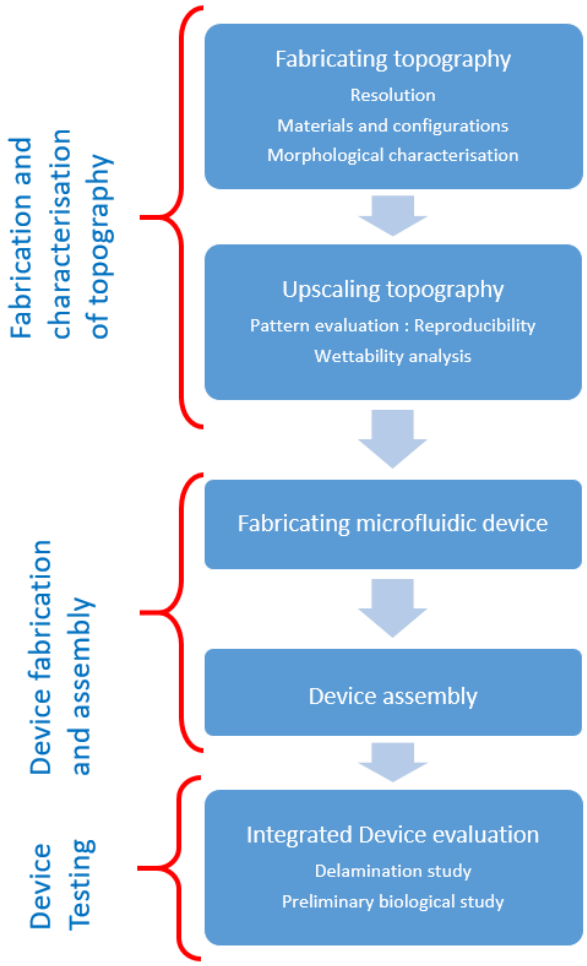

Figure 1.8: *The proposed process flow across various milestones (to the left of red brackets) for the study and the sub-tasks comprising each milestone.*

2. **Device fabrication and assembly**

   - **Bubbles in PDMS (LR)**: The PDMS layer may contain bubbles or may stick to the mould while peeling off. This can be improved by degassing PDMS well before curing and using ethanol while stripping it off from the mould.
   - **Insufficient bond strength (LR)**: The channel and substrate layer may not bond properly using oxygen/air plasma and it may even destroy the nanostructures on the substrate layer. If so, an uncured layer of PDMS may be used as described in section 1.14.3. Different adhesive layers available in the market could also be looked into but these may not be biocompatible.

3. **Integrated device characterisation**

   - **Separating channel and substrate layers (LR)**: Studying the delamination of the structures within the microfluidic device would involve separating the channel and substrate layers for imaging using SEM. This can be tedious and damage the structures in question.
   - **Sterilisation and other biological risks (HR)**: MSCs can be cultured into the device once the device has been deemed safe for sterilisation. Sterilisation processes may cause unwanted effects to the pattern or device. The device and its bonding may also be adversely affected during the various cell culturing protocols. A coating of ECM proteins such as collagen, fibronectin or laminin or that of Gold or TiO_2 may be needed in-case the photoresist fabricated structures are found to be cytotoxic. Such coatings may however change the dimensions of the features.

2

Paper

Developing a microfluidic device incorporating submicron topographies for studying bone regeneration

Abhishek Sharma

Department of Precision and Microsystems engineering, Faculty of Mechanical, Maritime, and Materials Engineering, Delft University of Technology, Delft, The Netherlands

Abstract
A major challenge facing the study of bone regeneration today is the inability to mimic the tissue microenvironment and the factors comprising it. Organ-on-chip based microfluidic systems today aim at doing so by dynamically culturing living cells in them. These are preferred owing to their small feature sizes, laminar flows, high throughput, small reagent quantities, and reduced dependency on animal studies. Substrate topography even at the submicron and nanoscale is known to induce osteogenesis by influencing cells at ligand/receptor levels but poses a major challenge in terms of fabrication and upscaling. The two photon polymerisation (2PP) process allows producing features in a spatially and dimensionally controlled fashion. The method is typically known for fabricating micro-sized structures but remains largely unexplored for producing features in the submicron/nano scale. This study aims at creating reproducible submicron pillar based topographies using 2PP and integrating them into a microfluidic device for studying their effect on bone regeneration. Uniform submicron patterns were produced using optimal process parameters and writing strategy. Further, the patterns were expanded to areas up to 2 mm $\times$ 1.7 mm and their uniformity was assessed. To demonstrate multiscale fabrication, these were also integrated onto a 2PP fabricated micro-scaffold in a single step process. The topography enhanced the surface hydrophilicity and could withstand flow rates of up to 8 ml/min. The human mesenchymal stem cells (hMSCs) dynamically cultured in these integrated devices showed a healthy morphology on the pattern with no visible signs of cytotoxicity even after a period of 5 days. This study marks a step towards printing controlled submicron topographies using 2PP that can be upscaled (both spatially and dimensionally), incorporated into biocompatible microfluidic chips, and thus help in achieving the optimal microenvironment for bone regeneration studies in the future.

Keywords: Bone regeneration, Organ-on-a-chip, Microfluidic, Submicron, Multiscale, Topography, Two photon polymerisation, Mesenchymal stem cells

1 Introduction

The aim of this study was to create topographies with submicron feature sizes and interspacing, and integrate them into a microfluidic device for bone regeneration studies. This was done in an attempt to mimic the microenvironment needed to promote tissue regeneration. Bone is one of the organs in the human body that possesses the ability to renew and remodel itself throughout lifetime. However, not all fractures result in a complete reunion. About 13% of tibial fractures for example, lead to incomplete or insufficient reunion especially in cases where the injury is severe and requires large amounts of bone regeneration [1, 2]. Various bone diseases such as avascular necrosis, osteoporosis, fibrous dysplasia, infections, or those caused due to genetic factors also lead to insufficient tissue regeneration [1, 3, 4]. Biomaterials supplemented with appropriate cell types (stem and progenitor cells), mechanical, physical, and/or other biochemical cues are being studied to realise an optimal microenvironment for promoting osteogenesis (new bone formation) [5, 6]. Making these biomaterials as efficient as the natural bone tissue requires expertise in chemistry, biology, and engineering.

Biomaterial topography is a major factor that affects cell attachment, morphology, proliferation, differentiation, and migration at various scales [7, 8]. For example, macrotopography (above 100 μm) [7], microtopography (0.1-100 μm) [9, 10],and nanotopography (1-100 nm) [11] influence the cells at colony, individual, and ligand/receptor levels respectively. With respect to nanotopography for example, nanopillar heights close to 15 nm, and nanopit diameters of about 30 nm have shown to induce osteogenesis

[11]. Nanotopography can thus stimulate the molecular interactions within the cell and actuate the pathways involved in the bone regeneration process. However, there isn't any known nanopattern in literature that yields the highest degree of osteogenesis. Optimal dimensions such as the required nanopillar diameter, nanopit depth, or the feature interspacing still remain unknown [11]. Also, integrating these nanotopographies on to micro and macro sized features within the biomaterial with a high spatial control remains a critical challenge in terms of fabrication. Innovations in nanofabrication and multiscale manufacturing methods are therefore needed to realise the above goals.

An array of techniques have been used for fabricating submicron/nanoscale features for semiconductor, biomedical, photonic, and microfluidic applications. Beam based techniques (electron beam lithography, UV lithography, X-Ray lithography) [12, 13], anodisation [14], phase separation [15], scanning probe lithography [16, 17], and replica moulding [18, 19] have been some of the most commonly employed fabrication techniques in these areas. The emerging two photon polymerisation (2PP) technique besides providing a high feature size (submicron) resolution , allows control over their dimensions and spatial arrangement. The ability to fabricate 'truly' 3D features also gives it an added advantage over other lithography processes. The process involves the use of a mode locked near infrared femtosecond laser to focus two ultrashort pulses of photons onto a photo-sensitive material [20, 21]. This photoresist material upon exposure, may become soluble or insoluble with respect to the developing agent. The 2PP method has been widely used to print microscale features however, the method still remains largely unexplored for reliably producing submicron and nanoscale features of required dimensions. Even though lines as thin as 50 nm have been produced via this method, laser fluctuations are a major cause of poor repeatability at this scale [20, 22].

Microfluidic devices provide the opportunity of encapsulating these submicron and nanoscale features to mimic the bone microenvironment. Their use for Organ-on-Chip (OOC) applications has been increasing over the years to simulate the tissue or organ level physiology [23]. Microfluidic models are chosen in such studies owing to their small feature sizes leading to laminar flows, being able to closely monitor and control the cell microenvironment, high throughput allowing multiple experiments on the same chip, the use of small reagent quantities and cell aspirate volumes, the ability to create a dynamic culture environment, allowing real-time imaging, and reducing dependency on animal studies [24, 25]. Studying the effect of submicron and nanoscale topographies would thus benefit from integration of such features into a microfluidic device. 2PP fabricated microstructures have long been used for static petridish based cell studies [26, 27] but their incorporation as submicron/nanopatterns into microfluidic chips remains unknown.

In this study, we propose 2PP as the method for fabricating submicron sized patterns and their integration into a microfluidic device. Ellipsoidal pillar based patterns/topographies (resembling the shape of the laser voxel) were produced and their uniformity was enhanced by selecting appropriate configuration (materials), writing mode, and correcting for the substrate tilt. The pillars were morphologically characterised and upscaled to a large area (in mm scale). Patterns were also produced on a micro-scaffold (also produced using 2PP) to illustrate the possibility of multiscale single step printing using this process. After integrating them into microfluidic devices, the patterns were tested for pillar delamination against a microfluidic flow to assess their adhesion and suitability for dynamic biological cultures. The device was also seeded with human mesenchymal stem cells (hMSCs) to study the cell response and check for any visible signs of cytotoxicity over a time period of 5 day dynamic culture.

2 Materials and Methods

2.1 Submicron pattern production

A pillar based topography was selected for this study. These pillars were written using the two-photon polymerisation (2PP) process in the Nanoscribe Photonic Profession (GT) laser lithography system. The system operates using a femtosecond laser with a wavelength of 780 nm, pulse width of about 150 fs, and a 100 MHz repetition rate. The Piezo writing mode in the Dip-in Laser Lithography (DiLL) configuration was selected for writing the pillars with each pillar representing a single voxel within the writing process. The acrylate based IP-Dip resin, provided by the manufacturer was used in combination with fused silica substrate (length = 25 mm, width = 25 mm, thickness = 0.7 mm) coated with a layer of Indium Titanium Oxide (ITO). The coated side of the substrate faced the objective lens (63X, NA 1.4) during the writing process. The samples were washed with acetone and isopropanol prior to the writing procedure. After writing, the samples were developed in a chemical bath of Propylene glycol monomethyl ether acetate (PGMEA) for 25 minutes, followed by 5 minutes of development in isopropanol.

2.2 Upscaling patterns

Writing parameters within the 2PP process were chosen for printing reproducible pillars of known dimensions. The process was then extended to write these topographies over larger areas (up to 2 mm $\times$ 1.7 mm) by stitching smaller

Table 1: *Sample description for integrated microfluidic testing*

Testing	Substrate	Pattern size	Bonding
Pillar delamination	ITO coated fused silica	1mm × 0.1 mm	Mechanical clamp
Preliminary cell studies	Fused silica	1 mm × 0.3 mm + 1 mm × 0.3 mm (upatterned)	Air plasma

written areas of 100 μm × 100 μm together. The method was then used to print submicron sized pillars on a microscaffold written using the Galvo mode in the machine. This was done to illustrate the possibility of incorporating such submicron topographies onto other macro and micro printed structures in the future.

2.3 Characterisation of the patterns

The topographical patterns produced were imaged using a scanning electron microscope (Jeol Intouchscope JSM-6010LA). An optical microscope (Keyence Digital Microscope VHX-6000) was used to obtain the pixel intensity maps and estimate the uniformity in pillar dimensions across the sample. Such a uniformity analysis would thus be indicative of the print reproducibility.

A drop shape analyser (Krüss Drop Shape Analyzer – DSA100) was then used to measure the contact angle of deionised water on the (upscaled) pattern in order to study the change in the wetting properties caused by the pattern. Deionised water droplets of volume 0.1-0.3 μl were placed on the patterned and non patterned regions of the ITO-coated substrate (that underwent development process beforehand involving isopropanol, PGMEA, and acetone) and the contact angle was recorded 5 seconds after drop placement. The samples were cleaned with isopropanol again prior to the angle measurements.

2.4 Microfluidic device fabrication

To fabricate the microfluidic device, a PDMS block containing a single micro-channel of length = 7.85 mm, width = 1 mm, and height = 200 μm was prepared using the mould replication technique. The mould was 3D printed using stereolithography (Envisiontec Micro plus HD). PDMS was mixed with the curing agent (SYLGARD 184) in a 10:1 mixture for 5 minutes. This mixture was poured into the 3D printed moulds and dessicated for 1 hour to remove any trapped air bubbles. The moulds were then heated at 70 °C for 3 hours and the PDMS was then peeled off from the moulds.

The PDMS layer was then placed over the substrate while aligning the pattern width with that of the channel (as shown in Figure 1c. The procedure for bonding PDMS to the substrate depended upon the kind of testing it was being subjected to later. For delamination testing, ITO coated fused silica glass was used as the substrate and was pressed onto the PDMS layer by means of a mechanically designed clamp. The pattern size used in this case was 1 mm × 0.1 mm. For the preliminary biological testing, uncoated fused silica was used as the substrate and it was bonded to PDMS using air plasma method. In this case, the patterns were written over a 1 mm × 0.3 mm area. The testing method and the respective sample details have also been summarised in Table 1.

2.5 Testing the integrated microfluidic system

Testing the device firstly involved studying the delamination of pillars with respect to the varying flow rates of deionised water. This also served as a method to assess leakages within the device and its potential for being used as dynamic cell culturing platform. The cytocompatibility of the device was then assessed via a preliminary cell study.

2.5.1 Delamination of pattern

As discussed above, 1 mm × 0.1 mm pattern strips were incorporated into the microfluidic device held leak-proof using a clamp. This was done because the strength of bonding produced between the ITO coated substrate and PDMS by air plasma technique is weaker in comparison to an uncoated fused silica substrate. The mechanical clamp (3D printed using Original Prusa i3 MK2S printer) holding the chip is shown in Figure 1a. The clamp design can be seen in the Solidworks exploded view model in Figure 1b. The chip was then connected to a peristaltic pump (Ismatec ISM 915) and varying flow rates of deionised water were applied. Pillar delamination was observed before and after the experiment using optical and SEM imaging techniques.

2.5.2 Preliminary cell study

The fused silica substrate was bonded to PDMS using air plasma. For this, the channel side of PDMS and the patterned side of the substrate were exposed to the plasma for 2 minutes at 40 W and a chamber pressure of 4 $m$bar. This method of bonding was done to allow real time optical imaging of the samples and improve their ease of handling (in comparison to a mechanical clamp). 3 μm thick unpatterned flat sheets of the same length and width as the pattern were also printed but using the Galvo writing mode.

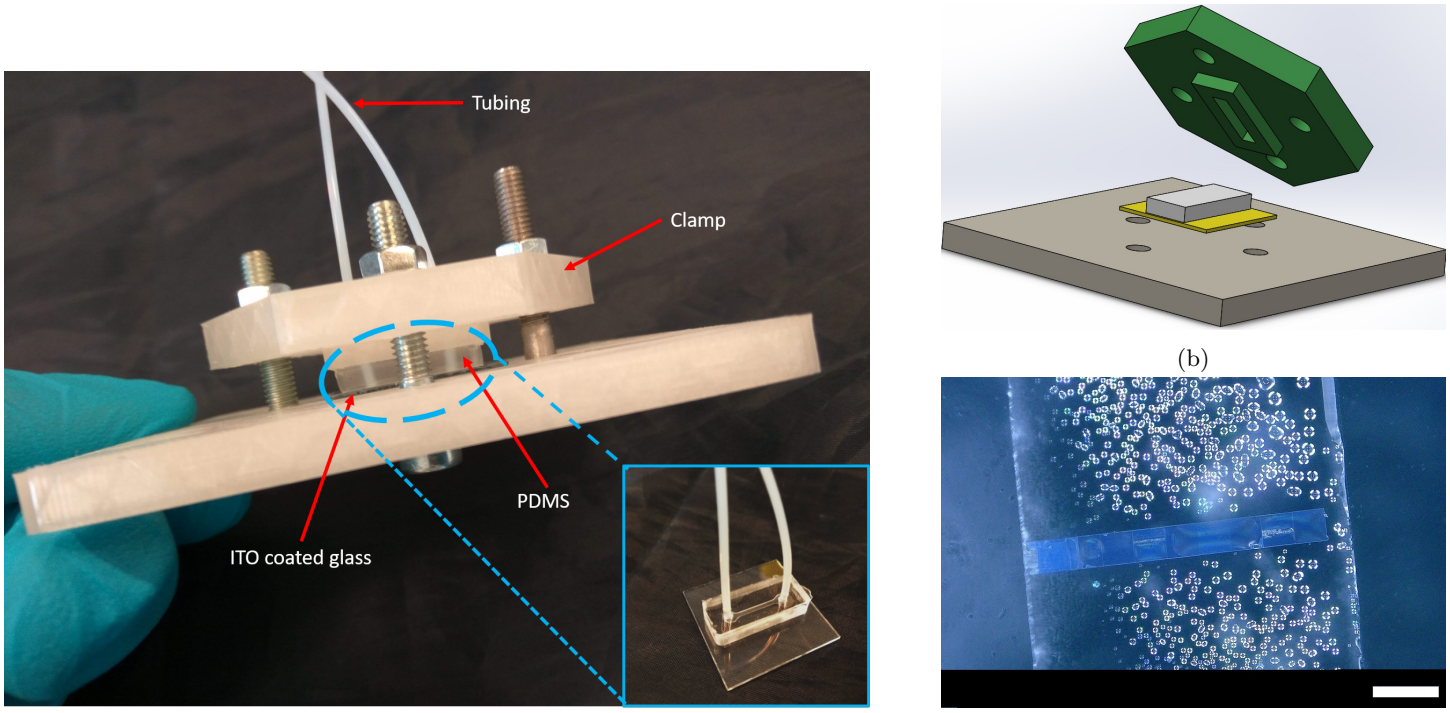

Figure 1: *Setup for the microfluidic delamination testing of the patterns.* ***(a)*** *Clamped PDMS chip and the microfluidic connections. The PDMS channel is aligned over the ITO coated fused silica substrate containing printed topography on it. Zoomed-in blue region shows the details of the microfluidic device before being clamped.* ***(b)*** *Solidworks model of the chip assembly.* ***(c)*** *Aligning the pattern along the channel width. Micro droplets can be seen in the channel after experiment. Scale bar is 200 μm.*

These were printed parallel to the pattern and similarly aligned along the channel width. The bonded devices were then connected to the tubings through the holes punched into PDMS at the channel inlet and outlet.

To conduct the cell studies, hMSCs were expanded in a preculture using protocols mentioned in [28]. A cell suspension of 1.1×10^6 cells/ml was achieved before seeding them into the microfluidic channel. For sterilisation, the microfluidic device was flushed 2-3 times with the α-MEM culture medium followed by cell seeding into the microchannel. The cells were allowed to statically attach to the channel surfaces by incubating (at 37 °C, 5%CO_2) for 24 hours before starting the flow of culture medium at 20 μl/h. The cells were optically imaged in the device after 1, 4, and 5 days of dynamic culture and later examined using SEM.

3 Results

3.1 Pattern production

Producing the topographical pattern first involved selecting the appropriate configuration and writing mode within the 2PP process that provided the best pattern uniformity (also related to pattern reproducibility). This was followed by adopting a tilt correction strategy for the substrate to further enhance the pattern uniformity. Lastly, a parametric study of the 2PP writing parameters aimed at minimising feature sizes was carried out and its effect on pattern uniformity was assessed. The subsections below sequentially describe the entire process.

3.1.1 Selecting print configuration for enhancing uniformity

After assessing various configurations and the respective available materials (resin and substrate) for the 2PP setup (depicted in Table 2), it was found that the ITO coated fused silica substrate yielded an interface signal amplitude (a value directly proportional to refractive index mismatch at the interface of the resin and the substrate) of about 5000-6000 in combination with IP-Dip resin while an uncoated fused silica substrate lowered this value almost by almost an order of magnitude. The amplitude value further dropped to about 300 while using the conventional configuration (IPL-780 and borosilicate glass) in the machine. En-

Table 2: *Configurations in the 2PP process, their respective materials, and Interface signal amplitude. The interface amplitude is directly related to the difference between the refractive indices of the resin and the substrate.*

Configuration	**Materials**	**Interface signal amplitude**
DiLL	IP-Dip + ITO coated fused silica	5000-6000
DiLL	IP-Dip + Unacoated fused silica	600-700
Conventional	IP-L 780 + Borosilicate glass	300-400

hancing this interface signal amplitude improved the uniformity in patterning over larger areas. More information regarding this can be found in supplementary section 3.1 (Figures 3.2 and 3.3).

3.1.2 Selecting writing mode and tilt correction of the substrate

From the available writing modes available in the 2PP process, the Piezo writing mode was chosen to produce each pillar as a single voxel. The much faster Galvo writing mode in the machine could not be used since it does not support compensating for the tilt of the substrate. At the submicron scale, this led to large variations in pillar dimensions along the direction of writing due to the angular motion of the scanner involved in Galvo based writing. Variation also occurred in the chosen Piezo writing mode but these could be reduced using the tilt compensation method as described below. A comparison between patterns printed using both these writing modes in the conventional configuration can be seen in supplementary section 3.2 (Figure 3.4).

Within the Piezo writing mode, a necessary correction accounting for the tilt of the substrate (accuracy in the order of 0.01°) was made to obtain a uniform pattern. This method involved measuring the interface position (in z direction) at different points across the substrate followed by fitting a linear plane through them. The tilt angles of this fitted plane in x and y directions were manually input into the 2PP machine program to add appropriate offsets in z coordinate while traversing in x and y directions. The auto tilt correction option in the machine (that follows an automated procedure to measure substrate tilt) yielded non repeating tilt angle values thus requiring to measure the tilt manually (that gave repeatable tilt values). More information about this method can be found in supplementary section 3.2 (Figure 3.6). The uniformity of patterns written on manually tilt corrected, auto tilt corrected, and uncorrected substrates (ITO coated fused silica, DiLL configuration) can be seen in supplementary section 3.2 (Figure 3.7)

The uniformity of the patterns which is referred to as the percentage area with pillar diameters larger than a minimum cut-off value (calculated using the scheme discussed later in section 3.2) was plotted for ITO coated and uncoated substrates, as shown in Figure 2a. It depicts an increase in pattern uniformity with an increase in the interface signal amplitude. The same analysis was done to observe the effect of tilt compensation on the ITO coated sample (Figure 2b). An increase in pattern uniformity can be seen for tilt corrected samples. The laser parameters had been kept constant for both the studies.

3.1.3 Parametric study in 2PP

After choosing the DiLL configuration (involving IP-Dip and ITO glass), and using the Piezo writing mode (that allowed tilt correction of the substrate) to achieve uniform patterns, the effect of 2PP writing parameters on the pillar dimensions and pattern uniformity was studied. Increasing laser power and time of exposure proportionally scaled up the dimensions of the voxel while increasing the distance of this voxel from the interface of the substrate and resin (called the Interface distance henceforth) affected the attachment of these pillars to the substrate, and reduced their height and diameter. The trends can be seen in Supplementary section 3.3 (Figures 3.8 and 3.9).

Reducing the laser power or time of exposure apart from decreasing the pillar dimensions, also led to a decrease in the uniformity of the printed area. Similarly, increasing the interface distance starts the printing process deeper into the substrate and led to a reduction in the pattern uniformity. These effects on pattern uniformity have been illustrated in supplementary information section 3.3 (Figures 3.10 and 3.11). To obtain pillars of sub-micron resolution while maintaining a good reproducibility of patterns, a laser power of 27.2 mW, a time of exposure of 2400 μs, and an interface distance of 0.3 μm were chosen as the optimal 2PP parameters. The pillar interspacing (centre to centre) was fixed for these patterns at 800 nm. A SEM micrograph depicting the individual pillars (in a local region of the pattern) obtained using these parameters is shown in Figure 3a. It can be seen that the pillars resemble an ellipsoidal shape similar to that of the voxel. A small fraction of the printed pillars were also found to be detached from the substrate (as shown in Figure 3b) while remaining in contact with it due to the strong stiction forces from developing in

PGMEA and isopropanol. These observations led to devising a method for analysing the uniformity of these patterns printed over larger areas.

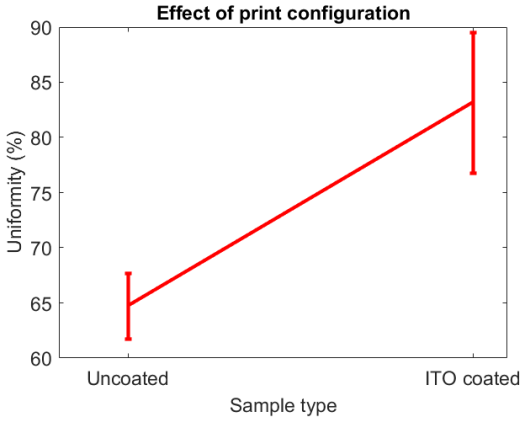

(a)

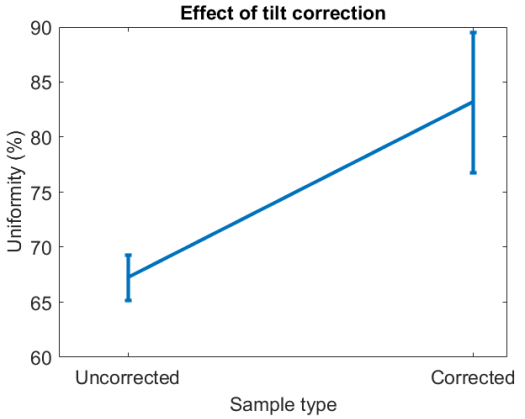

(b)

Figure 2: *Effect of print configuration and tilt compensation on the pattern uniformity (n = 4).* ***(a)*** *Increase in the uniformity of pattern when using ITO coated fused silica substrate in comparison to an uncoated substrate.* ***(b)*** *Increase in the pattern uniformity when the tilt of the ITO coated substrate is taken into account. Both cases (a) and (b) were compensated for tilts. Uniformity is measured as the percentage area showing a pixel intensity less than the threshold value found in section 3.2.*

3.2 Characterisation of patterns

3.2.1 Measuring uniformity of patterns

A 1 mm × 0.1 mm area was patterned using the above mentioned optimal laser parameters. The pillar height and diameter (mean diameter of the ellipse) in this area were quantified by taking multiple low resolution images at 850X using a scanning electron microscope and stitching them together to form the complete mesoscale image of the entire

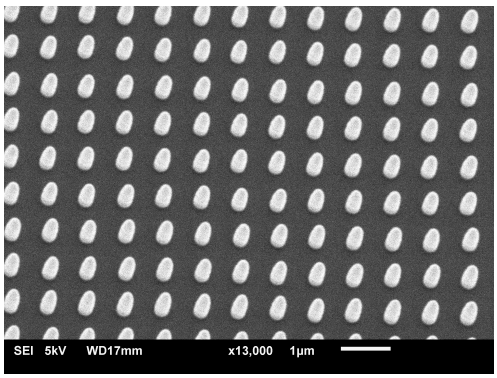

(a)

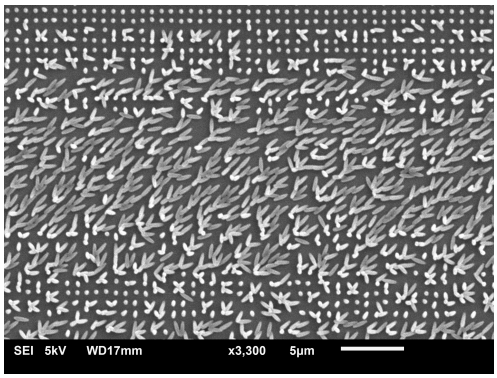

(b)

Figure 3: *Morphological characterisation of submicron pattern using SEM.* ***(a)*** *Printed sub-micron pillars imaged at a tilt of 20 °.* ***(b)*** *Delaminated pillars attached to substrate via stiction forces. The pillars in a feasible region (a) have been compared to pillars that were delaminated during fabrication in (b).*

pattern (Figure 4a). This image was then scaled using a high resolution image at 13000X from a region within the pattern (such as one in Figure 3a). Table 3 shows the various parameters obtained upon characterisation of the pillars.

The optical micrograph of this region is depicted in Figure 4b. Region 4 within this image shows a uniform pillar distribution while the colour intensity decreases in Regions 5 due to a decrease in the pillar diameter. A further decrease in pillar diameter produces areas such as Region 2. There are also regions where there are no printed pillars (such as Region 1) or regions where the pillars delaminated (Region 3) during the development procedure in PGMEA and IPA due to insufficient attachment (also shown in Figure 3b). The optical image can be correlated to the data obtained from the scanning electron micrograph to find the thereshold pixel intensity corresponding to the permissible minimum pillar diameter. This can be done by correlating

the pillar diameter distribution histogram shown in Figure 4c to the pixel intensity distribution in Figure 4d. These pixel threshold intensity values can then be used as a quick and approximate method of quantifying the uniformity of topographies printed using the same laser parameters. For example, about 73% area in optical image shown in figure 4b corresponds to pillar diameters larger than 284 nm (mean diameter - 50 nm). An upper limit of about 500 nm was also applied on the diameter to avoid counting delaminated pillars stuck to the substrate in this analysis. Applying the obtained intensity threshold yields an image depicting the feasible regions as shown in Figure 4e.

Table 3: *Morphological characterisation of pillars*

Number of pillars expected	156250
Number of pillars printed	118966
Interspacing (center to center)	800 nm
Mean diameter (d) ± sd	334 nm ± 30 nm
Mean height (h) ± sd	1541 nm ± 60 nm

3.2.2 Wettability analysis of the patterned substrate

It was seen that the contact angle of the water droplet decreases from 81.84° (n = 9, $\sigma = 3.15°$) on the plain substrate to 41.7° (n = 9, $\sigma = 3.9°$) on the patterned counterpart. 'n' and 'σ' represent the number of samples and standard deviation in the measured angle respectively. Figure 5 shows the increase in substrate hydrophilicity due to the pattern.

3.3 Pattern upscaling: Area and dimensionality

Figure 6a depicts the upscaling of this pattern to an area of 2 mm × 1.7 mm. It took about 87 hours and 50 minutes to print this area. The process is thus not an ideal one for mass production but rather for rapid prototyping of large scale area patterns. The percentage of area in this case that lies in the allowable diameter range ≥ 284 nm was found to be about 86% (n = 1).

Figure 6b shows the incorporation of these patterns onto a microscaffold. The scaffold was designed using the Galvo mode of writing and was fabricated using two perpendicularly aligned layers of woodpile structures. The patterns were incorporated by switching from Galvo mode (used for woodpile) to the Piezo writing mode. For the next layer of woodpile, the writing mode is switched back to Galvo followed by Piezo writing mode for the topography. Each woodpile is 55 μm long and has a cross section of 5 μm × 5 μm. The woodpiles were spaced by a centre to centre distance of 10 μm. It is also worth noting that the patterns have been printed at an increasing distance from the surface

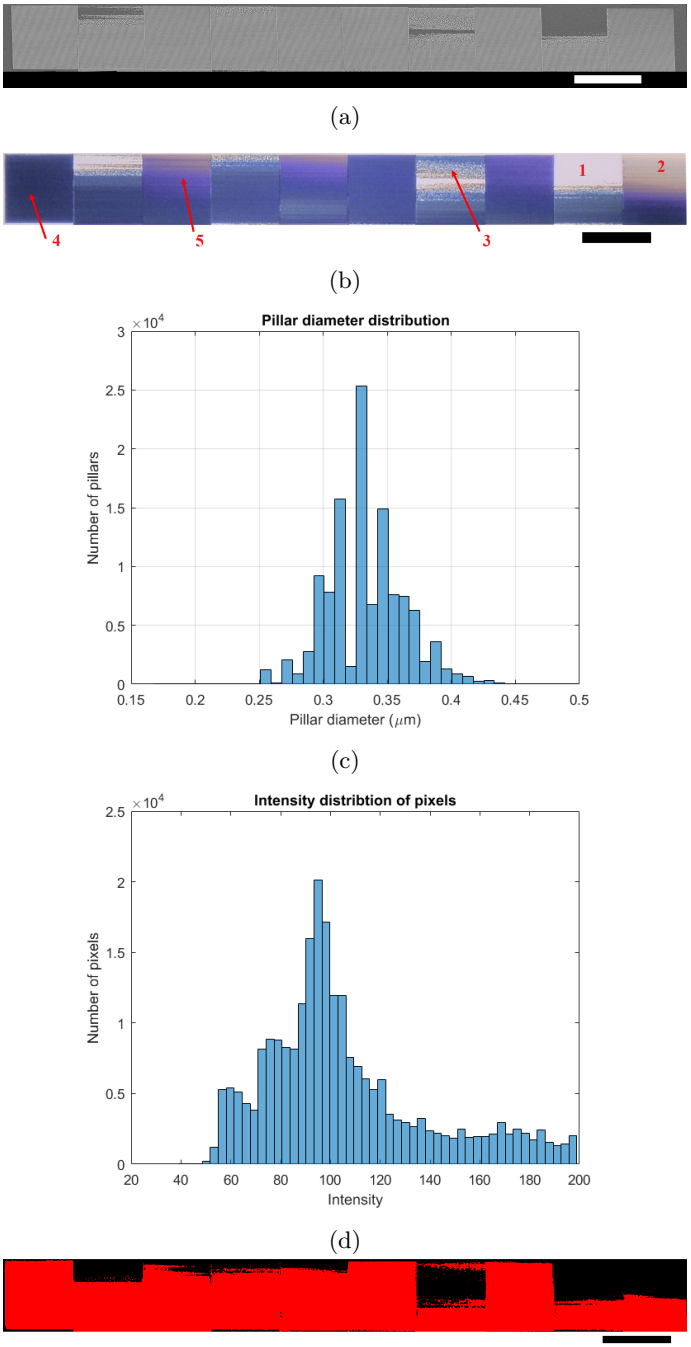

Figure 4: *Morphological characterisation of a mesoscale printed area.* ***(a)*** *Stitching low resolution SEM images to a 1 mm × 100 μm area.* ***(b)*** *Frequency distribution of pillar diameters obtained from SEM image in (a).* ***(c)*** *Optical image of the area depicting different kinds of regions within the pattern.* ***(d)*** *Frequency distribution of the pixel intensities obtained from optical image in (b).* ***(e)*** *Applying the obtained threshold intensity to image in (b). The red regions represent the feasible area while the black regions represent pillars outside the dimension bounds (diameter ≥ 284 nm). Scale bars are 100 μm.*

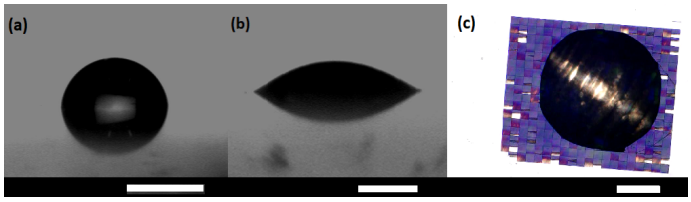

Figure 5: *Decrease in the contact angle from the non patterned substrate (a) to the patterned substrate (b). Top view of a drop resting on the pattern depicted in (c). All scale bars are 500 μm.*

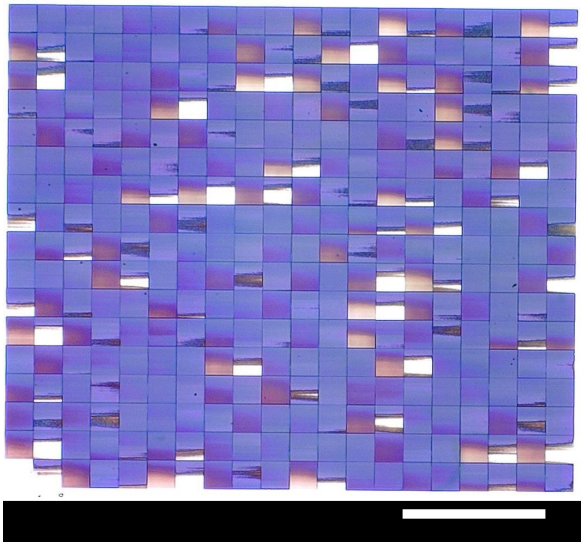

(a)

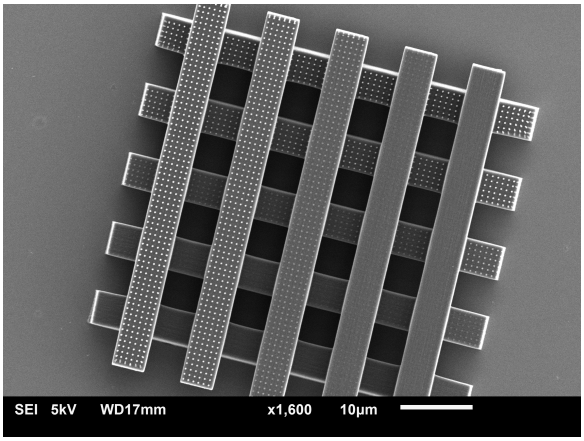

(b)

Figure 6: ***(a)*** *Submicron topography extended to a 2 mm × 1.7 mm area. Scale bar is 500 μm.* ***(b)*** *Submicron topography incorporated onto a woodpile based micro-scaffold*

of woodpile from left to right for the upper layer and top to bottom for the base woodpile layer thus leading to visible

Table 4: *Microfluidic testing conditions for pillar delamination studies. 3 samples per flow rate were tested.*

Flow rate (ml/min)	**Shear stress (Pa)**	**Comments**
1	2.24	Pillars unaffected, no leakages
3	6.72	Pillars unaffected, no leakages
5	11.2	Pillars unaffected, occasional leakages
8	17.92	Pillars unaffected, leakage via inlet/outlet

a gradient in the height and diameters of these pillars at various woodpiles.

3.4 Delamination of pillars in microfluidic channel

For the device with micro channels of length(l) = 7.85 mm, width(w) = 1 mm and height($2h$) = 200 μm, the shear (τ) on the walls of the channel for a flow rate Q is given by:

$$\tau = \frac{3\mu Q}{2wh^2} \tag{1}$$

For the channel considered, a shear stress of about 2.24 Pa acts on the walls per unit ml/min flow rate of water (dynamic viscosity $\mu = 8.90 \times 10^{-4}$ Pas). Table 4 shows the flow rates applied and the resulting wall shear forces. It was seen that the topography remained unaffected at flow rates as high as 8 ml/min. Figure 7 shows the unaffected pattern (optical and SEM image) after being to subjected to a flow rate of 8 ml/min. The mechanical clamp facilitated an easy dismounting of the PDMS layer from the substrate (figure 1). The sample was tilted by 20° during SEM imaging with respect to the normal to show that the pillars are attached intact to the substrate. Above these flow rates, keeping the chip leak proof was cumbersome (especially at the inlet and outlet connection points). These flow rates are much higher than the few tens or hundred μl/h values encountered in dynamic cell cultures [24, 29].

3.5 Preliminary microfluidic cell study on device

As discussed in section 2, the microfluidic devices for these studies were bonded using air plasma and the substrate used in these studies was uncoated fused silica. The devices were sterilised by washing using the culture medium and not using conventional methods such as UV irradiation, autoclaving, or ethanol cleaning due to the risk of damaging the patterns or/and the PDMS layer. It was seen even

after 5 days of cell culturing, there were no major signs of cytoxicity visible in the device. Figures 8(a)-(c) and (d)-(f) show the optical images taken after day 1 and day 5 of cell seeding respectively for the control, sheet, and the patterned surfaces. The SEM micrograph in figure 8h depicts the MSCs on the flat sheet surface. The cell around the sheet can be seen in contact with a cell on the sheet via filopodia. Figure 8g depicts the a cell spreading over the pattern. The cells have a healthy, spread morphology and they can be seen exerting contractile forces on the pillars, causing them to bend. It is difficult to make conclusions about cell migration or preference for unpatterned Galvo written sheets, Piezo mode written submicron patterns or control glass regions. More studies and longer culture times are be needed to further draw any conclusive results.

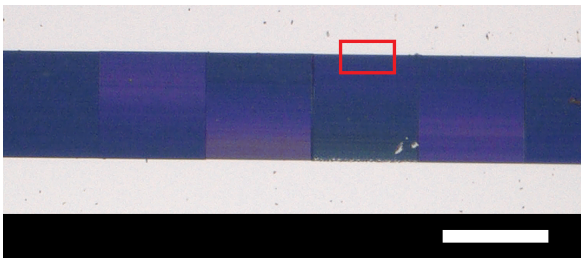

(a)

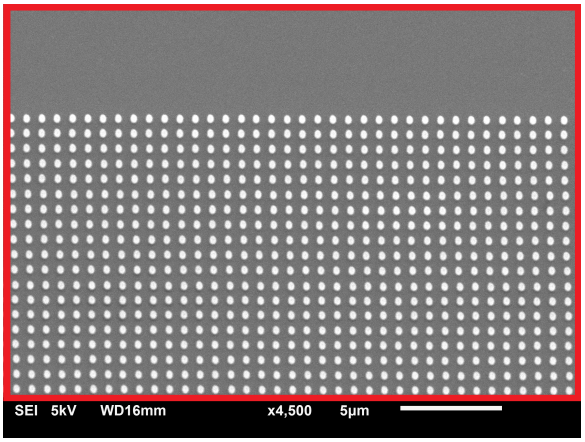

(b)

Figure 7: *Optical image of the patterned area* ***(a)*** *and a zoomed in scanning electron micrograph of a region within this pattern (in red) taken at a tilt angle of 20° and* ***(b)*** *after performing microfluidic delamination test at a flow rate of 8 ml/min. No signs of delamination can be seen.Scale bar in (a) is 100 µm.*

4 Discussions

4.1 Fabricating reproducible patterns

Achieving structures of specific dimensions involves optimising a number of parameters such as the laser power, time of exposure, interface distance, structure interspacing, and other Piezo writing based parameters. Pillars as small as 200 nm in diameter could be fabricated using the 2PP process in this study (see supplementary information section 3.3, Figure 3.8 and 3.9). This is in line with the minimum lateral feature size suggested by the manufacturer. The height and diameter of the structures at these scales act as dependent variables that scale simultaneously with laser parameters. Therefore at the submicron scale, it can be challenging to fix one of these dimensions while varying the other. As mentioned before, pattern uniformity during printing remained a major challenge that hindered their upscaling to larger areas. Uniformity is affected by a number of factors at this scale. The printing configuration, writing mode, tilt of the substrate, size of the pillar (dependent on laser parameters and interface distance), and environmental factors (temperature, humidity, vibrations) are some of the major factors that have been identified in this study.

The printing configuration involving IP-Dip resin on an ITO coated fused silica glass depicted the highest interface contrast, hence leading to patterns that showed uniformity of up to 86% (pillar diameter $\geq$ mean diameter - 50 nm) when scaled to a 2 mm $\times$ 1.7 mm area. Increasing the interface strength reduces the noise that helps in more precise detection of the substrate surface. This noise reduces with increasing difference in refractive indices between the two media (see supplementary information section 3.1, Figure 3.1). The tilt of the substrate could be manually corrected using the Piezo writing mode that further enhanced the pattern uniformity. The Piezo writing mode used in this study even though can increase uniformity by offsetting the substrate tilt, suffers from long printing times. The size of the pillars directly depends on the voxel dimensions that can be controlled via change in laser power, exposure time, and interface distance in the 2PP process. Our results are in agreement with the voxel scaling trends presented by Sun et al. [30]. Patterns that had an average diameter of about 200 nm for example, were less reproducible than those with larger dimensions. Even for pillar diameters of about 334 nm used in this study, pillar debonding, and the change in pillar diameters in certain regions can be seen. This can be primarily attributed to the laser fluctuations occurring at such small doses of energy. Factors such as humidity, temperature fluctuations, and vibrations also need to be accounted for at such scales.

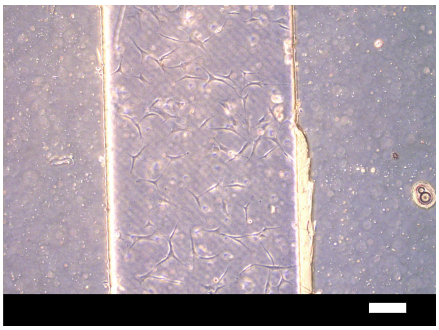

(a)

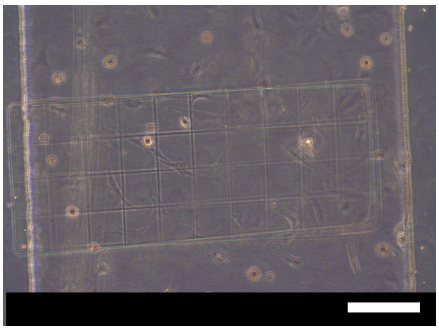

(b)

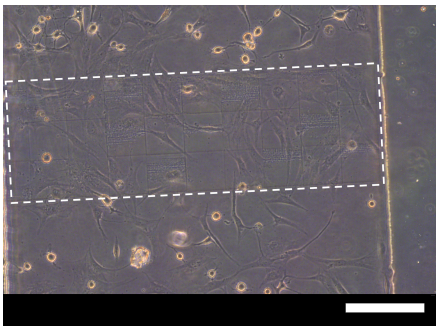

(c)

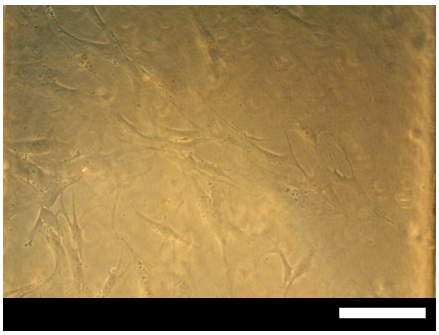

(d)

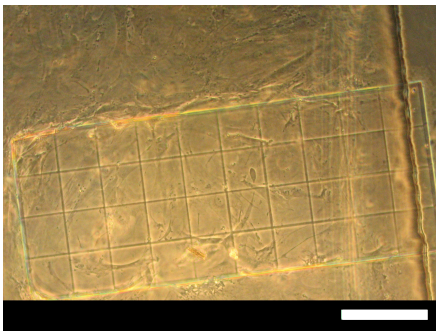

(e)

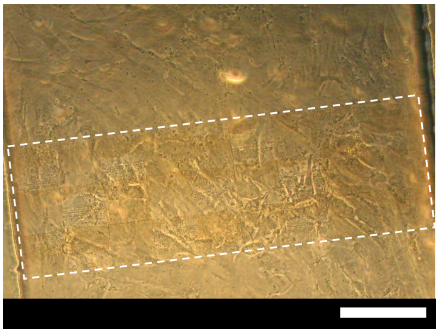

(f)

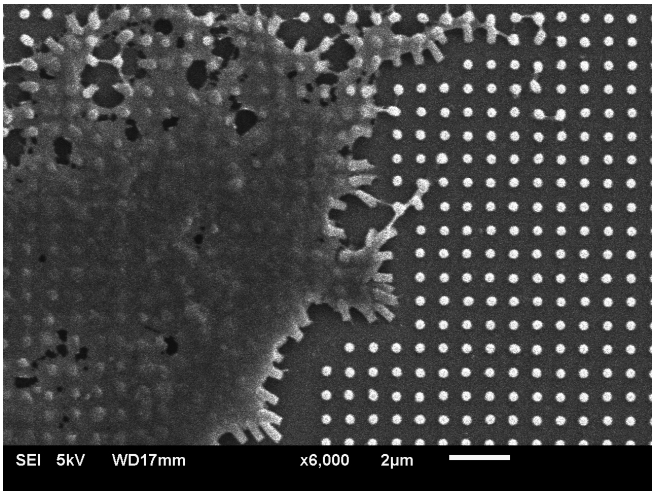

(g)

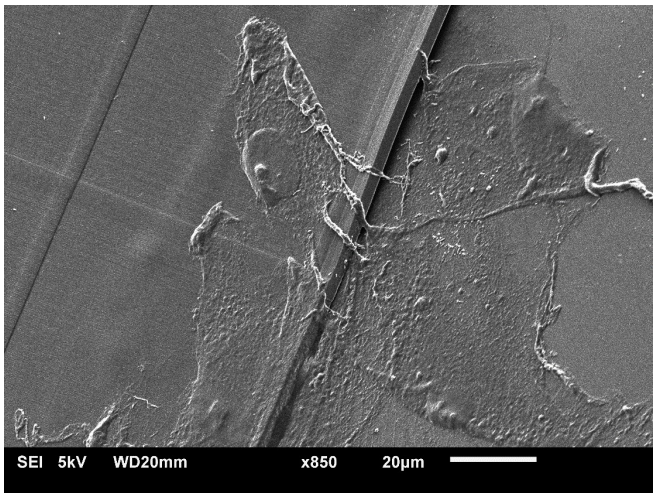

(h)

Figure 8: *Optical images of cells in channel on day 1(a-c) and day 5(d-f) and SEM images of cells on pattern (g) and flat sheet (h). Images (a) and (d) correspond to the control channel while images (b) and (e) and images (c) and (f) correspond to the flat sheet and patterned samples respectively. Images (a)-(f) shows the cells depicting a healthy, spread morphology on all samples. SEM image (g) depicts the cells exerting forces on the pillars causing them to bend and even delaminate. This sample used an ITO glass substrate as an exception (and was cultured statically in a petridish) Image (h) depicts cell filopodia extending around the sheet. Scale bar is 200 µm in images (a)-(f).*

4.2 Pattern upscaling and characterisation

The area based scaling of submicron pattern in this study depicts the long printing times involved in printing at such large scales. The method of imaging analysis used in the study exploits the optical phenomena occuring at the submicron scale and allows for an approximate way of characterising diameters of these topographies by merely looking at their optical images. This saves time by eliminating the need for examining the samples using SEM and sputtering them with gold beforehand. Sputtering can also affect cell response during biological evaluation studies. It also hampers device assembly when using plasma based bonding methods. This method of image analysis may however gives less accurate results owing to the image noise at low magnifications used. The use of a tungsten cathode based SEM in this study does not allow high resolution imaging below a few hundred nm. This can be improved by using a higher resolution SEM in the future.

Being able to print structures such as scaffolds with controlled submicron/nanotopography and porosity using 2PP opens new doors towards highly tunable biomaterial designs in the future. In this study, writing submicron pillars with variable heights onto a micro-scaffold demonstrates this concept. Being able to switch between Galvo and Piezo writing modes in a single process allowed realising this novelty in the study. However, it is difficult to write uniform submicron patterns onto large scale 3D (2PP) printed structures such as flat sheets and scaffolds in comparison to glass substrates. Enhancing uniformity of these patterns when writing on 2PP-fabricated structures requires calibrations to map the height and surface of these structures and identifying new pattern writing strategies accordingly.

4.3 Pattern increases substrate wettability

In literature, values in the range 60-85° have been reported for contact angle of water on ITO [31, 32, 33]. This variation indicates that the angle is highly senstive to factors such as contaminations, film thickness, and surface preparation methods. In our case, exposure to chemicals such as acetone, isopropanol, and PGMEA has been taken into account due to the sample development procedure involved. For homogenous patterns that are completely wetted by the droplet, the angle of contact is approximated by the Wenzel's model as:

$$cos\theta_w = Rcos\theta_y \tag{2}$$

Here, θ_w denotes the apparent contact angle of the droplet on the patterned surface while θ_y denotes the contact angle (Young's angle) for a smooth unpatterned surface [34]. R denotes the roughness factor of the surface and is defined as the ratio of the actual wetted area to the horizontally projected area (as if it was smooth). For our case assuming cylindrical pillars (for simplicity) of height h, diameter d, and centre to centre (interspacing) pitch p, the roughness factors can be derived as:

$$R = 1 + \frac{\pi dh}{p^2} \tag{3}$$

Substituting the dimensions from table 3 yields R = 3.49. Substituting these values into Wensel Equation 2 leads us to $\theta_w = 60.3°$. Hemiwicking, a phenomenon wherein a film develops over the pattern with the droplet sitting over the mixture of solid and liquid [35]. Hemiwicking requires the Young's angle to be smaller than a critical angle which is θ_c given as:

$$\theta_y < \theta_c = cos^{-1}\frac{1-\phi}{R-\phi} \tag{4}$$

Here ϕ denotes the fraction of the solid area within the liquid-solid interface area. For our assumed geometry, this is given as:

$$\phi = \frac{\pi d^2}{4p^2} \tag{5}$$

On substituting, the value of this critical angle is smaller than the Young's angle which applies to the Wenzel regime. The deviation seen in the experimental value of contact angle from the theoretically obtained Wenzel value can be attributed to the non-homogeneity in the pattern (Figure 5c shows that the pattern has regions that are non patterned and has pillars of varying dimensions due to process limitations) which can't be accounted for using this model. For simplicity, we also assumed the pillar geometry to be cylindrical rather than a truncated ellipsoid. The difference in the material properties of the pillars in comparison to the substrate also hasn't been considered in the model. Figure 9 depicts this deviation of the experimental values from the theoretical model. However, it does correctly predict that the hydrophilicity increases in such a case. An increase in surface hydrophilicity has been linked to enhanced proliferation and attachment of hMSCs [36, 37].

4.4 Estimating pillar adhesion

In this study it could only be established that wall shear stresses of few tens of N/m^2 is not enough to delaminate these pillars from the surface of the substrate. Figure 8g depicts pillars being bent and even delaminated due to the forces exerted by hMSCs on the pillars. The bending forces exerted by cells on a cylindrical pillar can be approximated from the relation:

$$\delta = \frac{4Fl^3}{3\pi Er^4} \tag{6}$$

where δ denotes the linear horizontal displacement of the pillar tip, F denotes the horizontal bending force, l = length of the pillar, r = pillar radius, and E = Young's modulus

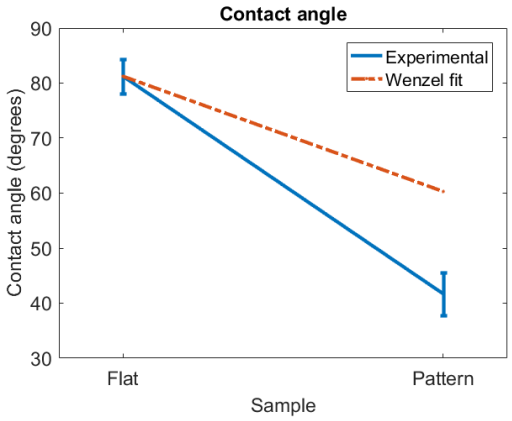

Figure 9: *Deviation of the experimental contact angle value from the Wenzel model*

of the polymeric material. This relation assumes a small displacement within the linear elastic regime. Observing SEM images of pillars and substituting δ in the order of a few hundred nm, E in the order of a few GPa [38], r = 167 nm, and l = 1.54 μm, yields forces in the order of hundreds of nN to a few μN. This estimated force range is in agreement with the values reported by Fu et al. [39]. The shear forces exerted on the pillars during the microfluidic flow studies are approximated by:

$$F_s = \tau \pi r^2 \tag{7}$$

Here the shear stress τ acting on the pillar has been approximated as the wall shear stress (given in Equation 1). The drag forces in this case were found to be in the order of 10^{-18}N and hence neglected. The complex flow profiles and impact forces that may originate due to pillar arrays also haven't been considered. The viscosity therefore leads us to forces in the pN scale. These forces are much smaller in magnitude than those exerted by cells on the pillars, therefore justifying the non-delamination of pillars in the former case. It is therefore crucial to improve the adhesion of these pillars for cell studies to the substrate by either scaling up their diameter or reducing their length. A higher interface distance starts the printing process deeper into the substrate and may also be effective in enhancing pillar adhesion. Coating the substrate surface with a layer to help enhance the pillar adhesion or looking at other resins might also be an option in the future. The adhesion of more complex structures such as scaffolds also needs to evaluated in further studies.

4.5 Microfluidic device design and its cytocompatibility

The 3D printed moulds fabricated using stereolithography in this study provide a low cost possibility to vary channel dimensions and design. A mechanical clamp has been used for fixing PDMS on top of ITO coated glass for the pillar delamination studies. This could not be done for biological studies given the handling problems with this method. A clamp also poses hindrance in imaging the samples microscopically. In the future, other bonding methods such as UV-Ozone plasma may be tried to observe if it yields a better bond strength than air plasma. Glues should be avoided since they can be cytotoxic and affect cell response. In case of integrated devices manufactured for the cell studies, after the plasma bonding procedure, no noticeable damage to the patterns was observed.

This study paves the way for future experiments aimed at predicting the optimal pattern size and arrangement that can enhance osteogenesis. The absence of any visible signs of cell death in the initial studies also suggest the potential application of the selected materials for biological studies. Both IP-L 780 and IP-Dip resins did not seem to show any detrimental effects on cell behaviour. This has also been found in similar studies but involved coating the structures with biocompatible layers (such as TiO_2, collagen, fibronectin) [26, 40, 41]. However, in this study no claims regarding cell preference towards control (glass), unpatterned (sheet), or the patterned areas can be made. Further studies in terms of a larger sample number and longer culture times are needed to draw any conclusive biological results.

5 Conclusions and Perspectives

In this work, we have used the 2PP process to produce uniform submicron topographies that have been incorporated into microfluidic platforms for bone regeneration based studies. To do so, we used the DiLL configuration (IP-Dip with ITO coated fused silica) to enhance interface detection and a Piezo mode based voxel by voxel writing strategy to compensate for the substrate tilt within the process. In this way, the printed areas have been upscaled to the mm scale. The patterns have been morphologically characterised by calibrating their optical images with their SEM micrographs. This provides an approximate quantification of pillar dimensions for patterns produced over large areas. They have also been integrated onto a 2PP written micro-scaffold in a single step process by alternately printing scaffold and pattern layers. These topographies have been integrated into the microfluidic device by mechanically clamping a PDMS channel layer over the patterned ITO coated substrate or using air plasma bonding in case of non coated fused silica substrate.

The printed pillars in this study are ellipsoidal in shape and showed an average diameter of 334 nm, and a height of 1.54 μm with an interspacing of 800 nm for the chosen writing parameters. The patterns significantly increased the substrate wettability of ITO coated fused silica. The pillars showed no signs of delamination even when flow rates were increased up to 8 ml/min. hMSCs when dynamically cultured for 5 days on these patterns in a microfluidic device, showed a healthy morphology with no significant signs of cytotoxicity. This study therefore marks a crucial step in using the 2PP process for fabricating biomaterials with reproducible and upscalable topographies having minimum feature sizes in the submicron scale. Our work also depicts that these 2PP fabricated structures can be conveniently integrated into microfluidic cell cultures that have the potential for successfully mimicking and studying the bone tissue microenvironment.

As discussed, the 2PP process holds the potential in successfully recreating the topographical make-up of the bone tissue by helping to optimise the feature sizes, their spatial layout, and their expansion at a multiscale level. The dependence of polymer's Young's modulus on laser parameters may be further exploited to tune the biomaterial properties (and hence the cellular microenvironment) in the future but it should be remembered that a change in laser parameters would also lead to a direct change in the feature sizes at this scale. The 2PP method is unable to fabricate (uniform) nanometre scale features thus suffering from lower print resolution than methods such as electron beam and focussed ion beam lithography. This is further limited by the decrease in pattern uniformity with reducing feature sizes. The long printing times (in Piezo writing mode) are not ideal for large production volumes but can be useful for rapid prototyping and laboratory based applications. Also, in such cases, 2PP would prove to be more cost effective in comparison to methods such as electron beam lithography that require expensive masks. A large number of parameters are involved in the 2PP process that need to optimised each time the pillar dimensions or interspacing need to be changed thus making the process tedious to some extent. New printing materials also need to be looked at to further increase the pattern uniformity. With respect to the microfluidic device, methods for bonding ITO to PDMS need to looked at in addition to designs that'd allow topography integration into complex co-culture based microenvironments.

References

[1] Rozalia Dimitriou, Elena Jones, Dennis McGonagle, and Peter V Giannoudis. Bone regeneration: current concepts and future directions. *BMC Medicine*, 9(1):66, 2011.

[2] Laurent Audigé, Damian Griffin, Mohit Bhandari, James Kellam, and Thomas P Rüedi. Path analysis of factors for delayed healing and nonunion in 416 operatively treated tibial shaft fractures. *Clinical orthopaedics and related research*, 438:221–32, sep 2005.

[3] Jan Henkel, Maria A. Woodruff, Devakara R. Epari, Roland Steck, Vaida Glatt, Ian C. Dickinson, Peter F. M. Choong, Michael A. Schuetz, and Dietmar W. Hutmacher. Bone Regeneration Based on Tissue Engineering Conceptions — A 21st Century Perspective. *Bone Research*, 1(3):216–248, 2013.

[4] Tao Gong, Jing Xie, Jinfeng Liao, Tao Zhang, Shiyu Lin, and Yunfeng Lin. Nanomaterials and bone regeneration. *Bone Research*, 3(July):15029, 2015.

[5] Liliana Polo-Corrales, Magda Latorre-Esteves, and Jaime E Ramirez-Vick. Scaffold design for bone regeneration. *Journal of nanoscience and nanotechnology*, 14(1):15–56, jan 2014.

[6] Larry L Hench and Julia M Polak. Third-generation biomedical materials. *Science (New York, N.Y.)*, 295(5557):1014–7, feb 2002.

[7] Sonja Kress, Anne Neumann, Birgit Weyand, and Cornelia Kasper. Stem Cell Differentiation Depending on Different Surfaces. In *Advances in biochemical engineering/biotechnology*, volume 126, pages 263–283. 2011.

[8] Anh Tuan Nguyen, Sharvari R Sathe, and Evelyn K F Yim. From nano to micro: topographical scale and its impact on cell adhesion, morphology and contact guidance. *Journal of Physics: Condensed Matter*, 28(18):183001, may 2016.

[9] B Wójciak-Stothard, Zbigniew Madeja, Wlodzimierz Korohoda, Adam Curtis, and Christopher Wilkinson. Activation of macrophage-like cells by multiple grooved substrata. Topographical control of cell behaviour. *Cell Biology International*, 19(6):485–490, jun 1995.

[10] Matthew J Dalby, Mathis O Riehle, Stephen J Yarwood, Chris D W Wilkinson, and Adam S G Curtis. Nucleus alignment and cell signaling in fibroblasts: response to a micro-grooved topography. *Experimental cell research*, 284(2):274–82, apr 2003.

[11] Sander Dobbenga, Lidy E. Fratila-Apachitei, and Amir A. Zadpoor. Nanopattern-induced osteogenic differentiation of stem cells – A systematic review. *Acta Biomaterialia*, 46:3–14, 2016.

[12] C. Vieu, F. Carcenac, A. Pépin, Y. Chen, M. Mejias, A. Lebib, L. Manin-Ferlazzo, L. Couraud, and H. Launois. Electron beam lithography: resolution limits and applications. *Applied Surface Science*, 164(1-4):111–117, sep 2000.

[13] Vitor R. Manfrinato, Lihua Zhang, Dong Su, Huigao Duan, Richard G. Hobbs, Eric A. Stach, and Karl K. Berggren. Resolution Limits of Electron-Beam Lithography toward the Atomic Scale. *Nano Letters*, 13(4):1555–1558, apr 2013.

[14] Tushar Kumeria, Abel Santos, and Dusan Losic. Nanoporous Anodic Alumina Platforms: Engineered Surface Chemistry and Structure for Optical Sensing Applications. *Sensors*, 14(7):11878–11918, 2014.

[15] Stefan Walheim, Martin Bo, Ju Ltau, Rgen Mlynek, Georg Krausch, and Ullrich Steiner. Structure Formation via Polymer Demixing in Spin-Cast Films.

[16] Abhijit Biswas, Ilker S. Bayer, Alexandru S. Biris, Tao Wang, Enkeleda Dervishi, and Franz Faupel. Advances in top–down and bottom–up surface nanofabrication: Techniques, applications & future prospects. *Advances in Colloid and Interface Science*, 170(1-2):2–27, jan 2012.

[17] Byron D. Gates, Qiaobing Xu, Michael Stewart, Declan Ryan, , C. Grant Willson, and George M. Whitesides. New Approaches to Nanofabrication:Molding, Printing, and Other Techniques. 2005.

[18] Stephen Y Chou, Peter R Krauss, Wei Zhang, Lingjie Guo, and Lei Zhuang. Sub-10 nm imprint lithography and applications.

[19] J Damon Hoff, Li-Jing Cheng, Edgar Meyho, L Jay Guo, and Alan J Hunt. Nanoscale Protein Patterning by Imprint Lithography.

[20] Manuela T. Raimondi, Shane M. Eaton, Michele M. Nava, Matteo Laganà, Giulio Cerullo, and Roberto Osellame. Two-photon laser polymerization: from fundamentals to biomedical application in tissue engineering and regenerative medicine. *Journal of Applied Biomaterials & Biomechanics*, 10(1):0–0, 2012.

[21] Boris N Chichkov and Andreas Ostendorf. Two-Photon Polymerization: A New Approach to Micromachining. *Photonics Spectra*, 40(October):72–79, 2006.

[22] Xian-Zi Dong, Zhen-Sheng Zhao, and Xuan-Ming Duan. Improving spatial resolution and reducing aspect ratio in multiphoton polymerization nanofabrication. *Applied Physics Letters*, 92(9):091113, mar 2008.

[23] Sangeeta N Bhatia and Donald E Ingber. Microfluidic organs-on-chips. *Nature Biotechnology*, 32(8):760–772, 2014.

[24] Joung Hyun Lee, Yexin Gu, Hongjun Wang, and Woo Y. Lee. Microfluidic 3D bone tissue model for high-throughput evaluation of wound-healing and infection-preventing biomaterials. *Biomaterials*, 33(4):999–1006, 2012.

[25] Masoomeh Tehranirokh, Abbas Z. Kouzani, Paul S. Francis, and Jagat R. Kanwar. Microfluidic devices for cell cultivation and proliferation. *Biomicrofluidics*, 7(5):051502, sep 2013.

[26] Michele M. Nava, Nunzia Di Maggio, Tommaso Zandrini, Giulio Cerullo, Roberto Osellame, Ivan Martin, and Manuela T. Raimondi. Synthetic niche substrates engineered via two-photon laser polymerization for the expansion of human mesenchymal stromal cells. *Journal of Tissue Engineering and Regenerative Medicine*, (June 2016):2836–2845, 2016.

[27] A. Ovsianikov, M. Malinauskas, S. Schlie, B. Chichkov, S. Gittard, R. Narayan, M. Löbler, K. Sternberg, K. P. Schmitz, and A. Haverich. Three-dimensional laser micro- and nano-structuring of acrylated poly(ethylene glycol) materials and evaluation of their cytoxicity for tissue engineering applications. *Acta Biomaterialia*, 7(3):967–974, 2011.

[28] Claudia Bruedigam, Marjolein van Driel, Marijke Koedam, Jeroen van de Peppel, Bram C.J. van der Eerden, Marco Eijken, and Johannes P.T.M. van Leeuwen. Basic Techniques in Human Mesenchymal Stem Cell Cultures: Differentiation into Osteogenic and Adipogenic Lineages, Genetic Perturbations, and Phenotypic Analyses. *Current Protocols in Stem Cell Biology*, 17(1):1H.3.1–1H.3.20, jun 2011.

[29] Bu Wang, Alex L. Weldon, Pisist Kumnorkaew, Bu Xu, James F. Gilchrist, and Xuanhong Cheng. Effect of surface nanotopography on immunoaffinity cell capture in microfluidic devices. *Langmuir*, 27(17):11229–11237, 2011.

[30] Hong-Bo Sun, Tomokazu Tanaka, and Satoshi Kawata. Three-dimensional focal spots related to two-photon excitation. *APPLIED PHYSICS LETTERS*, 80:3673.

[31] Zhiyou Zhong, Youxin Zhong, Chen Liu, Sheng Yin, Wuxing Zhang, and Dufang Shi. Study on the surface

wetting properties of treated indium-tin-oxide anodes for polymer electroluminescence devices. *Physica Status Solidi (A) Applied Research*, 198(1):197–203, 2003.

[32] Rakesh A. Afre, Yasuhiko Hayashi, and Tetsuo Soga. Enhanced photovoltaic device performance upon modification of indium tin oxide coated glass by liquid nitrogen treatment. *Journal of Physics D: Applied Physics*, 42(4), 2009.

[33] Ming Hua Piao, Dae Soo Yang, Kuk Ro Yoon, Seung Ho Lee, and Seong Ho Choi. Development of an electrogenerated chemiluminescence biosensor using carboxylic acid-functionalized MWCNT and Au Nanoparticles. *Sensors*, 9(3):1662–1677, 2009.

[34] David Quéré. Wetting and Roughness. *Annual Review of Materials Research*, 38(1):71–99, 2008.

[35] Elena Martines, Kris Seunarine, Hywel Morgan, Nikolaj Gadegaard, Chris D.W. Wilkinson, and Mathis O. Riehle. Air-trapping on biocompatible nanopatterns. *Langmuir*, 22(26):11230–11233, 2006.

[36] Somruthai Tunma, Kewalin Inthanon, Chanokporn Chaiwong, Jantrawan Pumchusak, Weerah Wongkham, and Dheerawan Boonyawan. Improving the attachment and proliferation of umbilical cord mesenchymal stem cells on modified polystyrene by nitrogen-containing plasma.

[37] B.D. Boyan, A. Cheng, R. Olivares-Navarrete and Z. Schwartz. Implant Surface Design Regulates Mesenchymal Stem Cell Differentiation and Maturation. *Advances in Dental Research*, 28(1):10–17, 2016.

[38] Enrico Domenico Lemma, Francesco Rizzi, Tommaso Dattoma, Barbara Spagnolo, Leonardo Sileo, Antonio Qualtieri, Massimo De Vittorio, and Ferruccio Pisanello. Mechanical Properties Tunability of Three-Dimensional Polymeric Structures in Two-Photon Lithography. *IEEE Transactions on Nanotechnology*, 16(1):23–31, 2017.

[39] Jianping Fu, Yang-Kao Wang, Michael T Yang, Ravi A Desai, Xiang Yu, Zhijun Liu, and Christopher S Chen. mechanical regulation of cell function with geometrically modulated elastomeric substrates. 2010.

[40] Rainer Wittig, Erik Waller, Georg von Freymann, and Rudolf Steiner. Direct laser writing-mediated generation of standardized topographies for dental implant surface optimization. *Journal of Laser Applications*, 24(4):042011, 2012.

[41] Barbara Spagnolo, Virgilio Brunetti, Godefroy Leménager, Elisa De Luca, Leonardo Sileo, Teresa Pellegrino, Pier Paolo Pompa, Massimo De Vittorio, and Ferruccio Pisanello. Three-dimensional cage-like microscaffolds for cell invasion studies. *Scientific Reports*, 5(1):10531, 2015.

3

Supplementary information

3.1. Enhancing the interface strength

The interface signal amplitude between the substrate and resin increased on switching from conventional (IP-L 780 and borosilicate glass) to the DiLL configuration (IP-Dip and fused silica glass). This value is further seen to increase on using an Indium Tin Oxide (ITO) layer coated fused silica substrate. The increase in the interface can be attributed to the increase in the difference between the refractive indices of the substrate and the resin (Δn). Table 3.1 shows the refractive indices of these materials at 780 nm while table 3.2 shows the increase in measured interface signal amplitude with increasing Δn.

Table 3.1: *Refractive indices of optical media in 2PP at 780 nm*

Material	**Refractive index (780 nm)**	**Reference**
IP-L 780	1.48	[94]
IP-Dip	1.52	[94]
Fused silica glass	1.46	[95]
Borosilicate glass	1.52	[95]
Indium Titanium Oxide	1.62	[95]

Table 3.2: *Interface signal amplitudes and their scaling with difference in refractive indices* $|\Delta n|$

Configuration	$\|\Delta$**n**$\|$	**Interface signal amplitude**
Conventional (IPL, Borosilicate glass)	0.04	300 - 400
DiLL (IP-Dip, Fused silica glass)	0.06	600 - 700
DiLL (IP-Dip, ITO coated fused silica)	0.1	4000 - 6000

3.1.1. Enhanced interface allows better surface detection

An experiment to quantify the error in measurement that occurs while detecting the interface is carried out. The interface surface is plotted using the z height measurements (using a method similar to tilt measurement see section 3.2) as a function of x and y coordinates over the substrates. The surface is obtained by plotting these points in MATLAB. Next, a linear plane of the form:

$$z_0 = a_0 + a_1 x + a_2 y \tag{3.1}$$

is fitted onto the surface. This is done assuming that the substrate surfaces are perfectly flat with a constant tilt in x and y directions. The goodness of fit for all the three cases namely:

- Conventional configuration: IPL-780 + Borosilicate glass
- DiLL configuration: IP-Dip + Fused silica glass

- DiLL configuration: IP-Dip + Fused silica glass coated with ITO

is calculated using MATLAB. The sum of the squares of residuals or errors (SSE) is chosen in this case as a measure of assessing the goodness. The SSE is given as:

$$SSE = \sum_{i=1}^{k} (z - z_0)^2 \tag{3.2}$$

where z is the actual z height of the point, and z_0 is the fitted value. k represents the number of independent points on the surface. In this case, k takes a value of 33 (for 36 measurement points). It can be clearly seen via table 3.3 that the error increases from IP-Dip + ITO configuration towards fused silica. The measurements are made twice for each sample. The error further increases on moving towards the conventional mode. This is indicative of the effect of the interface strength on the interface detection. This is also plotted in figure 3.1. This quantitative trend relates to the worsening of the pattern quality as the interface signal amplitude decreases. The choice of using IP-Dip + ITO coated glass is thus justified in the current study.

Configuration	**SSE$_1$**	**SSE$_2$**
IPL-780 and Borosilicate glass	432	198.6
IP-Dip and Fused silica glass	22.7	21.7
IP-Dip and ITO coated glass	16.2	16.8

Table 3.3: *Correlating interface strength to the error in surface detection. The error measurement was performed twice.*

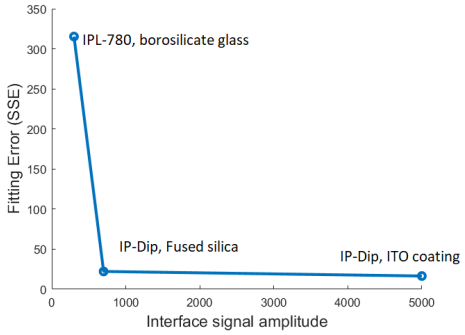

Figure 3.1: *Average interface detection error decreases with increasing signal amplitude*

3.1.2. Pattern quality: Conventional to DiLL (fused silica)

A change in configuration type conventional (IP-L 780, borosilicate glass) to DiLL (IP-Dip, fused silica) increased the interface signal amplitude from approximately 300-350 to 600-700. The change in pattern quality is shown in Figure 3.2. Using the IP-Dip resin in combination with fused silica increased the feasible printed area as well as the print uniformity. This has not been quantified here. Samples in both cases have been written in the Piezo mode and corrected against tilt in this case. A laser power of 32 mW and an exposure time of 2000 μs was used in both cases. Hence, this comparison does not take different properties of IP-L 780 into account.

3.1.3. Effect of ITO coating on fused silica glass

Using the ITO glass instead of a normal fused silica greatly enhanced the pattern quality. The interface signal amplitude increased from 600-700 to about 5000-6000. Figure 3.3 shows the improvement in pattern quality in this case for the Piezo writing strategy. Using the method discussed to measure pattern uniformity, there is an increase of about 15% in this case. Both the patterns have been corrected for tilt in this case. A laser power of 27.2 mW, an exposure time of 2400 μs and an interface distance of 0.3 μm was used in both cases.

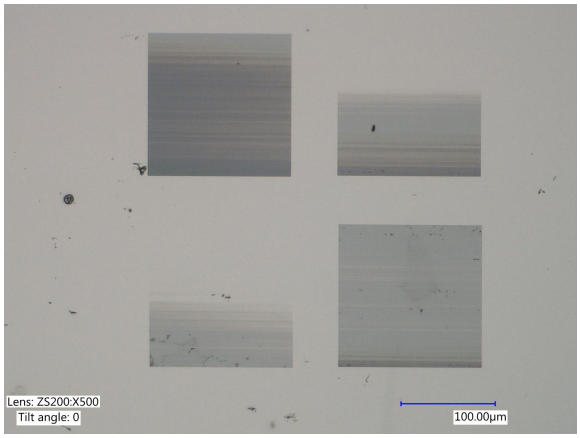

(a) *Printing in conventional mode on borosilicate glass using IP-L 780 using the Piezo writing strategy*

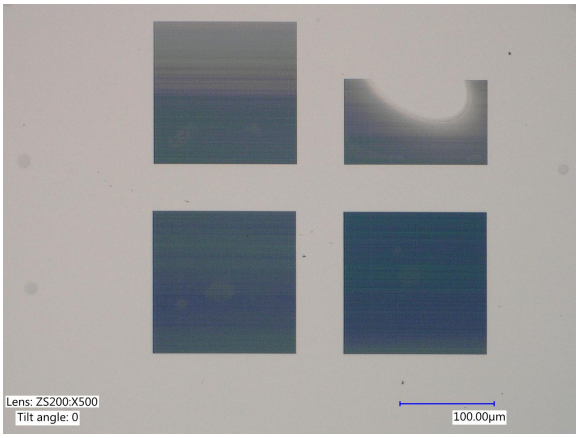

(b) *Printing in DiLL mode on fused silica glass using IP-Dip using the Piezo writing strategy. Different properties of the resins have not been considered here.*

Figure 3.2: *Increase in pattern uniformity upon transition conventional to DiLL configuration*

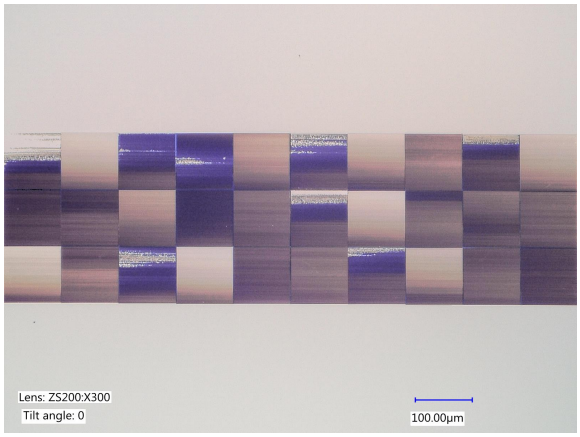

(a) *Print quality on fused silica glass in DiLL mode*

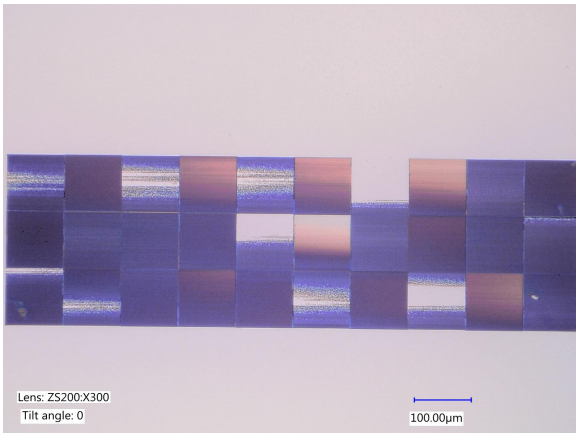

(b) *Pattern quality on ITO coated fused silica in DiLL mode*

Figure 3.3: *Increase in pattern quality on using ITO coated fused silica (by about 15%) in comparison to a normal fused silica substrate*

3.2. Writing mode and tilt correction strategy

3.2.1. Transition from Galvo to Piezo writing mode

Printing in the Galvo mode is much faster than Piezo mode due to writing in a pointwise voxel by voxel (or point by point) fashion in the latter case in comparison to the angular motion of the laser scanner involved in the former. The Piezo settling time that allows the piezoelectric element's vibrations to die down adds further to the total writing time. The Galvo mode doesnot allow tilt correction since it is controlled by a galvanometric scanner. This is possible in the Piezo mode. This is the reason why we chose the latter mode for our intended application since it allows the possibility to correct for this error. Figure 3.4 shows the improvement in pattern quality (qualitatively) on a transition from Galvo to Piezo writing mode.

The laser parameters in both cases have been adjusted to yield the similar pillar diameters (proximately 300-350 nm). However, the heights in the two cases were not equalised. Writing in the Galvo mode requires a scan speed parameter instead of a time of exposure (as in case of Piezo mode). The Galvo mode also involves non-linear interaction between various voxels hence requiring different writing parameters than the Piezo mode. The Galvo mode written structures show a smooth gradient (in the writing direction) while in Piezo mode even the variations are rather abrupt (but perpendicular to the direction of writing). This effect becomes especially visible at the boundaries of stitched regions during large area patterning in the Galvo mode. This difference in pillars can be clearly observed in figure 3.5. A laser power of 9 mW and a scan speed of 1000 μm/s were used in this case.

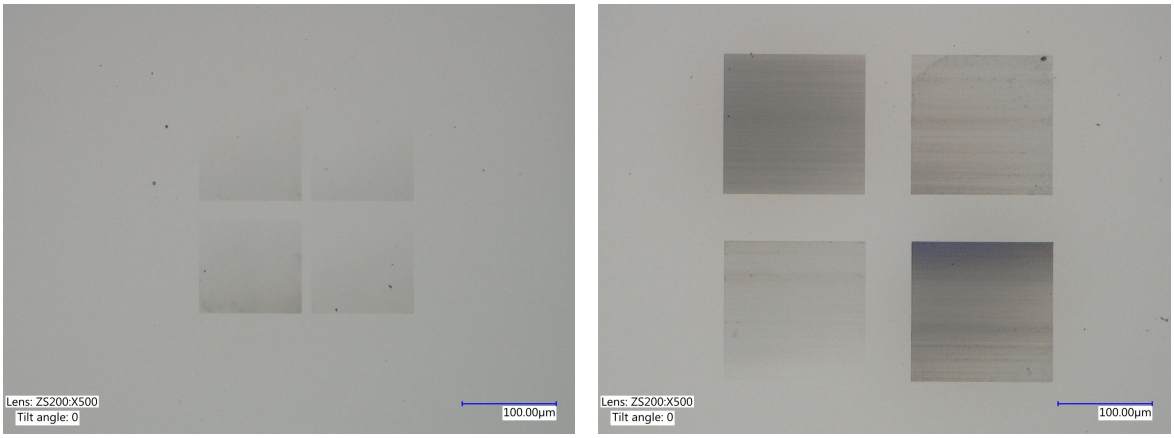

(a) *Printing in conventional mode on borosilicate glass using IP-L 780 using the Galvo writing strategy*

(b) *Printing in conventional mode on borosilicate glass using IP-L 780 using the Piezo writing strategy*

Figure 3.4: *Increase in pattern quality due to the tilt correction in allowed Piezo mode while this is not the case in the Galvo mode. In figure (b), the sample has been corrected for tilt.*

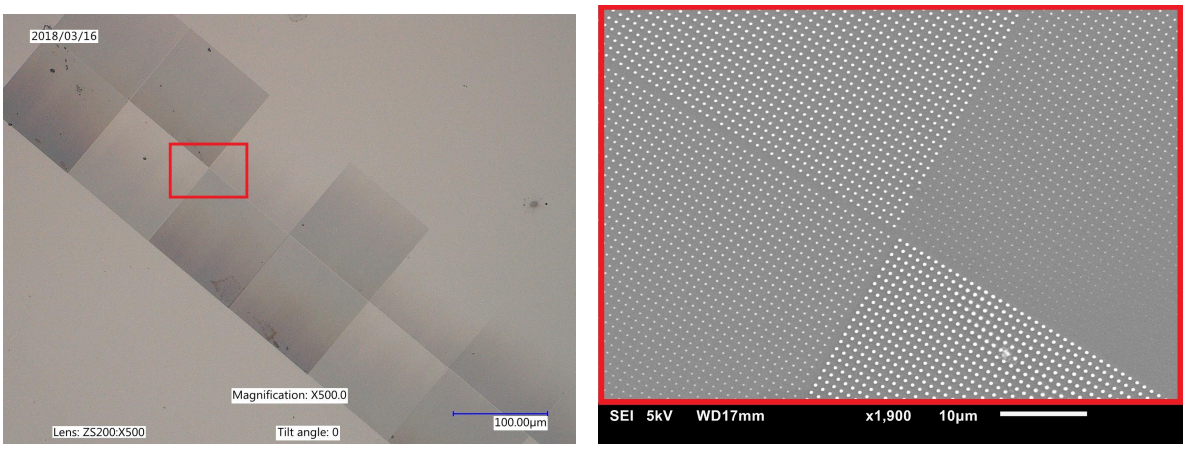

(a) *Optical image of a large area pattern printed using Galvo mode*

(b) *SEM image of the boundary region shown in a red box in figure(a)*

Figure 3.5: *Variation in pillar dimensions at the stitching boundaries of pattern (printed via Galvo mode) with optical image in (a) and a zoomed in SEM image in (b). At boundaries, the Galvo scanner finishes scanning a particular block and starts printing a new one causing the pronounced variation in dimensions.*

3.2.2. Tilt correction and its effect

In Piezo mode, the machine displays the tilt of the sample in x and y directions and manipulates the z coordinate of the Piezo element accordingly to compensate for these tilts. However, it was found that the tilt values measured by the machine were not repeatable (even for the same sample) and hence produced unsatisfactory results. This led to devising a method to measuring the tilt of the sample manually. For the 25mm × 25 mm × 0.7 mm ITO coated fused silica sample, a 6×6 grid of equally spaced points was selected spanning across the substrate. This is shown in figure 3.6. It is not possible to measure tilt over a larger area due to hardware limitations. The z position of the Piezo was measured at these points to obtain the tilt angles of substrate along x and y directions. The averages of tilts in x and y were taken respectively to yield these tilt values.

Figure 3.7 shows a clear contrast in the uniformity of the pattern obtained with and without tilt compensation as well as on using the auto tilt feature. This is done for laser power 27.2 mW and time of exposure 2400 μs. Manual tilt calibration is thus needed to improve the pattern uniformity.

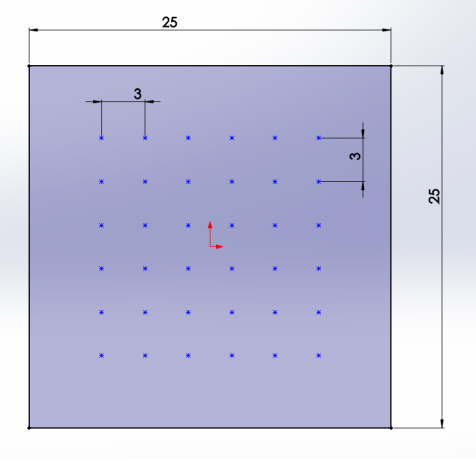

Figure 3.6: *Selecting points for tilt measurement. All dimensions in mm*

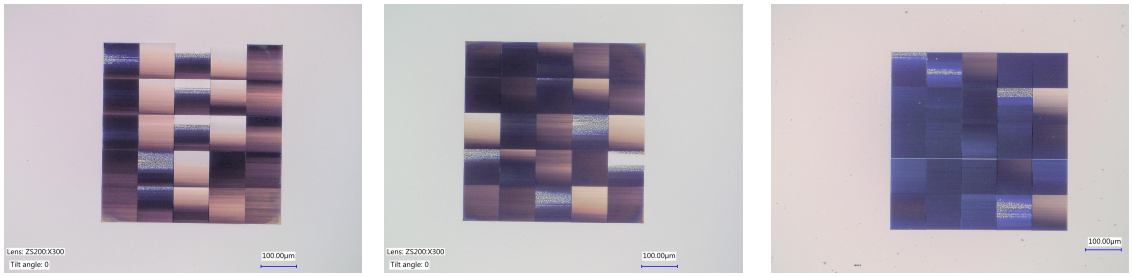

(a) *Pattern produced without any tilt correction*

(b) *Pattern produced using the auto-tilt correction mode*

(c) *Pattern produced using manual tilt correction*

Figure 3.7: *Increase in pattern quality on correcting the sample tilt. In this case, this is done for IP-Dip and ITO glass combination.*

3.3. Parametric optimisation in DiLL mode

3.3.1. Scaling of pillar dimensions with writing parameters

In the DiLL mode configuration using IP-Dip resin in combination with ITO glass, the scaling of pillar dimensions (mean diameter and height) with respect to laser parameters (laser power and time of exposure) and interface distance was studied. Figure 3.8 shows the dependence of pillar dimensions on laser power and time of exposure. The measurement are done at a constant interface distance of 0.1 μm in this case. The pillar height as well as diameters increase with increasing power and exposure times.
The dependence of pillar diameter on interface distance is not monotonically decreasing (as shown in Figure 3.9a). However, the dependence of height shows a decreasing linear trend (Figure 3.9b). The laser power and exposure time were fixed at 14.4 mW and 1600 μs respectively. The error bar denotes two standard deviations in both cases (figures 3.8,3.9).

3.3.2. Effect of writing parameters on pattern uniformity

A change in laser power leads to a change in the voxel dimesions thus leading to a change in pillar diameter and height. 3.10 depicts the change in the pattern colour (which is directly related to the pillar dimensions) when the laser power decreases from left to right. The time of exposure is kept at 2400 μs for all the patterns while the interface at 0.3 μm, and the pillar centre to centre interspacing at 800 nm. It is interesting to note that the percentage of printed area also decreases as the laser power is decreased. The percentage of fallen pillars is also increasing in a similar fashion. The percentage feasible area is thus decreasing from (a) to (d), indicating the dominating effect of laser fluctuations at lower laser powers.

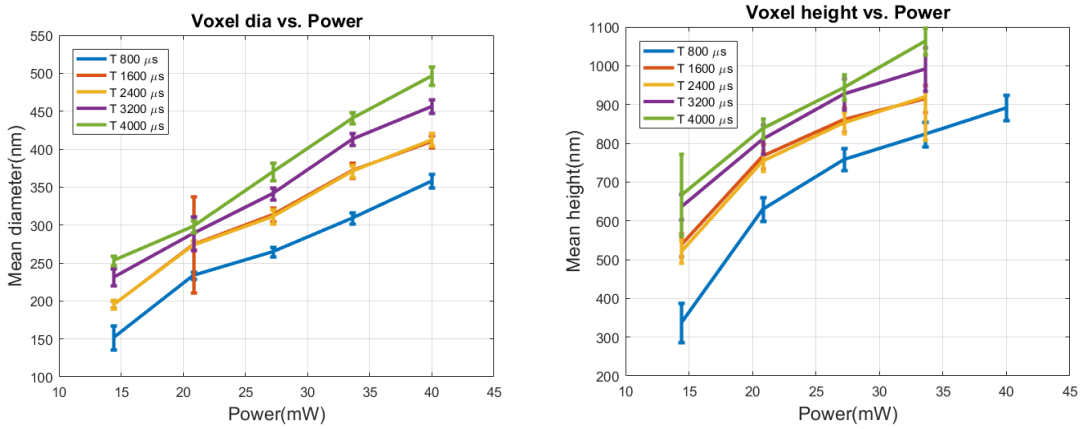

(a) *Increasing pillar diameter with laser power (mW) for different times of exposure, T (μs)*

(b) *Increasing pillar height with laser power (mW) for different times of exposure, T (μs)*

Figure 3.8: *Parametric study of pillars with laser parameters*

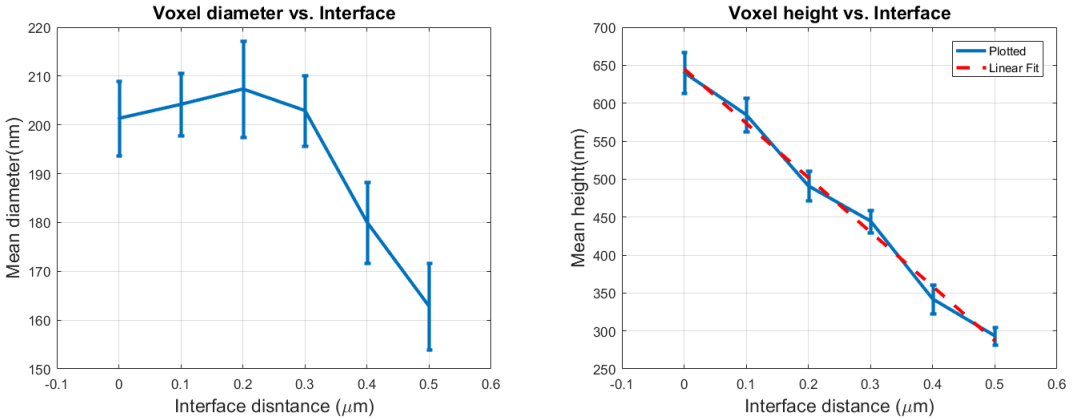

(a) *Effect of interface distance on pillar diameter*

(b) *Effect of interface distance on pillar height*

Figure 3.9: *Parametric study of pillars dimension scaling with interface distance*

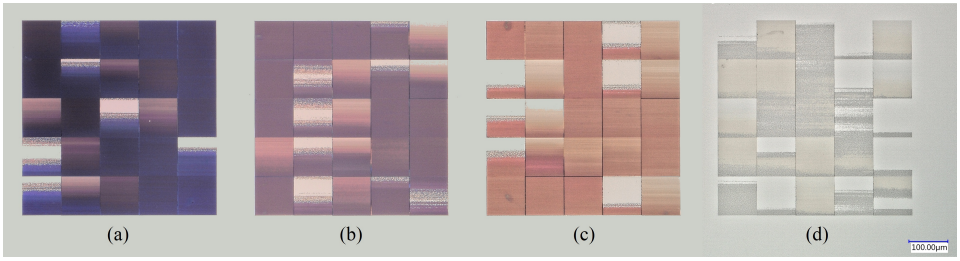

Figure 3.10: *Change in pattern optical image with laser power in Piezo writing mode. The change in pattern colour depicts a variations in pillar dimensions. For smaller pillar dimensions (towards right), the pattern uniformity decreases.*

Pattern label	**Laser power (*m*W)**
a	27.2
b	24
c	20.8
d	14.4

Table 3.4: *Laser powers used for printing in Figure 3.10*

The pattern quality is also dependent on the change in interface distance. This is the distance between

the first voxel and the boundary between the substrate and the resin. In figure 3.11, the interface distance increases from *a* to *d* thus causing writing procedure to start further below the actual interface. Table 3.5 shows the interface values used for the study. A laser power of 14.40 *m*W, time of exposure of 2400 μs, and center to center pillar distance of 600 nm were used. It can be seen that the pattern uniformity decreases with large unwritten areas appearing on increasing the interface distance. On making the interface distance smaller (right to left), areas containing eroded pillar can be seen thus indicating an insufficient attachment.

Pattern label	**Interface distance (μm)**
a	0.1
b	0.3
c	0.6
d	0.8

Table 3.5: *Interface distance values used for printing in Figure 3.11*

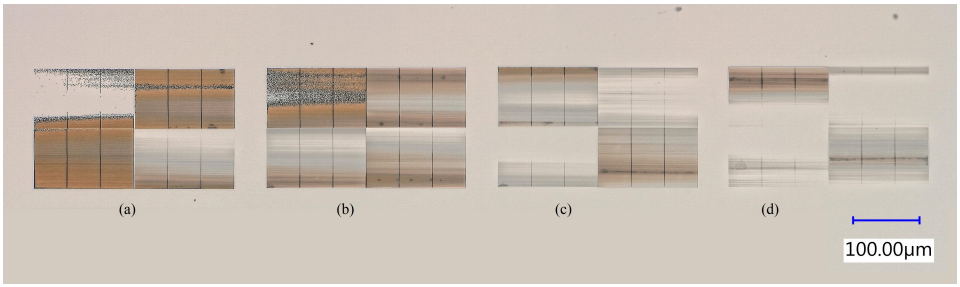

Figure 3.11: *Decrease in pattern uniformity with increasing interface distance in Piezo writing mode*

A

Fabrication of topography

A.1. Writing modes and configurations

The aim was to produce features of minimum possible size and later expanding these topographies over a larger areas. It was later realised that the latter goal is interlinked to the former requirement. This is similar to an optimisation problem where the minimum feature and reproducibility in printing counter each other. To start with, it is important to know that the Nanoscribe operates in two **writing modes** namely:

1. **Galvo mode**: Here the laser sweeps over the resin along an angular path (in X-Y Plane) using a galvanometric mirror scanner. This allows much faster printing than the piezo writing mode.

2. **Piezo mode**: The piezo mounted on the stage moves in this case. This provides a much higher resolution in movement but the writing speeds are drastically reduced. This mode allows for compensating the tilt of the substrate and thus can be used to the improve print quality.

The stage scanning is used to move the stage once certain structures have been written and the range of writing for the galvo or piezo modes have been exceeded. A typical writing procedure thus involves writing within a certain bounded area using the galvo or piezo mode and then once the permissible writing limit of this area has been reached, the stage is moved to another location and the piezo or galvo mode operation are repeated. Writing in this fashion helps in printing large area patterns using the so-called **Stitching Technique**. It is also worth noting that the Nanoscribe operates in two **configuration modes** (applicable to this study) namely:

1. **Conventional mode**: In this mode, the lower side of the substrate is coated with an oil matching the refractive index of the substrate while the upper face is coated with the photo-polymerisable resin. This allows writing structures in the upward direction. Spherical abberations are a problem to be acounted for in this mode when writing tall structures. The IP-L 780 resin is used in combination with printing oil in this case on a borosilicate glass cover slips.

2. **Dip-in laser lithography (DiLL) mode**: In this case, the photosensitive polymer is place on the bottom face of the substrate an the objective lens dips in directly into this polymer. The writing thus takes place in the downward direction. This mode thus reduces aberration errors due to a single refractive interface involved. The IP-Dip resin is popularly used in this case for producing small feature sizes in combination with fused silica glass (for 63X objective).

A.2. Conventional configuration

A.2.1. Galvo writing mode

Studies were carried out across different writing as well configuration modes to find the minimal feature sizes. The Galvo scan mode was evaluated for the conventional writing configuration (IP-L 780 with borosilicate glass). Pillars of diameter 200 nm were designed in Solidworks and fabricated using different scan speeds and laser powers. Parameters such as the slicing and hatching distances of the pillars were kept constant at 100 nm. Pillars ranging from a mean diameter of 180 nm to about 500 nm were obtained. Below this range,

the pillars were not printed due to too low laser doses while above this range, the pillars were burnt due to the laser dose being too high. This is depicted in figure A.1a. Error bars indicate the standard deviation in measurements made for 25 pillars. It can be seen that the diameter increases monotonically with power and scan speed in the given range. It is also seen that the pillars become elliptical for increasing scan speeds, thus decreasing their circularity. For each designed diameter, the laser parameters need to be re-optimised to produce pillars of low feature size while preserving the pillar roundness. Figure A.2a depicts the distortion in shape of pillars at high speeds. At such high speeds, the pillars begin to start merging and at one point become joined. This is shown in figure A.2b.

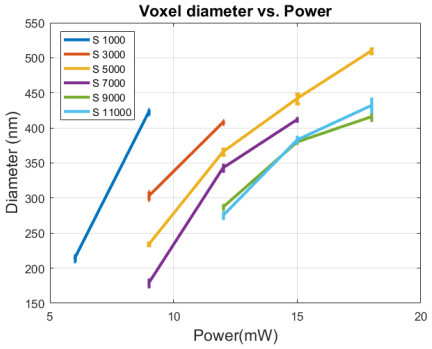

(a) *Mean pillar diameter variation with laser power at different scan speeds, S(µm/s) in Galvo mode*

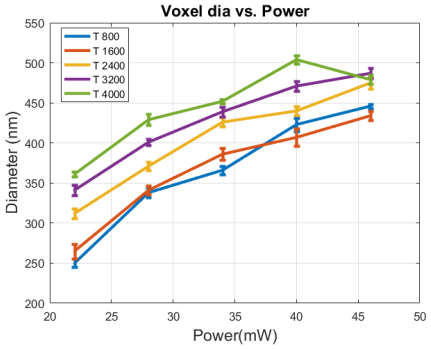

(b) *Mean pillar diameter variation with laser power at different exposure times, T(µs), in Piezo mode*

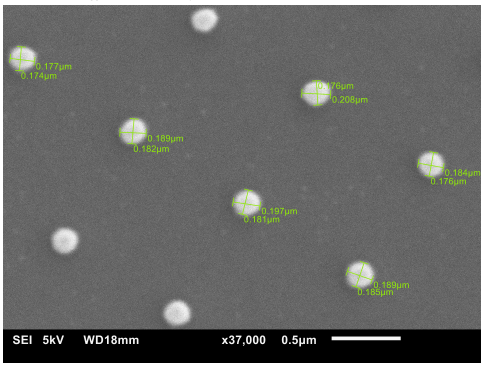

(c) *Pillars of diameter less than 200 nm depicted using Laser power 18 mW and scan speed 7000 µm/s in galvo mode, T(µs)*

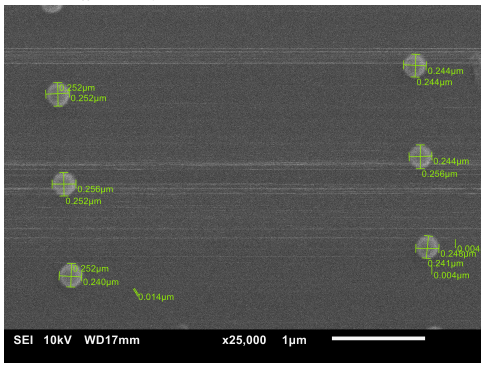

(d) *Pillars of diameter about 250 nm produced using Laser power 44 mW and time of exposure (T) 800 µs in piezo mode*

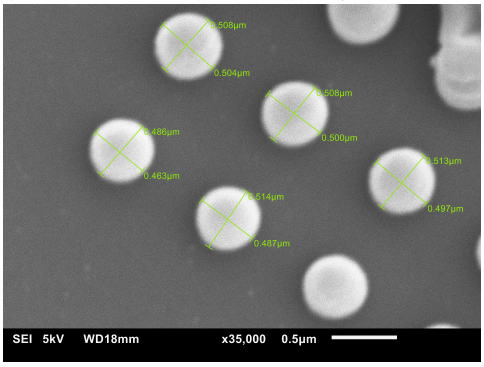

(e) *Pillars of diameter more than 500 nm depicted using Laser power 36 mW and scan speed 5000 µm/s in galvo mode, T(µs)*

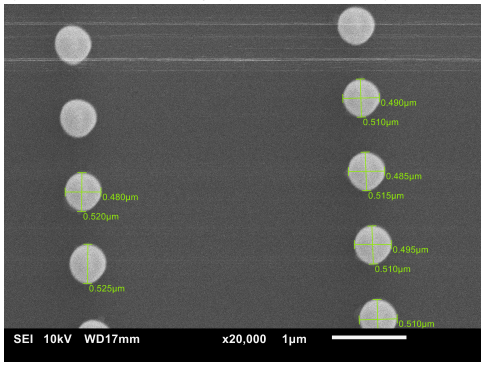

(f) *Pillars of diameter about 500 nm produced using Laser power 92 mW and time of exposure (T) 3200 µs in piezo mode*

Figure A.1: *Varying pillar diameters as a function of laser power in the conventional mode (IP-L 780) for galvo and piezo writing*

A.2.2. Piezo writing mode

In this mode, the piezoelectric element moves from one point to the other before it being irradiated for a certain time by the laser. This time is called the time of exposure. Figure A.1b depicts the monotonic increase of pillar mean diameter with laser power and time of exposure (T). The pillars produced in the piezo scan mode were rounder than the galvo counterpart. However, this is done by providing a sufficiently high settling

time to the piezo element. Figures A.1c and A.1d compares pillars reaching the lower size limit in galvo and piezo modes while Figures A.1e and A.1f depict the same comparison for larger sized pillars.

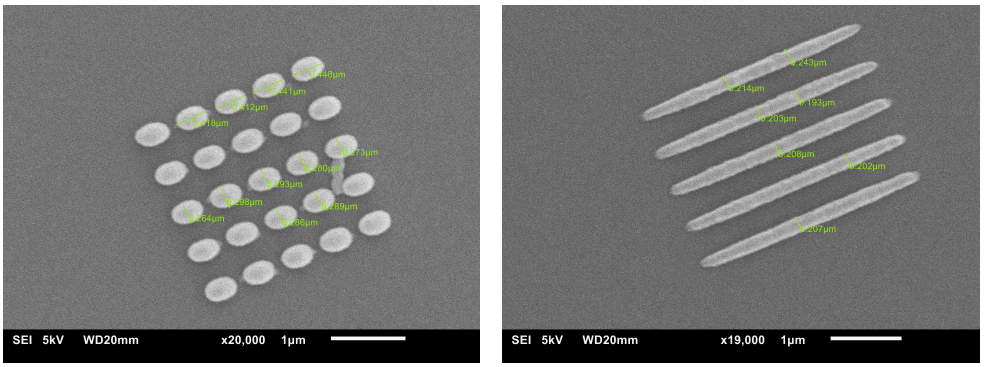

(a) *Elliptical shape of pillars at a high scan speed (10000 µm/s, Laper power 45 mW)*

(b) *Merging of pillars into a straight line at higher scan speeds (190000µm/s, Laser power 45 mW)*

Figure A.2: *Distortion of pillars with increasing scan speed in Galvo mode during conventional wiriting*

The trends shown in Figures A.1a and A.1b are rather qualitative than quantitative since repeating the experiments produces large variations in diameters. Printing on larger areas produced regions where no pillars were printed or pillars that were greatly reduced in diameters than other regions of the pattern (in both galvo and piezo modes). Figure A.3 depicts this for the galvo mode in an optical micrograp(figure A.3a) and a zoomed in SEM micrograph(A.3b). The same is depicted for the piezo mode in a conventional configuration in Figures A.3c, A.3d. It is worthy to note that the auto tilt correction option is turned on in this case. The non-uniform results obtained in both cases led to examining whether the strength of the interface has a role to play in finding the boundary between the resin and the substrate.

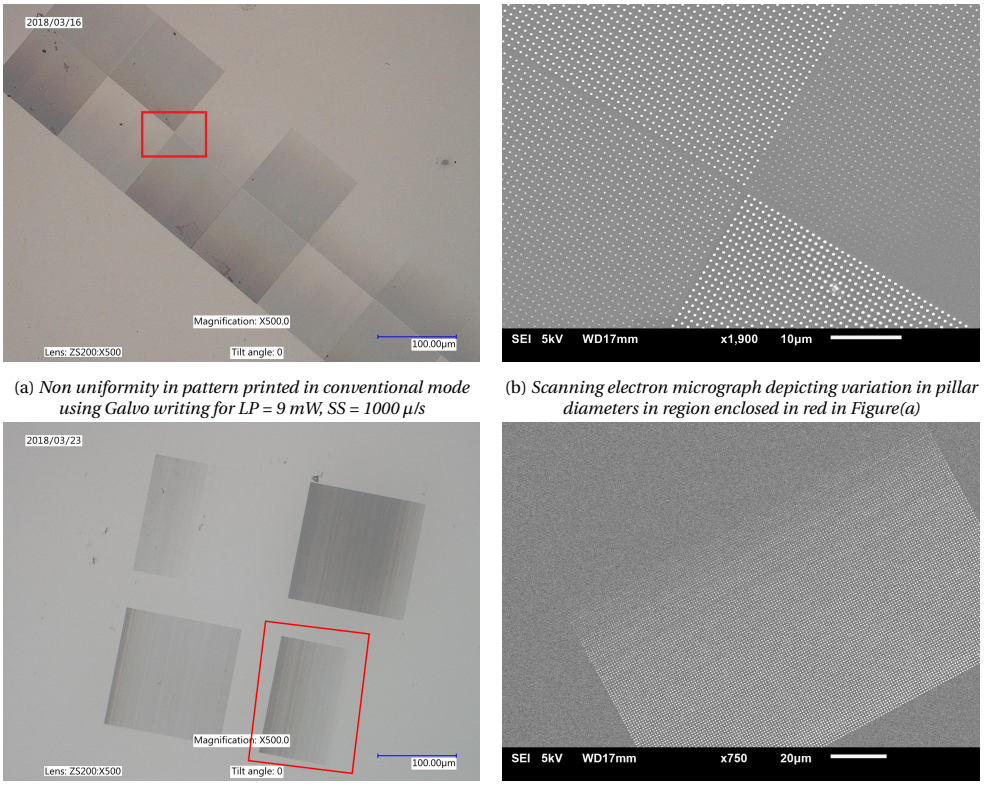

(a) *Non uniformity in pattern printed in conventional mode using Galvo writing for LP = 9 mW, SS = 1000 µ/s*

(b) *Scanning electron micrograph depicting variation in pillar diameters in region enclosed in red in Figure(a)*

(c) *Non uniformity in pattern printed in conventional mode using Piezo writing for Laser power = 32 mW, T = 2000 µs*

(d) *Scanning electron micrograph depicting variation in pillar diameters in region enclosed in red in Figure(c)*

Figure A.3: *Variation in pillar diameters over larger areas in galvo writing mode and conventional configuration*

A.3. DiLL mode

Printing using Galvo mode in DiLL configuration produced unsatisfactory results for fabricating topographies on a large scale. The galvo mode does not allow compensating for the tilt of the substrate. This is one major reason why it can't be used to produce uniform topographies over larger areas (above a few hundred micron length scales). It can be a viable option for smaller areas. On using the **piezo writing mode in the DiLL configuration**, the pattern uniformity increased. This was done using a laser power of 24 mW and a time of exposure (T) of 2000 μs. The auto tilt correction feature in the machine was turned on during this process. The parametric sweep of Piezo mode in this case has been already discussed in Supplementary information section 3.3. For the Galvo writing mode, the parametric sweep was not carried out.

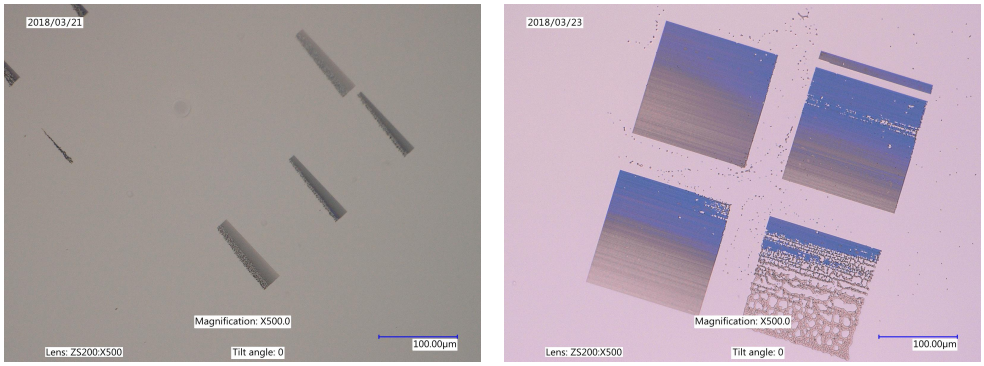

(a) *Printing in DiLL configuration with Galvo writing using a laser power of 9 mW and scan speed of 1000 µm/s*

(b) *Printing in DiLL configuration with piezo writing using a laser power of 24 mW and a time of exposure of 2000 µs.*

Figure A.4: *Printing in DiLL mode using galvo and piezo modes*

A.4. New methods of enhancing interface amplitude

Coating Poly-vinyl alcohol

A layer of Polyvinyl alcohol (PVA) was coated onto the fused silica and borosilicate substrates to enhance the interface strength of the substrate. PVA was dissolved in water and spin coated for 2 minutes at 1000 rpm on substrates that were prior treated using air plasma. The signal amplitude was increased to about 3000 in this case. However, the PVA was not coated uniformly over the substrate. It was found that the upon developing the sample, all the pillars debonded and fell down (sticking to the substrate). This is possible due to dissolution of PVA during the developing process. Figure A.5a shows the optical image of pattern obtained on PVA coated fused silica substrate (DiLL configuration) in the piezo wiriting mode. Figure A.5b shows the SEM micrograph of the same pattern thus depicting that an optically uniform looking pattern (A.5a) was composed of fallen pillars.

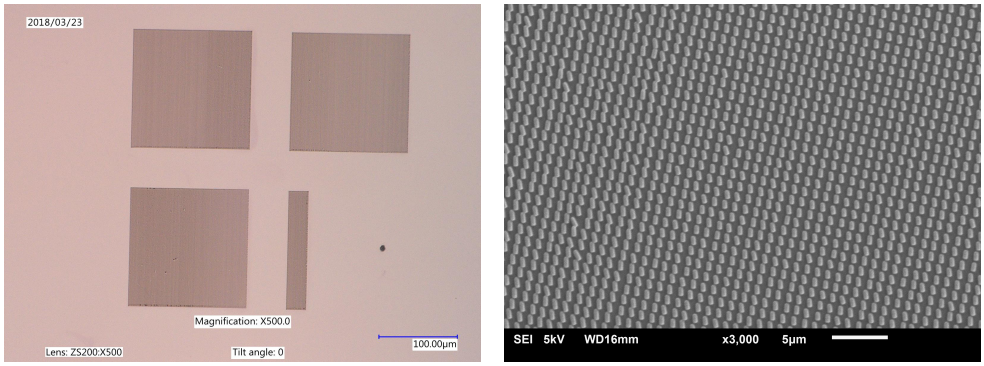

(a) *Optical image of printing on PVA in DiLL mode (piezo writing)*

(b) *SEM image of the fallen pillars*

Figure A.5: *Printing on a layer of PVA using piezo writing method in DiLL configuration*

Sputtering Gold-Palladium

A few nm thick gold-palladium coating was sputtered onto the fused silica substrate for 2 minutes at a sputtering current of 10 mA and a pressure of 9×10^{-2} $m$bar. Upon printing on this substrate, the polymer burns off even at very low powers. Bubbles appear while printing and upon developing the sample, porous and burnt regions within the pattern are produced. The structure resembles a micro/nano porous scaffold in morphology. However, the structure is uncontrolled and hence not relevant for this study. Figure A.6 depicts these structures.

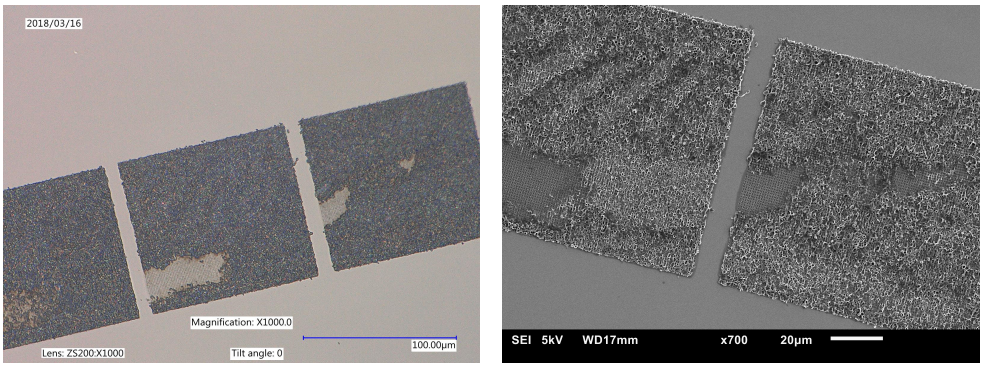

(a) *Optical image of printing over a sputtered layer of Au-Pd* (b) *SEM image of the burnt structures*

Figure A.6: *Printing on substrate sputtered with a layer of Gold-Palladium mixture*

Other coatings and resin-substrate combinations

Coatings of PEDOT:PSS as well as food colourant dyes were also coated onto the substrates after briefly treating with oxygen plasma however, it was difficult to find interfaces in these cases. The coatings produced were also non-uniform. These are therefore not recommended.

The borosilicate glass was used with IP-Dip but no interface could be detected in this case. The same was found for IP-L in combination with fused silica substrate. This can be attributed to the small difference in the refractive indices of these materials (refer table 3.1 in supplementary information).

A.5. Effect of temperature and humidity

The 2PP setup is operated at 18-21°C. However, when the temperature was raised by about 10°C, there was a noticeable shift in the print quality. This is shown in Figure below. It can be seen that the pillar sizes have changed and the pattern loses uniformity to some extent at a higher temperature. The increase in humidity may also have affected this.

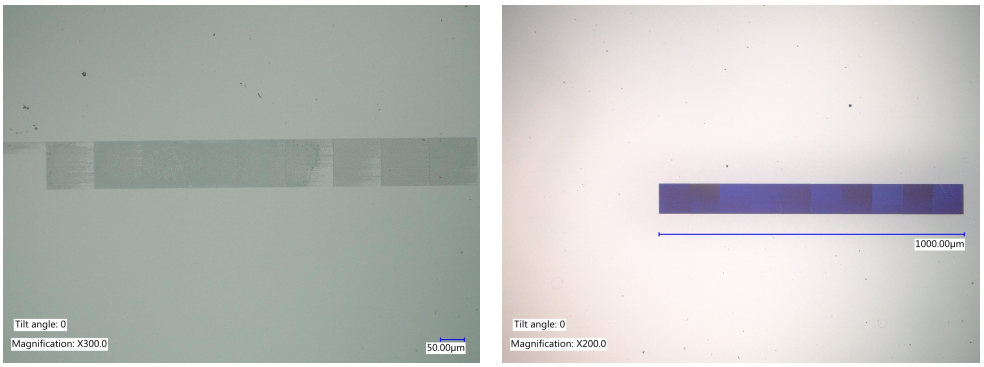

(a) *Printing at 30° C* (b) *Printing at 20° C*

Figure A.7: *Effect of temperature and humidity on patterning (DiLL mode, Galvo writing, LP = 9 mW and scan speed = 1000 µm/s)*

A.6. Varying pillar interspacing

The pillars were printed using different laser parameters as well as varying interface distances for various interspacings (center to center). Table A.1 gives an overview of the patterns obtained and the parameters used in their printing. Each images contains three patterns printed at different interface distances. The interface distances are 0.3 μm, 0.4 μm, and 0.5 μm for the bottom, middle and top patterns respectively in each image.

It can be seen that the pillars become larger with decreasing interface distances. Also, with decreasing pillar interspacing, the pillars tend to lose their round shape and become joined to each other with polymerisation occurring in spaces between them. This critical interspacing distance seems to increase with increasing laser dose as well as with decreasing interface distance.

Pattern	**Printing parameters**	**Interspacing**
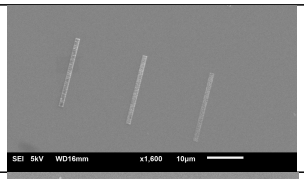	Laser power = 14.4 mW, t = 1600 μs	300 nm
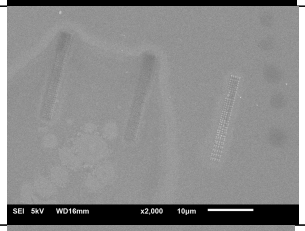	Laser power = 14.4 mW, t = 1600 μs	500 nm
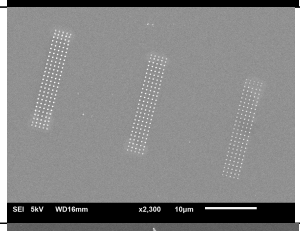	Laser power = 14.4 mW, t = 1600 μs	800 nm
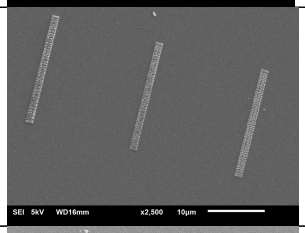	Laser power = 14.4 mW, t = 2400 μs	300 nm
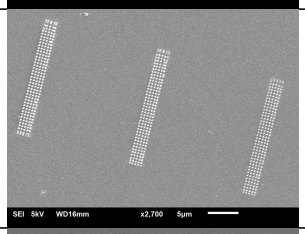	Laser power = 14.4 mW, t = 2400 μs	500 nm
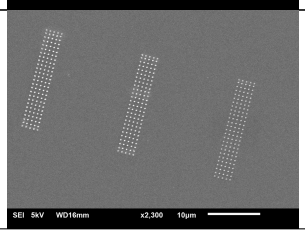	Laser power = 14.4 mW, t = 2400 μs	800 nm

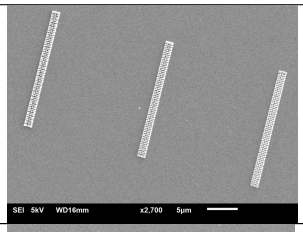	Laser power = 20.8 mW, t = 800 μs	300 nm
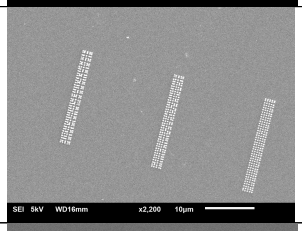	Laser power = 20.8 mW, t = 800 μs	500 nm
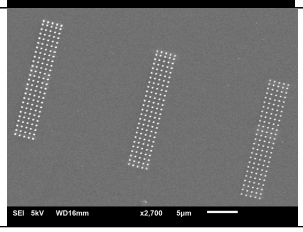	Laser power = 20.8 mW, t = 800 μs	800 nm

Table A.1: *Patterns obtained at varying interspacings, interface distances, and laser parameters*

A.7. Measuring uniformity of patterned areas (and Image analysis)

For the cutoff intensity of 130, covering pillars above 284 nm, a uniformity of 73% was found in figure 2.4. The methodology has already been discussed in Chapter 2 (Paper). This sections shows a few more examples of this applied to other patterns fabricated with the same laser parameters.

Pattern	Sample description	Percentage
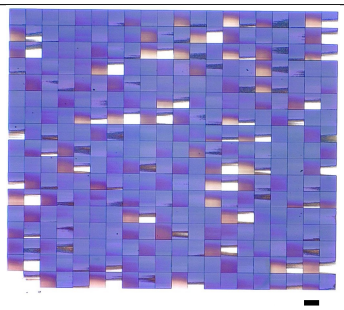	DiLL mode,IP-Dip + ITO glass, Tilt corrected	86%
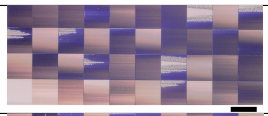	DiLL mode, IP-Dip + Fused silica, Tilt not corrected	55%
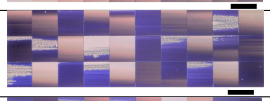	DiLL mode, IP-Dip + Fused silica, Tilt corrected	64%
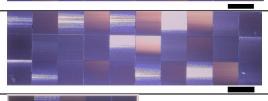	DiLL mode,IP-Dip + ITO glass, Tilt corrected	75%
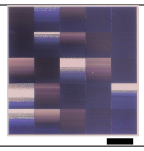	DiLL mode,IP-Dip + ITO glass, Tilt corrected	84%

Table A.2: *Measuring pattern uniformities. The scale bar for each figure is 100 µm*

A.7.1. Image analysis in MATLAB

The SEM images are analysed using Image-J. This is used to obtain the pillar dimensions over large areas by scaling it appropriately using a high resolution image. FigureA.8a shows a low resolution. This was converted to a thresholded image as in figure A.8b to calculate the pillar height, diameter and the number of pillars in this region. The same procedure is applied to a high resolution image and the pillar dimensions from known pillars are used to scale the dimensions obtained from the low resolution image. This method is not fool proof but can give approximately good results and reduce measurement times when measuring pillar dimensions for large number of pillars.

Once the mean pillar dimension and standard deviations are known from this method, a correlation is made to optical image as shown to obtain the cutoff pixel intensity indicating pillars that have diameter than a certain minimum value. This is done using a simple MATLAB code that follows the given process flow:

1. Load image file (preferably in .png format) into MATLAB. Make sure that all the images are taken under same imaging conditions (brightness, contrast, colour, shadow, magnification, beam type etc.)

2. The rgb image needs to converted to a grayscale image since we want to track intensity of pixel rather than a colour. This is done using the rgb2gray command.

3. The pixel intensities are entered into a m*n matrix where m and n are number of pixels along length and width. Let this matrix be called J

4. We want to calculate the threshold intensity (maximum value, say λ) which is permissible. Higher intensity values correspond to whiter pixels which indicate smaller pillar dimensions.

   we want a relation depicting percentage area within bounds as:

$$f(\%) = \frac{A1}{A2} * 100 \tag{A.1}$$

   where f is the percentage feasible area, A1 = area with intensity below threshold area in total image, A2 = total area considered which includes non printed areas too.

   To find A1, we want pixels with intensity I such that,

$$A1 = size(J <= \lambda) \tag{A.2}$$

   Also to find A2,

$$A2 = size(J) \tag{A.3}$$

5. Using trial and error we can find λ intensity that yeild the same feasible area as that from SEM measurements. This intensity λ can now be applied to other samples fabricated using same laser parameters to characterise them without SEM imaging.

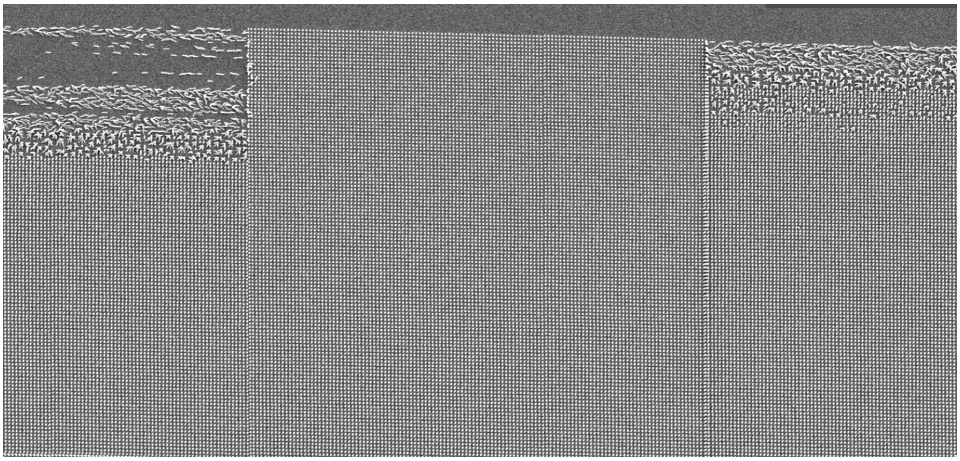

(a) *SEM image of pillars taken at low resolution*

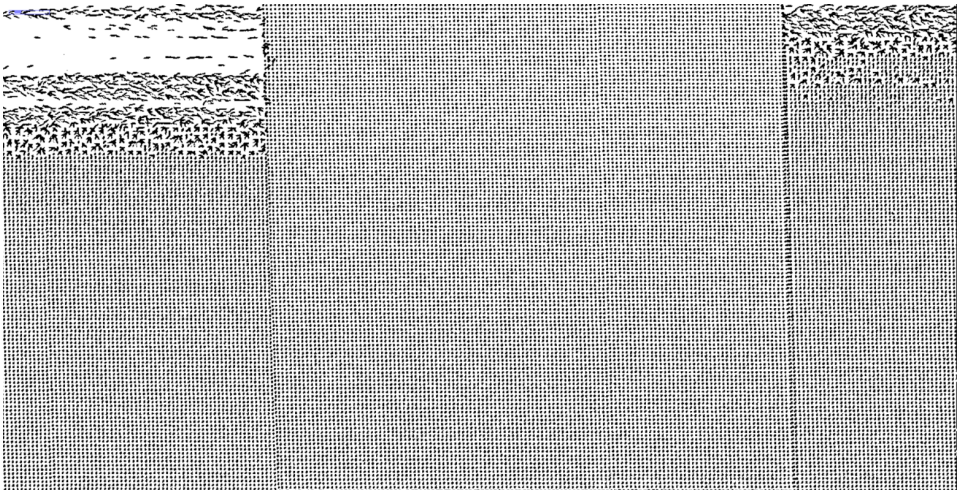

(b) *Applying threshold to low resolution image for measuring pillar dimensions*

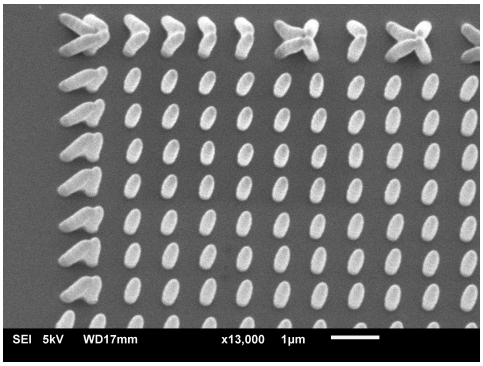

(c) *High resolution SEM imaging of pillars*

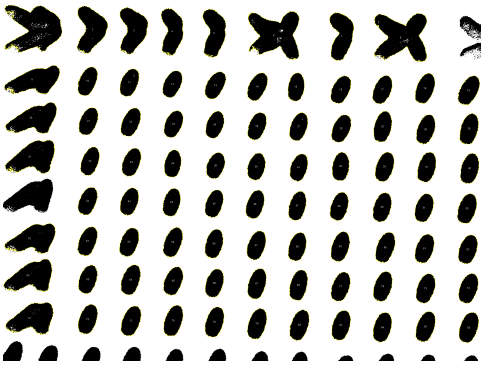

(d) *Thresholding image (c) to obtain pillar dimensions from high resolution image*

Figure A.8: *Obtaining pillar dimensions via scaling from a high resolution image*

A.8. Effect writing direction on pattern uniformity

The writing directions were also varied while writing the patterns. Figure A.9 depicts the change in uniformity of the pattern in a direction perpendicular to the writing direction. For instance the case (a) shows diminishing intensity in vertical direction while it is written horizontally. The same can be seen for vertical, diagonal, and box writing strategies. The cause for this is still not well understood.

Pattern label	Writing direction
a	Horizontal
b	Verical
c	Diagonal
d	Rectangular

Table A.3: *Effect of writing direction on patterns shown in Figure A.9*

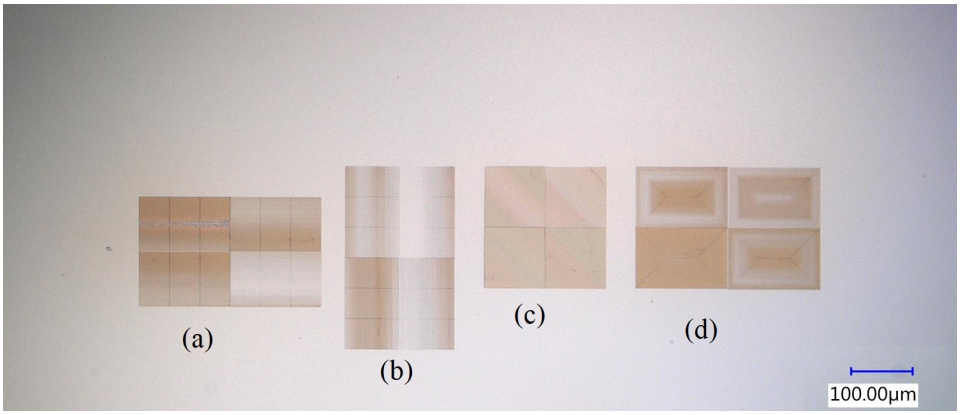

Figure A.9: *Printing in DiLL mode using different writing directions*

A.9. Effect of tilt correction method: Linear and Parabolic

A parabolic tilt compensation was also tried instead of a linear one. This was done using the auto tilt correction feature within the machine. The feature does not allow for tilt correction multiple times during the writing process. For example, on selecting the parabolic fit, the first tilt correction is parabolically compensated however the second time it changes back to a linear fit. Figure A.10 shows the non linear (curved) unprinted area upon enabling a parabolic tilt compensation (figure A.10b) in comparison to its linear counterpart (figure A.10a). The structures are written at laser power 14.4 mW, exposure times 2400-2800 μs, and interfaces of 0.4-0.5 μm.

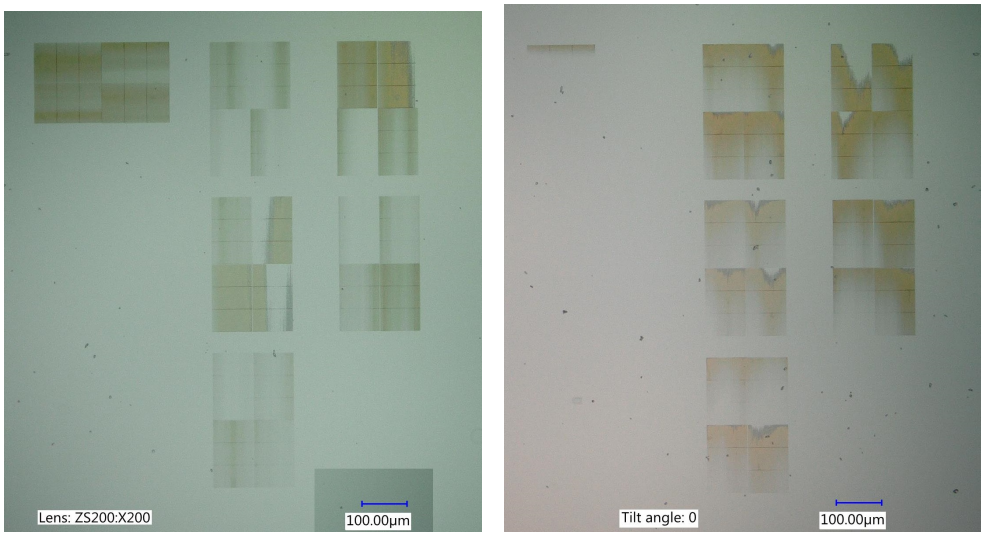

(a) *Linear tilt compensation* (b) *Parabolic tilt compensation*

Figure A.10: *Linear versus parabolic tilt compensation*

A.10. Effect of update rate

The update rate (U, in Hz) in the piezo writing mode controls the rate of interpolation between consecutive points. The writing speed (S) in piezo mode is given by:

$$S = U * D \tag{A.4}$$

where D is the distance between two consecutive points in nm. This parameter was seen to affect the size and position of the pillars within the topography. It was previously said that the factor does not affect writing in pulsed mode setting of the piezo mode [82] but it is seen otherwise that this factor can considerably affect the writing quality. The laser power and exposure times were set at 14.4 mW and 2400 μs respectively. Figure A.11 depicts this change pattern quality printed on top of a scaffold.

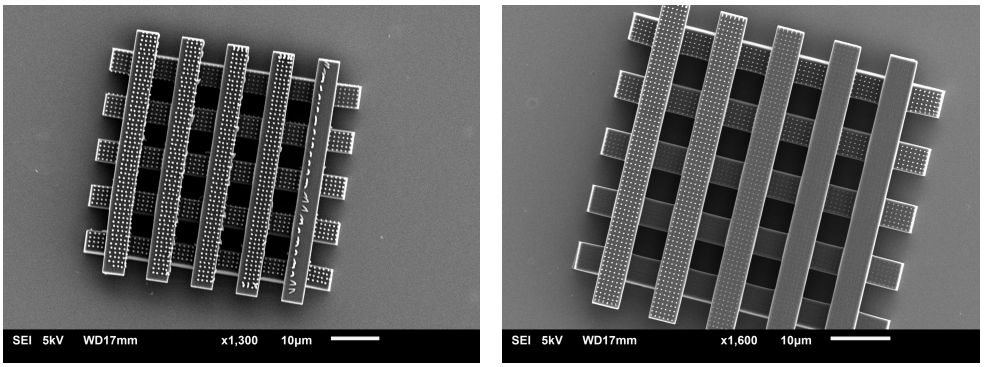

(a) *Printing using an update rate of* 10^3 *Hz* (b) *Printing using an update rate of* 10^4 *Hz*

Figure A.11: *Effect of update rate on patterning in piezo mode (pulsed setting)*

A.11. Large scale patterning on sheets

The patterns were upscaled to be incorporated on top of galvo printed plain sheets. The following two major problems were encountered during this process:

1. Warping in case of large sheets
2. Non uniformity while printing topographies on sheets

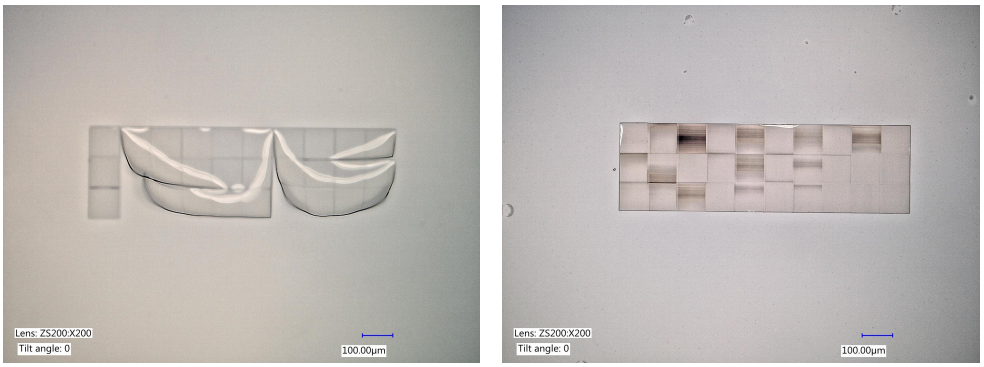

(a) *Printing using an update rate of* 10^3 *Hz* (b) *Printing using an update rate of* 10^4 *Hz*

Figure A.12: *Effect of update rate on patterning in piezo mode (pulsed setting)*

The warping of sheets (l = 1mm, b = 300 μm, t = 5 μm) as shown in Figure A.12a is caused due to shrinkage of sheets after they cool down and lose contact with the base, causing them to curl up. This is countered by increasing the interface distance (to 2 μm) so that these sheets are adequately attached to the base (printing 3 μm above the interface). Also, the blocks (100 μm * 100 μm each) that are stitched together to form this sheet are made to overlap 5 μm each other. This design change effectively countered the warping phenomenon.

Figure A.12b illustrates the variation in pattern uniformity along the sheet with large parts that remain unprinted. The patterns were printed without any tilt correction. It needs to explored whether a tilt corrected is still needed in this case. A very interesting phenomenon that is seen while printing patterns on these sheets is that these patterns appeared only on sheets that are printed towards positive x and positive y directions. This is attributed to the fact that the ITO coated fused silica substrate used in this case is tilted by about +0.04° to +0.06° in both x and y directions. Considering a 2D scenario in the XZ plane, Figure A.13 depicts the two situations of printing in $+x$ and $-x$ directions. The positive x in DiLL mode lies from right to left while the $+z$ lies from top to bottom direction. In case of A.13a, while printing sheets from right to left, the positive tilt angle ϕ_x causes the blocks (in blue) causes the sheets to be attached to the substrate (in green). In case A.13b, while printing from left to right, the sheets are not fully in contact with the substrate. This leads to insufficient attachments that can cause misalignment of the surface. In case A.13a, the patterns have a flat surface to attach to while in case A.13b, the non-flat surface prevents so in A.13b. This is one possible explanation for why the topographies are printed only in case A.13a. Figure A.14 shows all the possible printing directions of writing for these sheets(- -, + +, + -, - +) with the print occurring only in the + + case. The label descriptions can be found in table A.4.

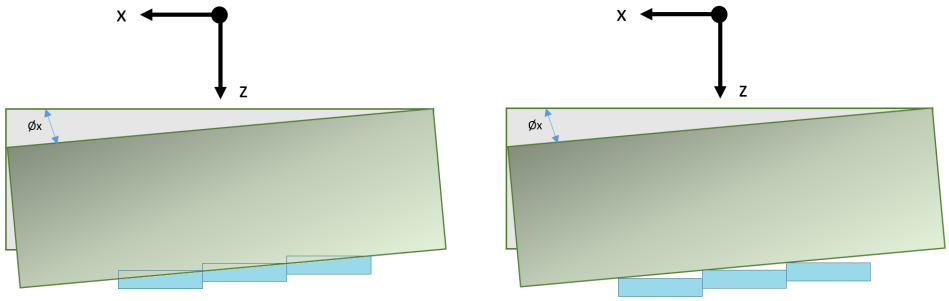

(a) *Printing sheet (in blue) on tilted substrate towards +x direction (starting from right)*

(b) *Printing sheet (in blue) on tilted substrate towards -x direction (starting from left)*

Figure A.13: *Effect of update rate on patterning in piezo mode (pulsed setting)*

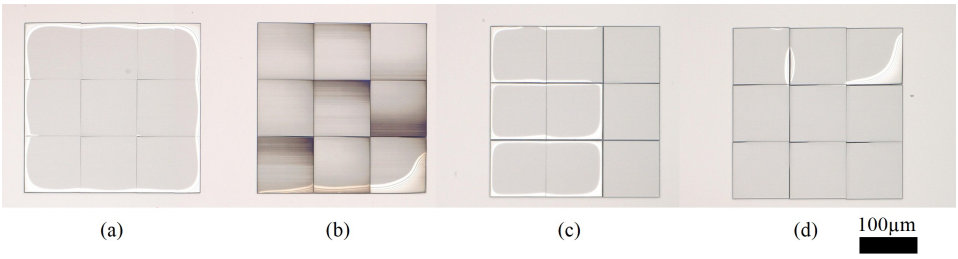

Figure A.14: *Writing patterns on sheets written in different directions*

Pattern label	Direction-x	Direction-y
a	-	-
b	+	+
c	+	-
d	-	+

Table A.4: *Writing directions for sheets written in Figure A.14*

A.12. Large scale patterning on scaffolds

A similar warping phenomenon (see figure A.15a) is seen when scaffolds are printed on a larger scale. This is countered in a similar way as in section A.11. The scaffolds are made to overlap 5 μm with each other to solve

this problem as well as by increasing the interface distance. Figures A.15b and A.15c depict the pattern non-uniformity. Enhancing the pattern uniformity involves further study and should involve investigate the effect of tilt correction on patterns and the z-offset given to the patterns to attach to the sheet or scaffold surface.

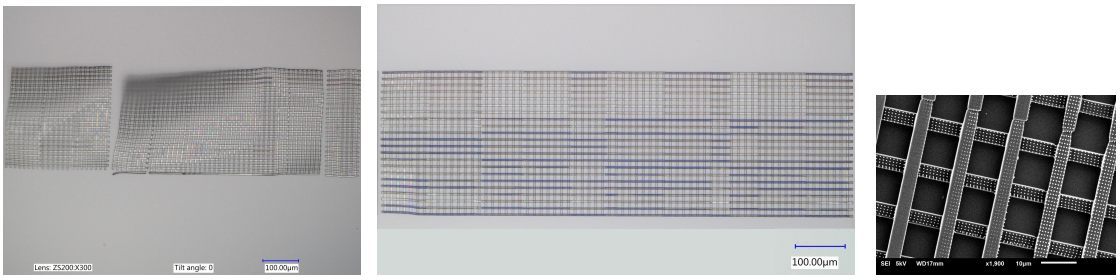

(a) *Warping of a large area scaffold*

(b) *Uneven pattern over the scaffold structure*

(c) *SEM micrograph depicting uneven pattern printing*

Figure A.15: *Upscaling patterns on a scaffold*

A.13. Viewing patterns under an inclined beam

The optical images in this study have been taken under a beam directly perpendicular (approximately) to the substrate. However, on imaging these samples using beam that are inclined to the substrate (using peripheral lighting), different colours are produced. This section depicts examples for some of such patterns, the parameters used, and the configuration that was used to produce them.

A.14. Trying to mimick a controlled disorder pattern

The controlled disordered arrangement of nanopatterns inspired by Dalby et al.[36] was programmed to printed using the 2PP process. The random points were programmed using MATLAB over a 100 μm × 100 μm surface an repeated over larger areas. The user manual advises users not to use the 'Connectpointsoff' command however, printing this random arrangement in piezo mode could not be realised without using this command. Care was taken with respect to not exciting the piezo element close to its resonance frequency. Upon printing, the pillar interspacings were found to be much larger than programmed. Also, the pillars were much larger than expected for known laser power and exposure time calibration. This is shown in Figure A.16. This problem can be solved by printing in Galvo mode but this would involve a compromise with the pattern uniformity when printing on larger areas. Within piezo mode, increasing the update rate or tweaking the piezo settling and deceleration times may help further optimise the process.

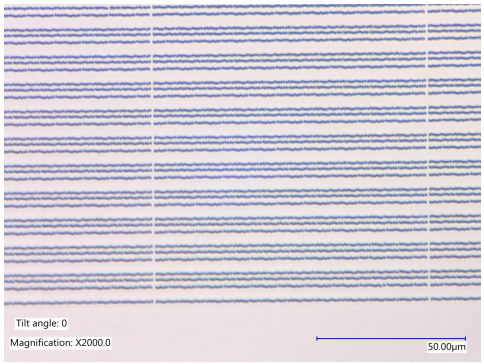

Figure A.16: *Results obtained on trying controlled disorder pattern printing*

Pattern	Printing details
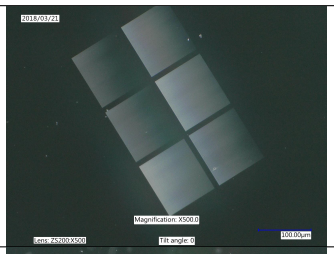	Conventional mode, Galvo writing, 90 mW, 1000 μ/s, IF = 0.1 μm
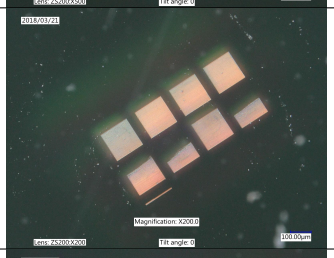	Conventional mode, Piezo writing, PVA coating, fallen pillars, 32 mW, 2000 μs, IF = 0.0 μm
	DiLL mode, Piezo writing, 32 mW, 2000 μs, IF = 0.1 μm
	DiLL mode, Piezo writing, ITO coated glass, 27.2 mW, 2500 μs, IF = 0.1 μm
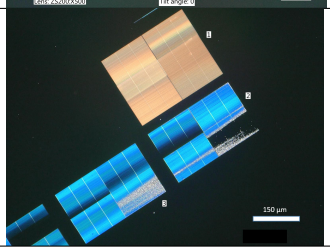	DiLL mode, Piezo writing, ITO coated glass, 27.2 mW (upper block) and 14.4 mW (lower blocks), 2500 μs (upper block) and 2400 μs (lower blocks), IF = 0.1 μm

Table A.5: *Patterns observed under peripheral lighting condition of the microscope (IF = Interface distance)*

B

Microfluidic device

This section deals with preparation of the microfluidic device. The section on clamp design (Section B.2) applies only for delamination testing substrate since the fused silica substrates (used in Biological studies) were bonded using air plasma.

B.1. Mould design

Figure B.1 depicts the mould design and dimensions used for mould used for curing PDMS. A small uplifted area at the inlet and outlet was made to make sure that the tubing does no touch all the way to the bottom of the PDMS, which may lead to build up of high pressures. The diameter of inlet and outlet is 3 mm for the delamination testing while it is 1.6 mm for the preliminary biological testing samples. This was due to the different diameters of tubings used for these cases.

B.2. Clamp design

The ITO was not able to bond properly to PDMS using oxygen/air plasma bonding. Methods such as use of epoxy glue, quick fix (second) glue were used but these yielded unreliable bonding too. The glues swell up over a period of time when in contact with fluids in the channel. Uncured PDMS as a glue was also tried in an effort to seal the edges of the chip but this was met with unsatisfactory results and frequent leakages. For some devices that acheived high bonding strength, it was difficult to debond PDMS for subsequent SEM imaging. This also posed a major problem.

With inspiration from my colleague Richard Pleeging who used a clamp to seal his microfluidic device, it was decided to design a clamp for the current study and circumvent the above problems. The clamp was 3D printed using Poly lactic acid (PLA). The clamp was designed to tolerate large shearing and compressive forces while minimising bending. It was also desired that the clamp applied a uniform force across the device. Space in the middle was left to allow optical examination and allow access for the tubings. The area surrounding this space was made protruded as shown in Figure B.2 to minimise bending and prevent liquids from escaping along the channel boundary. The clamp design can be seen in figure B.2 The clamp thus helped to:

- Conveniently remove PDMS for imaging using SEM
- Reach higher flow rates
- Control bonding strength by varying screw tension

For flow rates above 5-8 ml/min, the leakage occured from inlet and exit points. Fixing these tubes using PDMS glue was not very effective with PDMS tending to seep through the interface between tube and hole, ending up clogging the channel in some cases. Epoxy glue was found to be more effective in this case.

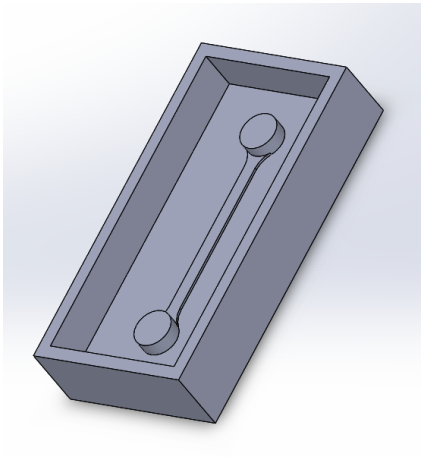

(a) *A 3D view of the mould for microfluidic chip*

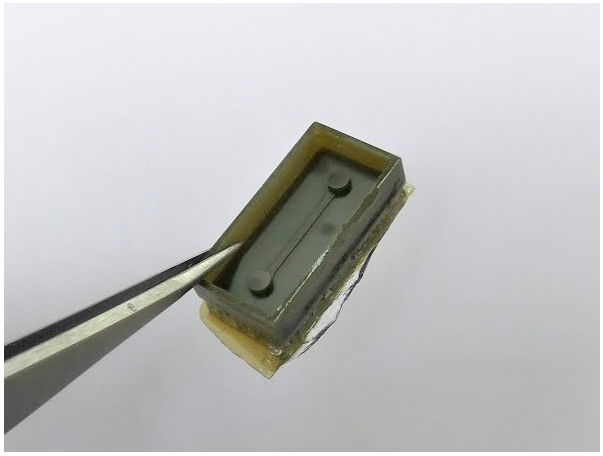

(b) *Top, side and front views of the mould with dimensions used*

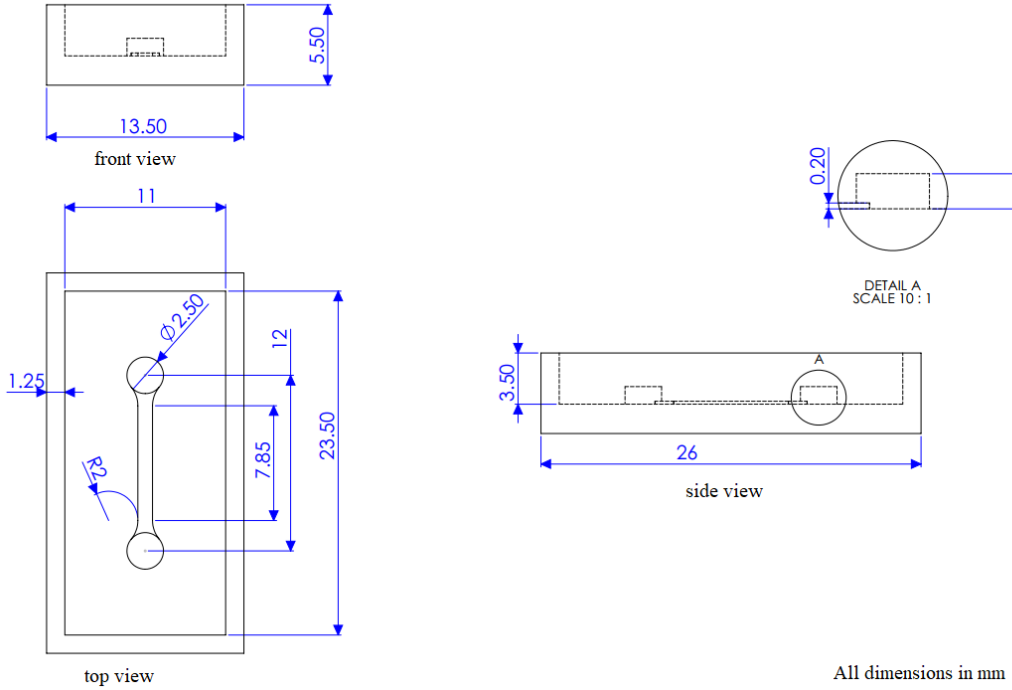

(c) *Top, side and front views of the mould with dimensions used*

Figure B.1: *Mould design used for the microfluidic study*

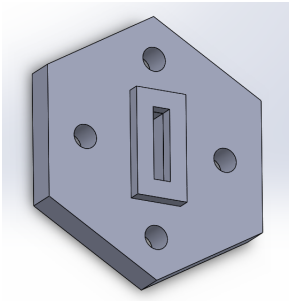

(a) *A 3D view of the clamp for microfluidic chip*

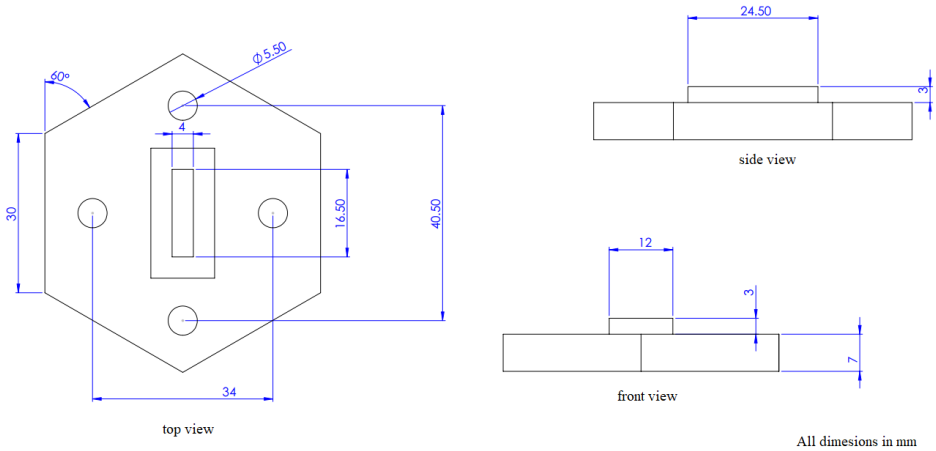

(b) *Top, side and front views of the clamp with dimensions used*

Figure B.2: *Clamp design used for the microfluidic delamination study of pillars*

B.3. Connections

Needles were connected to the tubings first. To do this, needles were removed from their base attachment using pliers. The back end of the was then inserted into the tubing while the front end pierced into the hole through PDMS. Glue from a hot gun was used to make the connections leak proof. The tubings were connected to the peristaltic pump. However, to use the pump, it first had to be calibrated by entering the tubing diameter followed by measuring the amount of fluid collected in a certain time. The flow rate was then calibrated accordingly.

B.4. PDMS preparation

1. **Cleaning moulds**
   After printing using stereolithography, the moulds were cleaned in ethanol using ultrasonication for 20 minutes. It is important that clean beakers be used during ultrasonication to prevent particles sticking to moulds.Moulds were then dried using air gun. Image B.1 shows the mould design used. The contamination was minimised by storing them in sealed petridish at all times.

2. **Stripping PDMS**
   PDMS was carefully stripped from the mould by first cutting with a blade along the edges of the mould. Care must te taken during this process since a wrongly cut PDMS will not bond using air plasma at a later stage. After cutting, the PDMS was carefully stripped using the blunt back end of a spatula. During the process, ethanol is injected into the spacings between the mould and the PDMS to facilitate easier stripping.

   The PDMS after stripping was turned upside down and cured again at 100° for 35 minutes to fully cure the previously unexposed side. Uncured PDMS can be cytotoxic and thus pose a major hindrance to

biological testing. Also, since ethanol was used during the stripping process, it is important to remove the ethanol absorbed into the PDMS using this method. Ethanol can otherwise swell the PDMS and interfere during the air plasma bonding.

3. **Air plasma**
   The side to be bonded (PDMS and glass) was kept in the air plasma chamber facing upwards. A power of 40 W was used for 2 minutes. Plasma was generated at a pressure of about 4 mBar. After removing the samples were immediately bonded. The 1 mm width of the topograhy was used to align the 1 mm wide channel around it. The alignment is more difficult for smaller topographical areas. Also, an error of abut 100 microns in alignment can easily happen while bonding. The non-bonded areas can be immediately identified from the air that gets trapped in that area. The PDMS has to be clean, flat, scratch free, and free from any other local defects for the bonding to be successful.

4. **PDMS removal after experiments**
   For some cases, the PDMS to ITO bond was pretty strong and it was difficult to separate the two layers by force. PDMS also turned brittle in the region close to the interface. Removal of PDMS by hand led to large chunks of it still sticking to the interface. A blade was used to cut open the PDMS but care must be taken while doing so, not to damage the pattern. PDMS being high elastic can compress and damage the pattern when high forces are applied to it. Also, it is almost unavoidable to avoid loss of the pattern towards the edges of the channel (along the width). Figure B.3 shows this effect. The region left undelaminated is enclosed in a red box. It is a wise idea to use a clamp to avoid pattern delamination by rubbing or moving PDMS parts. After removal, it is quite probable that micro particles or meso sized particles of PDMS still stick to the pattern causing damage or difficulty in removal.

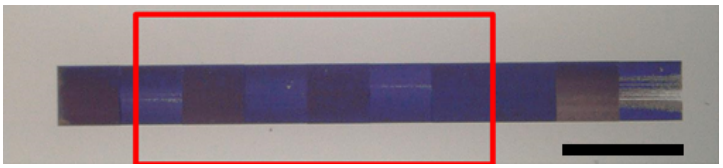

(a) *Pattern before removing PDMS*

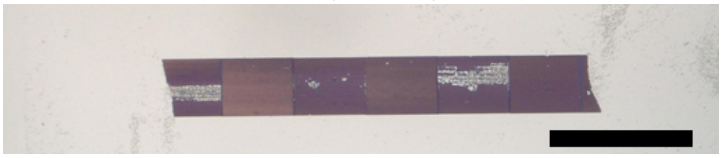

(b) *Damaged pattern after removing PDMS*

Figure B.3: *PDMS removal damaging the pattern. Scale bar is 200 μm*

The main factors influencing the quality of this PDMS layer were thus found to be:

1. The quality of optical membrane used in the stereolithograhy process:
   Scrathes and dust/microparticles will directly affect the mould.

2. The number of times the same mould is being used for PDMS curing:
   After 2-3 curing cycles, the mould can not be used.

3. Cleaning procedure for moulds being used second time or more:
   Cleaning with ethanol, isopropanol or acetone left small swollen particles of PDMS behind and were difficult to remove. Dry cleaning at high pressures using an air gun or electronic dust remover were found to be more useful. Using tweezers to remove leftover visible particles was also helpful.

4. Curing conditions:
   The mould need to be placed on flat surfaces while curing to prevent differential thickness along the PDMS layer. Also, the PDMS needs to be covered to prevent contamination using a glass petridish.

C

Preliminary Biological Studies

Six samples (NC, N-SH, N-T IC, I-SH, I-T) were used for the preliminary biological characterisation. The sample names and nomenclature are described in table C.1. Samples N and I have suffixes SH and T after them which denotes that on substrate N (fused silica glass glass) or I (ITO glass) two samples namely SH (a flat galvo written sheet), and T (topographical pattern) have been written. A schematic of the non-control samples (I,N) is also shown in figure C.2. The control sample used has nothing printed on it.

The specifications of the PDMS channel layer can be seen in Figure C.1 as side view (left) and front view (right). The channels are 7.85 mm long (14.5 mm lomg including inlet and outlet), 1 mm wide and 200 μm deep. Holes were punched into PDMS using biopsy punch of diameter 1.6 mm to create inlet and outlet. This creates holes that are a bit smaller in diameter than the punch due to PDMS retraction as a results of its elasticity. The substrates were bonded to PDMS channel layer using oxygen plasma bonding. Polytetrafluoroethylene (PTFE) tubing of inner diameter 0.3 mm and outer diameter 1.6 mm was inserted into the holes for supply and collection of culture media. The low bond strength between PDMS and ITO led to the leakage of I, IC chips after day 1. They were cleaned and cultured in a well plate after this. Samples N and NC were unaffected and were continued to be cultured as a microfluidic chip.

Sample name	Printing	Substrate
NC	Control	Fused silica glass
N-SH	Plain Sheet (Galvo written)	Fused silica glass
N-T	Topography (Piezo written)	Fused silica glass
IC	Control	ITO coated fused silica
I-SH	Plain Sheet (Galvo written)	ITO coated fused silica
I-T	Topography (Piezo written)	ITO coated fused silica

Table C.1: *Sample description for biological studies*

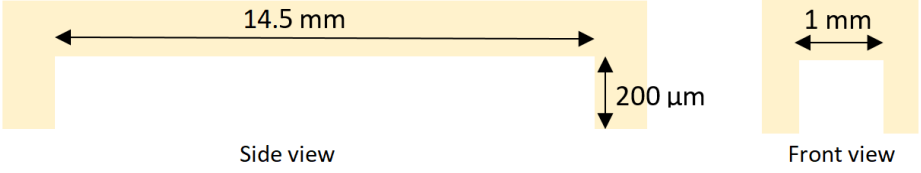

Figure C.1: *Schematic of the PDMS channel used*

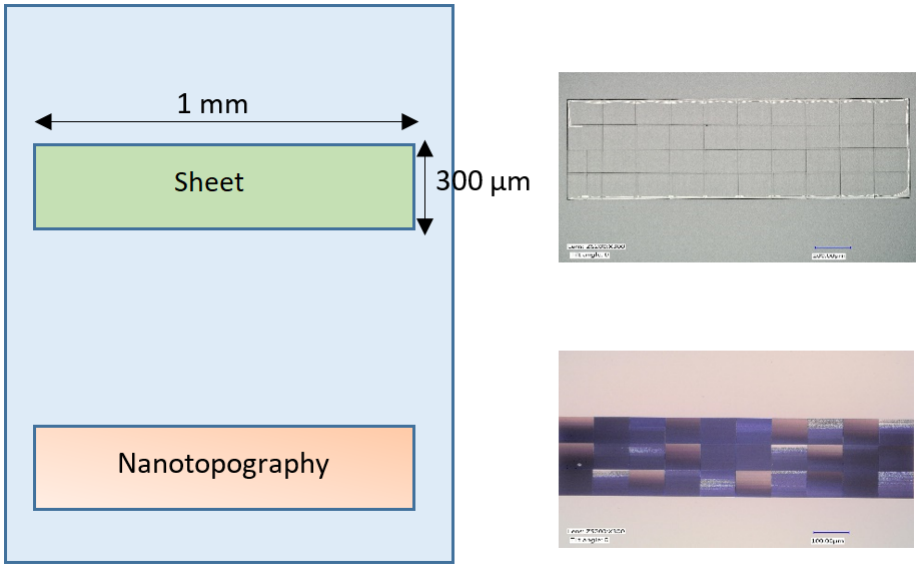

Figure C.2: *Schematic of the sample (I and N) used for preliminary study. Sample N only could be bonded using air plasma*

Scaffolds were also printed on some samples but these were delaminated when subjected to the fluid flow. One of such scaffold structures floating around in the microfluidic channel can be seen in Figure C.3. Interestingly, it behaves as meta material in the medium and reflects light in a certain wavelength band.

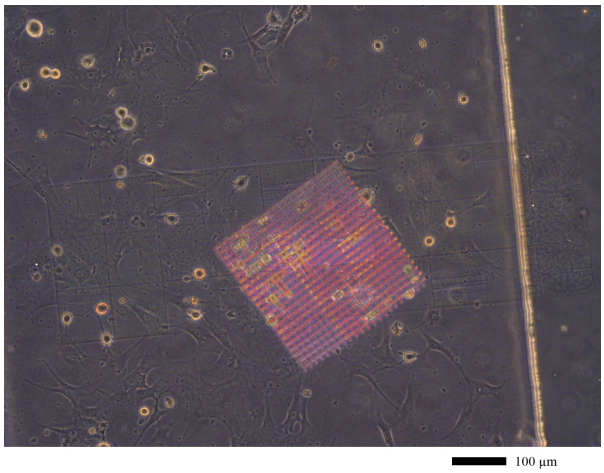

Figure C.3: *Delaminated scaffold reflecting a specific wavelength when submurged in the culture medium*

Optical imaging was done after 1, 4 and 5 days. At the end of 5th day, the cells were fixed by flushing them with glutaraldehyde-paraformaldehyde fixative for 10 minutes. This was followed by successively washing with ethanol in increasing concentrations of 50%, 70%, and 96% respectively. After this, they were taken for imaging using SEM. The PDMS layer was cut open for this purpose. The sheet printed on sample *I* and the nanopattern on the sample *N* were lost during the process. Therefore for these, only optical data can be used.

C.1. Optical Imaging

In this section, the images taken at various magnifications and time periods have been shown.

C.1.1. I: ITO coated fused silica

I-SH

The optical images in channel could be obtained only after day 1 due to leakage of device and loss of the sheet in the well plate. The images can be found in Table C.2

Images	Day	Comments
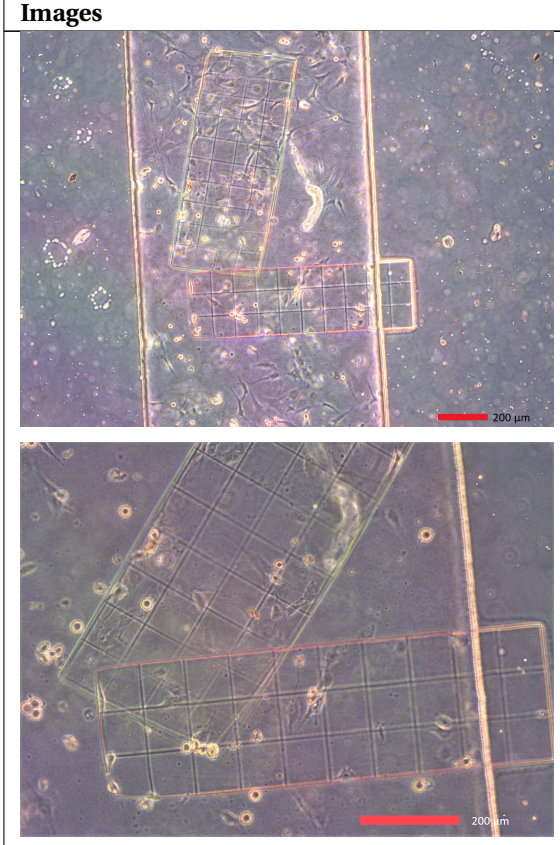	1	Floating structure at top. Few elongated cells on bottom sheet. Non-cytotoxic environment.

Table C.2: *Optical images of cells on galvo written flat sheets for ITO coated glass. Figures on the right depict the optical images of these features.*

I-T

The optical images in channel could be obtained only after day 1. After this, the images were made in a well plate setting. The image quality afterwards reduced, thus lacking a clear contrast between cells and substrate. There was also a loss in the cell number while changing the sample culture to a well plate type. This is shown in table C.3. In some cases, topographies have been enclosed in boxes and a few cells marked with arrows for better clarity.

Images	Day	Comments
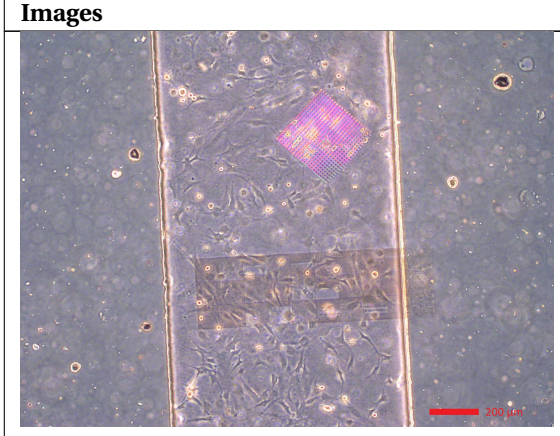 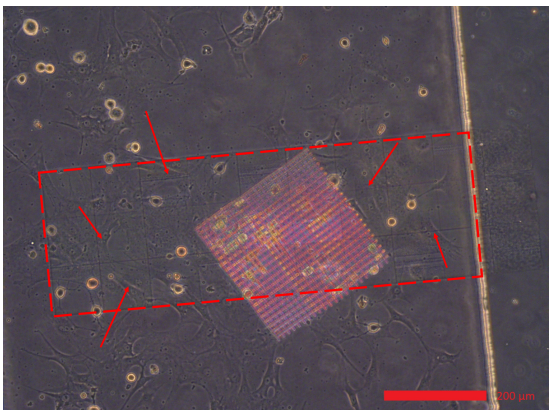	1	Floating scaffold structure in pink. Elongated cells on pattern with uniform spreading. Non-cytotoxic environment.
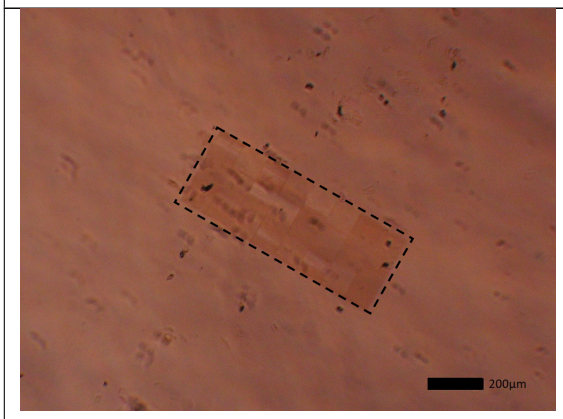 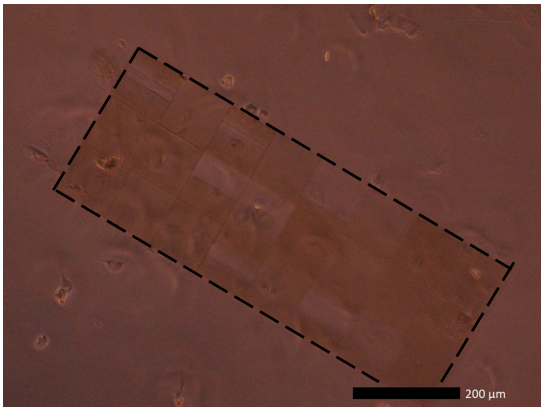	5	Few cells left due to change in culture conditions. It was difficult to focus cells in this case. It is difficult to assess the cell response in this case. Later, it will be shown via SEM imaging that the cells showed non-cytotoxic response on these patterns.

Table C.3: *Optical images of cells on topography for ITO coated glass*

IC

Control images within the channel could only be obtained for Day 1.

Images	Day	Comments
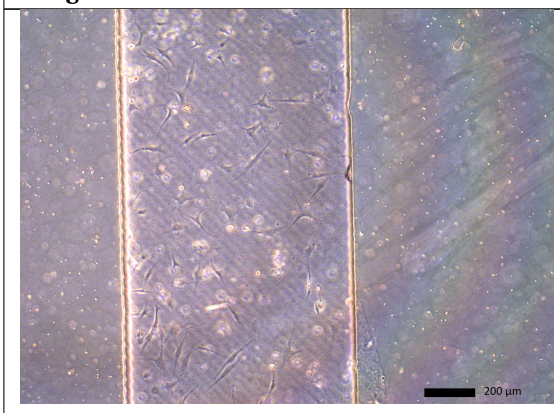	1	Cells show healthy and uniform attachment. No signs of cell death seen.

Table C.4: *Optical images of cells on control sample (without anything printed on it) for ITO coated glass*

C.1.2. N: Fused silica glass

N-SH

Images	Day	Comments
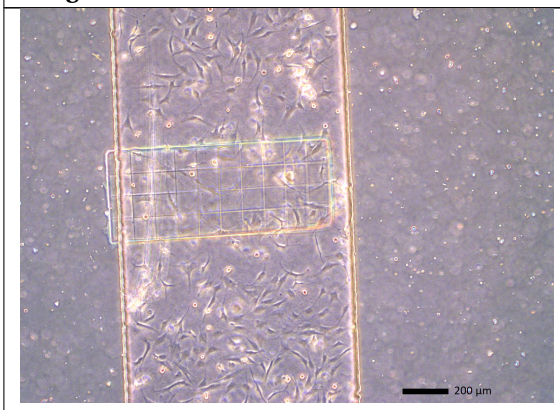 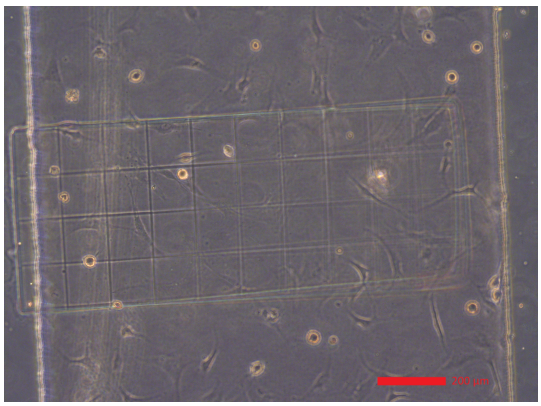	1	Elongated cells with no visible cytotoxic cells. It seems that cells spread less on the sheet than the surroundings. More experiments needed to confirm this.

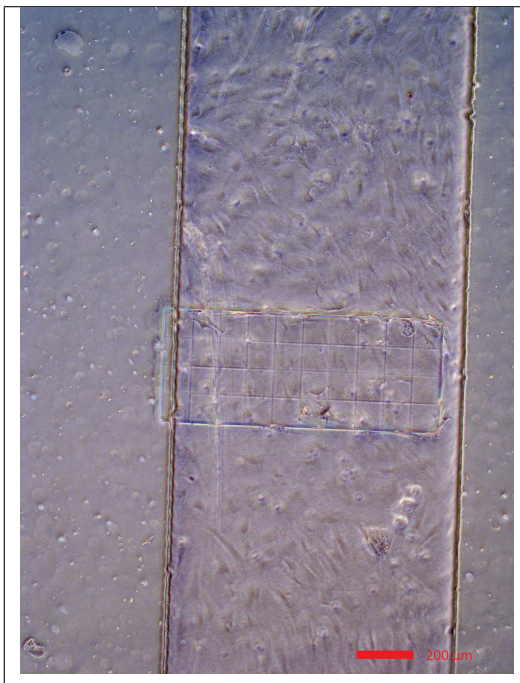 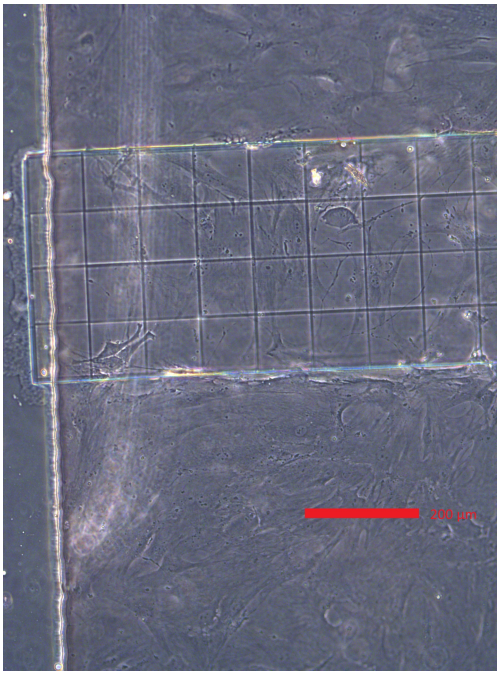	4	Even after day 4, no signs of cytotoxicity. Some cells can be seen on the sheet too.

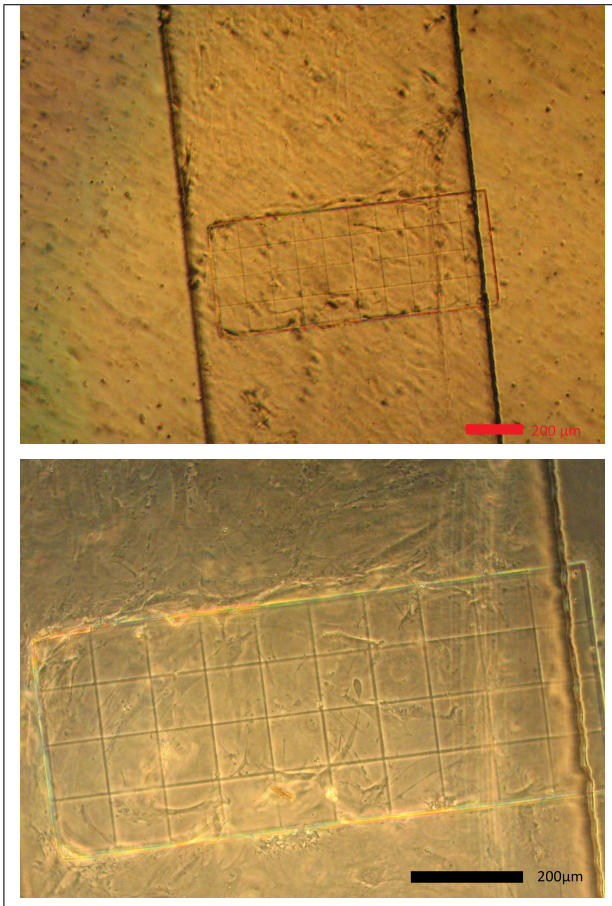	5	Healthy microenvironment. Cells and filopodia can be clearly seen.

Table C.5: *Optical images of cells on sheet for fused silica glass*

N-T

Images	Day	Comments
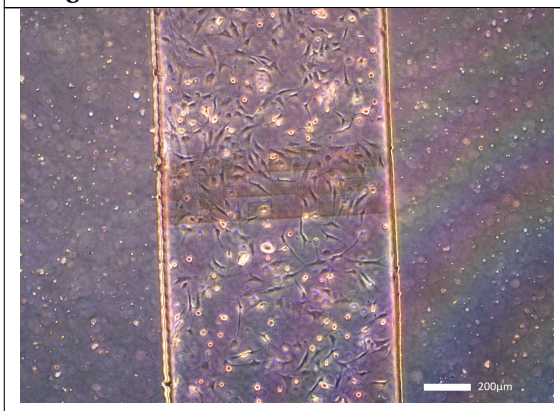 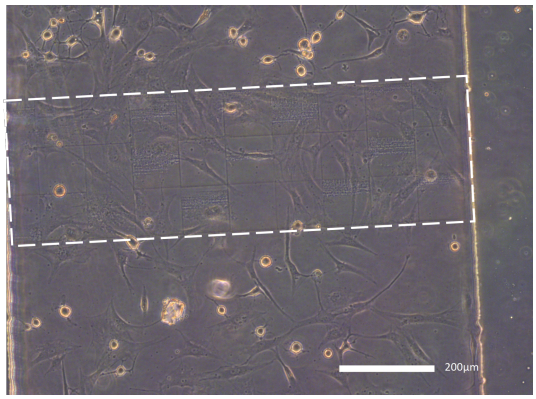	1	Uniform cell spreading can be seen with clear constrast between cells and pattern

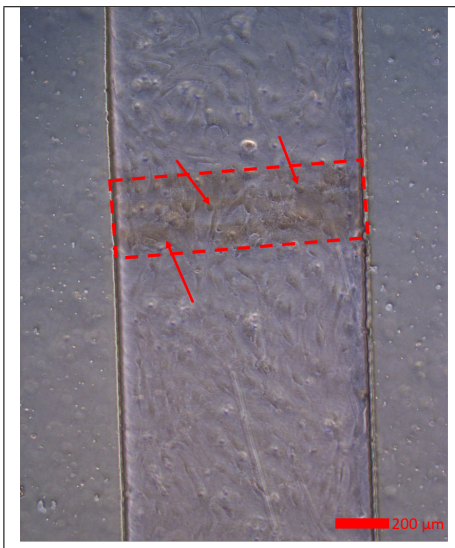 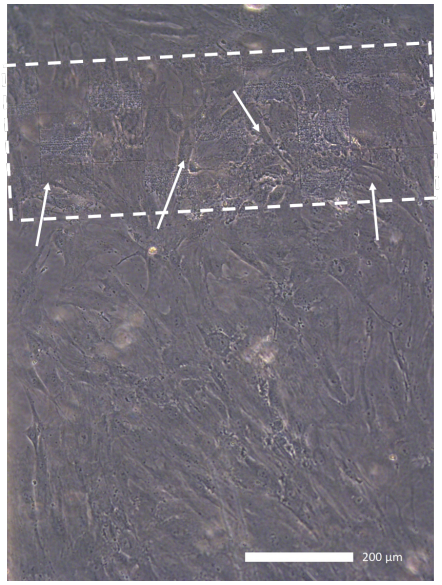	4	Cell imaging become more challenging as cells multiply and spread across the channel
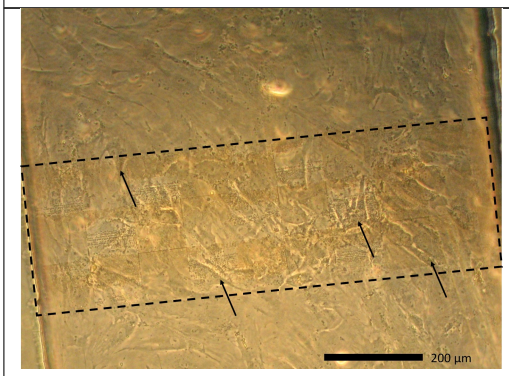	5	Difficult to focus and identify individual cells

Table C.6: *Optical images of cells on printed topography for fused silica glass*

NC

Images	Day	Comments
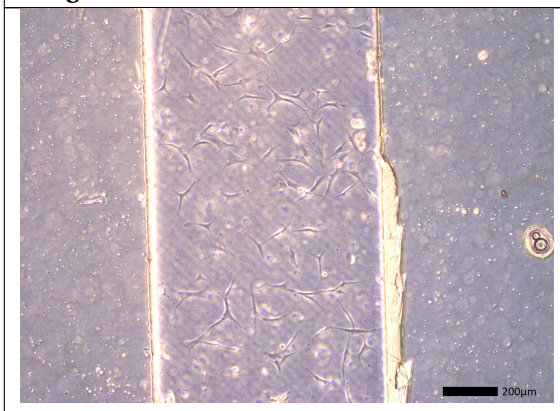	1	Non cytotoxic environment with uniform spreading
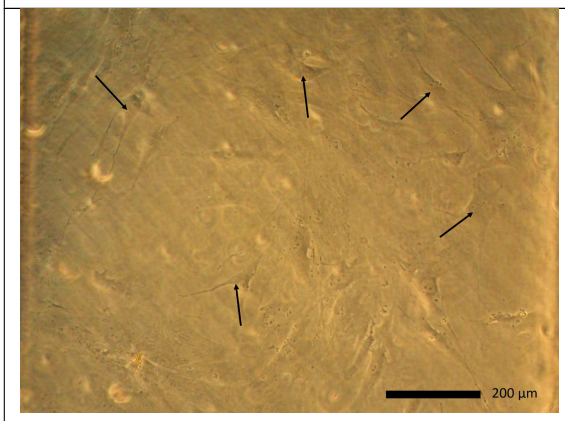	5	Loss in image quality and difficulty in imaging

Table C.7: *Optical images of cells on control area for fused silica glass*

Discussions: Optical Images

For all the optical images some common observations that were made are:

1. The microenvironment within the device is non cytotoxic. In all cases the cells show an elongated morphology with philopodia stretching out especially in day 4 and day 5 images.
2. Imaging becomes more complicated with increasing time. This may be attributed to the cells multiplying and spreading over the surfaces. Certain compounds secreted by the cells may also be hampering imaging. The contrast between the substrate and cells seems to decrease drastically.
3. No conclusions can be made whether cells prefer certain kinds of surfaces. The experiments needs more trials to make any conclusive remarks.

C.2. SEM Imaging

For the sample N-T, the pattern was damaged while removing PDMS from it. The sample theretofore, couldn't be imaged using SEM. I-SH was washed away during transfer to well plate. The scanning electron microscopy was done for the following samples:

- I-T
- N-SH
- IC
- NC

These have been discussed below:

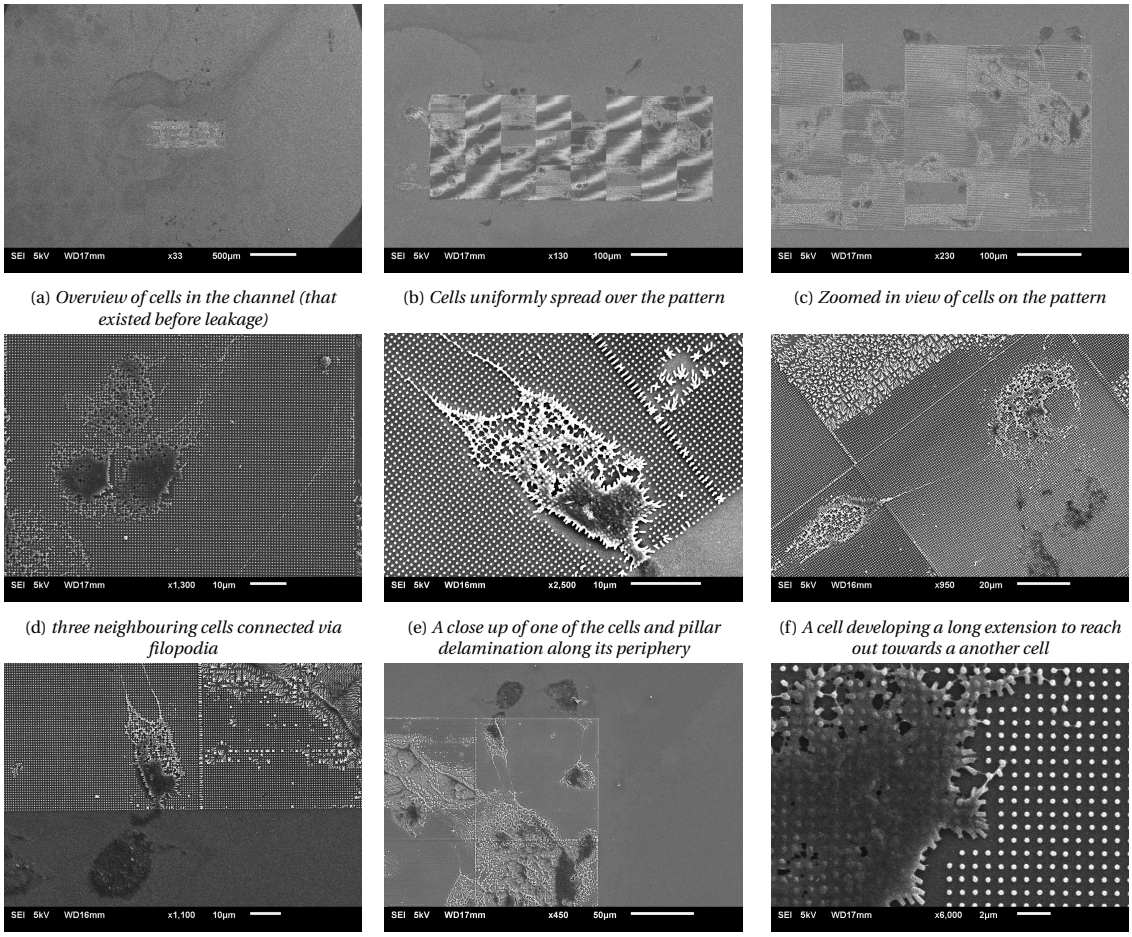

(a) *Overview of cells in the channel (that existed before leakage)*

(b) *Cells uniformly spread over the pattern*

(c) *Zoomed in view of cells on the pattern*

(d) *three neighbouring cells connected via filopodia*

(e) *A close up of one of the cells and pillar delamination along its periphery*

(f) *A cell developing a long extension to reach out towards a another cell*

(g) *zoomed in view of cell extensions and communication to neighbouring cell outside pattern*

(h) *Cells on and outside the pattern*

(i) *Cell filopodia bending the pillars*

Figure C.4: *Cells on pattern for sample I-T*

C.2.1. I-T

As discussed before, this sample was shifted to a well plate and the cell count reduced significantly. However, it is very interesting to see the cell attachment to the pattern. The cells appear to be dehydrated. This could have happened due to improper fixing procedure. The ethanol used for fixing or used to clean the sample could have been responsible for this. The filiopodia and cell connections show that the material is cytocompatible and the cells were able to attach to the pattern. It is also very interesting to see that the cells develop these filopodia along the pillars. The pillars seem to have bent and even delaminated in regions were the cells are attached. It is difficult to predict if this due to the forces cell exert on these pillars or whether this is due to cell shrinkage due to dehydration. Further studies are needed to identify the cause and magnitude of these attachment forces.

C.2.2. N-SH

SEM images of sample in figure C.5 depict more cell numbers towards the periphery than in the middle of the sheet. This is probably related to the fact that the sheet is flat in the middle and tends to curl upwards towards the periphery. This is a common fabrication defect encountered while printing sheets of large areas. Figures C.5e and C.5f depict cells at the top of the sheet towards the periphery connected to cells at the bottom via filopodia. This kind of a cell response depicts the non-cytotoxic environment within the channel.

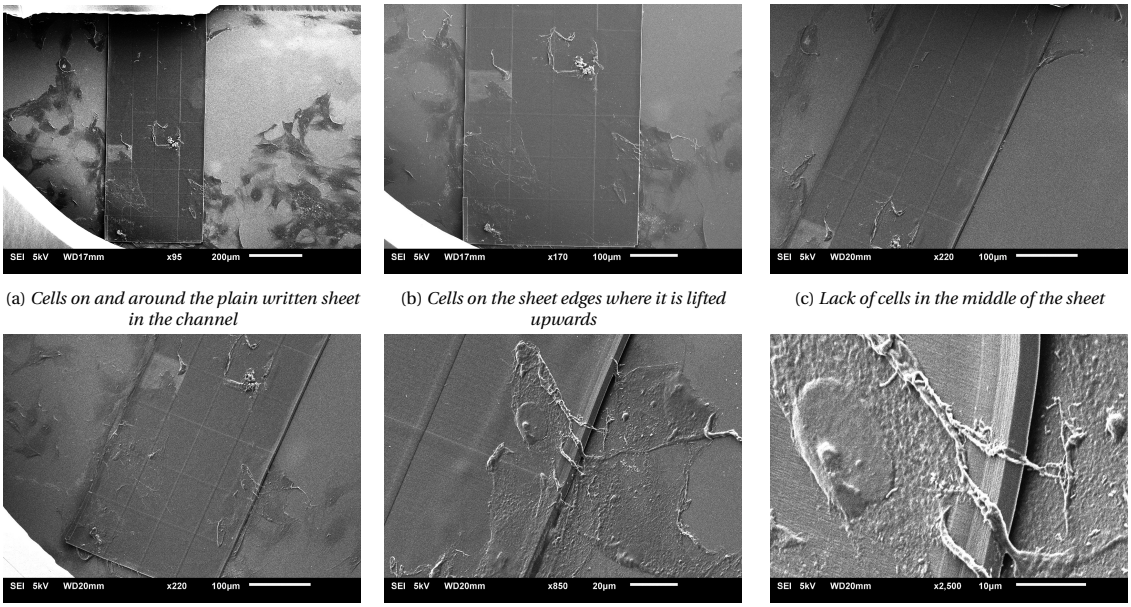

(a) *Cells on and around the plain written sheet in the channel*

(b) *Cells on the sheet edges where it is lifted upwards*

(c) *Lack of cells in the middle of the sheet*

(d) *Tilted view of sheet periphery with cells on it*

(e) *Cell on top of sheet with filopodia connected to a cell at the bottom*

(f) *Zoomed in view of filopodia in figure (e)*

Figure C.5: *Cells on sample N-SH*

C.2.3. IC, NC

Figure C.6 depicts the cells on control samples IC and NC. For sample NC, it can be seen that the cells have attached uniformly along the channel. For sample IC, the cells number has decreased drastically as a result of transferring sample to a well plate which involved PDMS removal and cleaning.

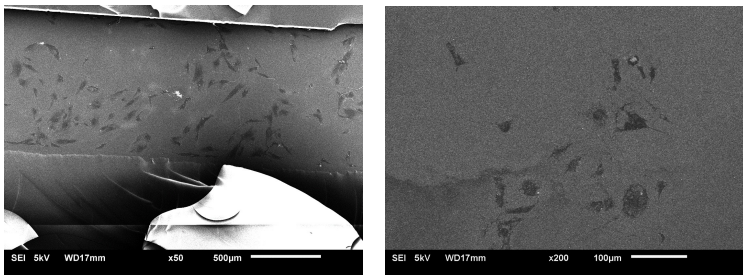

(a) *Cells along the channel in sample NC*

(b) *Cells on the sample IC which was later cultured in a well plate*

Figure C.6: *Increase in pattern quality correcting the sample tilt*

C.2.4. N-T

In case of pattern printed on fused silica glass, it is interesting to see that a few cells in the erased region still lay with filopodia covered in/on fallen pillars. It can't be said whether these pillars delaminated before or after the pattern was destroyed. However, the filopodia can be seen growing in the direction of the pattern. This is shown below in figure C.7. It is also interesting to see that the volume of cells at the inlet and outlets of the channel is much larger than that in other regions within the channel. This can be seen in figure C.8.

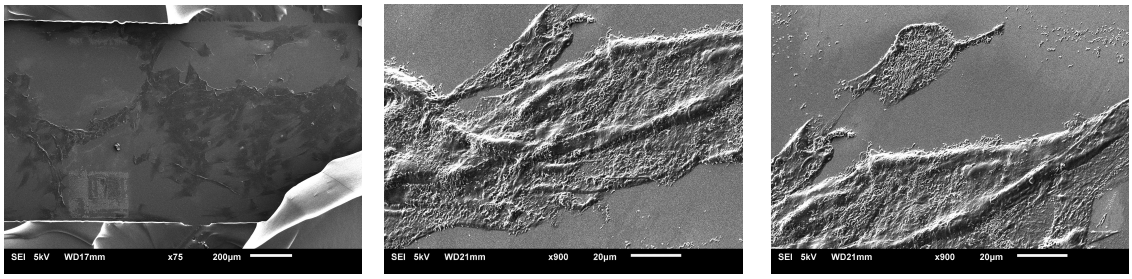

(a) *Overview of the cells within the channel of N-T. Notice unerased pattern at bottom left*

(b) *Cell on erased nanopattern with pillars embedded in/on it*

(c) *Cell growing through the region where pattern had previously existed*

Figure C.7: *Cell growth in sample N-T with erased pattern*

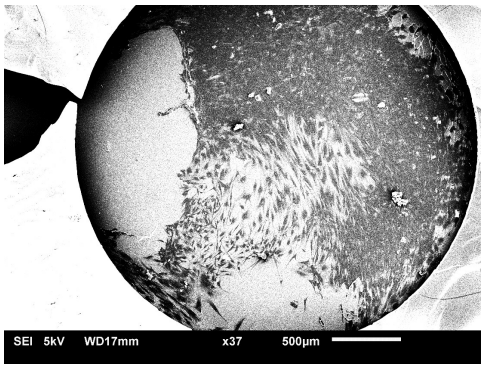

Figure C.8: *Increased Cell concentration in inlet and outlet of channel*

Discussion: SEM images

Some important conclusions that can be made via SEM imaging of the samples is:

1. Sample I-T depicts cells spread out along the pattern depicting an elongated morphology. This indicates that the environment was favourable for cell growth. Extensions or filopodia depict cells trying to use these submicron pillars for attachment and proliferation. Cells on pattern can also be seen connected to those outside. The pillars seem to bent or even delaminated in certain cases possibly due to forces exerted by the cells. In this case, the attachment of pillars with the substrate needs to be improved. This could be done by increasing interface distance or coating the glass with a layer that provides better adhesion to the resin.

2. For the sample N-SH, the cells can be seen preferring the periphery over the middle region due to the curling-up effect as discussed before. Cells on sheet can be seen connected to those beneath.

3. An increased concentration of cells is seen at the inlet and outlets than inside the channel. This can be due to the 90° bend in these regions which causes cells not being able to keep up with the sudden change in momentum.

4. Loss of cells in sample IC makes it difficult to comment about cell response while for sample NC, a uniform cell spreading is seen over the channel.

D

Nanoscribe Protocols

This chapter includes the codes and methods used to design the experiments or do measurements for some of the processes used in this study.

D.1. Printing in Galvo mode: Parametric Sweep

This section depicts carrying out a sample parametric sweep in Galvo mode. In this study, this was done in the conventional mode. In this case, the laser power (%), scan speed (μm/s), and interface distance were swept. The pillars were designed to be 200 nm in diameter and 200 nm high. They were interspaced at 1μm (centre to centre). The laser power was varied from 10% to 60% in steps of 10%. The scan speed increased from 1000 μm/s to 11000 μm/s in steps of 2000 μm/s. The interface distances 0 μm, 0.1 μm, and 0.2 μm were used. In this case, the slicing and hatching distances to create the pillars were also varied as 0.01 μm, 0.03 μm, and 0.05 μm.

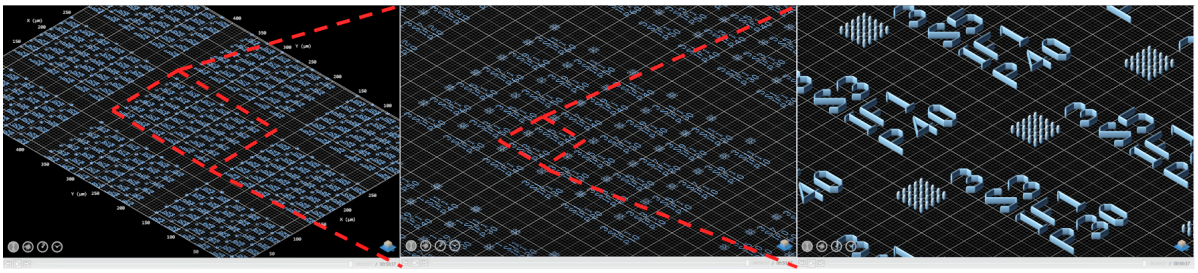

(a) *Parametric sweep as coded in Nanoscribe for galvo mode*

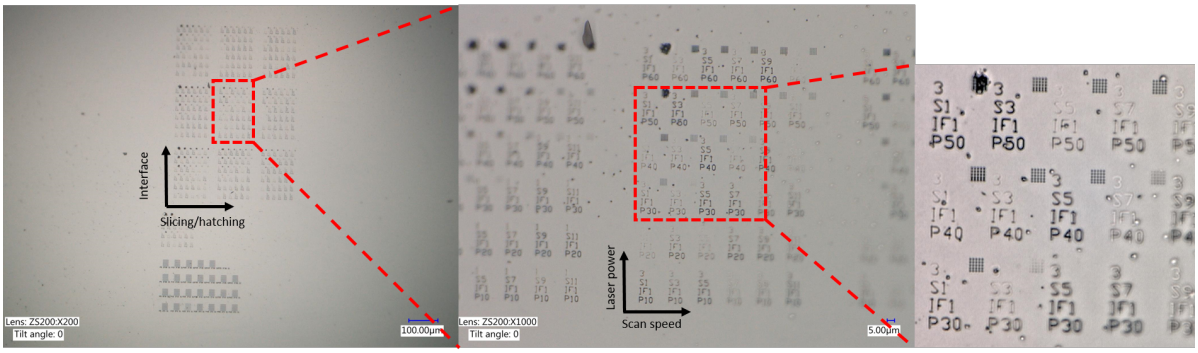

(b) *Optical micrograph of obtained parametric sweep*

Figure D.1: *Parametric sweep in Galvo mode. The figures in left show 9 blocks with each block printed for different interface distances and slicing/hatching distances. The middle figure contains a zoomed in block where in the laser power and scan speed are varied within this block. The right figure shows individual pillar arrays printed for each of these parameters.*

D.2. Printing in Piezo mode

This section depicts two sample codes for:

- **Parametric sweep:**
  Carrying out a parametric sweep in this mode for laser power, exposure time, and interface distances. The laser power was varied from 100% to 20% in steps of 20%. The exposure time was varied from 4000 μs to 880 μs in steps of 780 μs. The interface distance varies from 0 to 0.5 μm in steps of 0.1 μm. The code written for this using for loops generates digital pattern shown in Figure D.2a. Note that auto correction feature has been used here for illustration purpose. The resulting structures obtained have been shown in figure D.2b. Each single block has laser power vs time of exposure variation which are collectively varied with interface distance (in zoomed out image). The experiment is repeated 3 times.

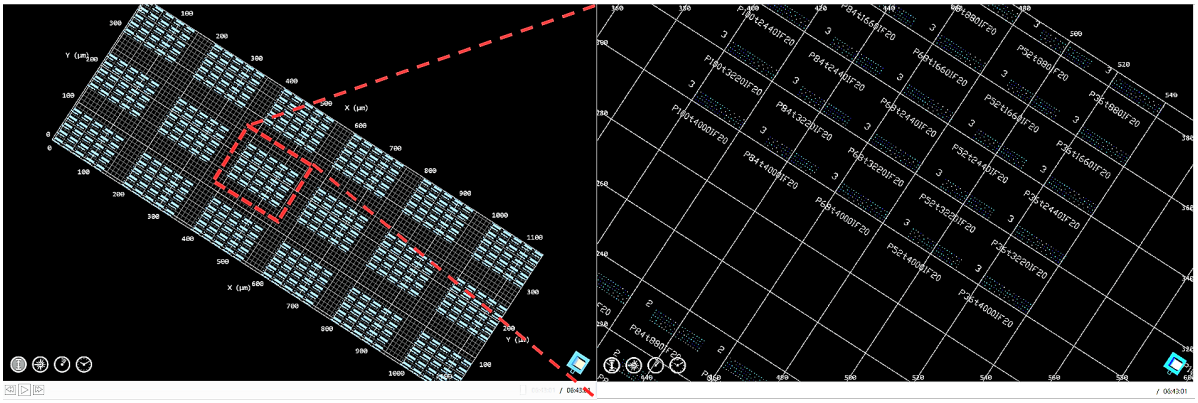

(a) *Parametric sweep as coded in Nanoscribe*

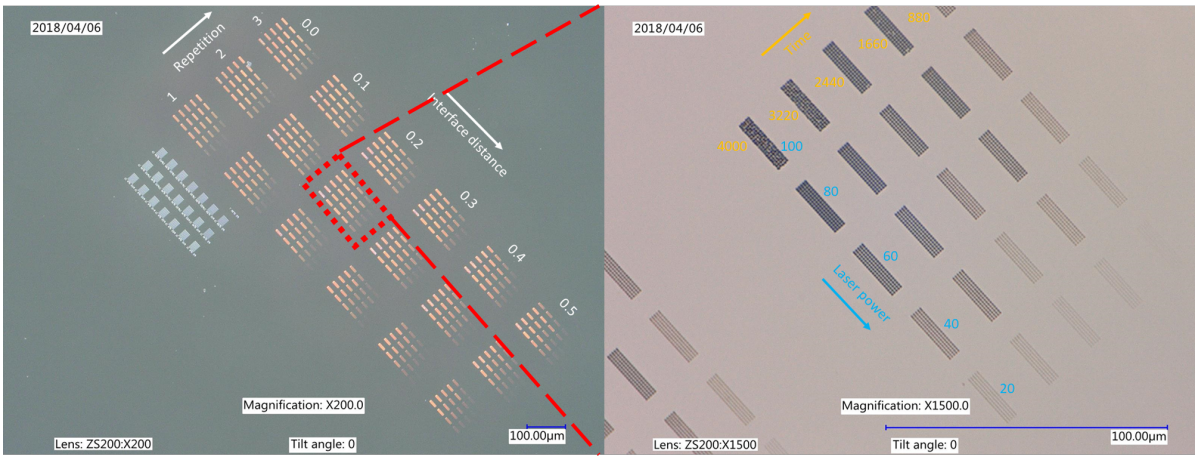

(b) *Optical micrograph of obtained parametric sweep*

Figure D.2: *Parametric sweep in Piezo mode. The left images depicts blocks that are different from each other based on interface distance and repetition (to check for reproducibility). The images on the right show a zoom in of one of these blocks wherein the laser power and time of exposure are being varied.*

- **Large area patterning:**
  Patterning large area of 2 mm * 2 mm onto the substrate. This is done for laser power 68%, interface distance of 0.3 μm and an exposure time of 2400 μs. The update rate is assumed to 10000 Hz. A manual tilt of 0.036° and 0.0556° has been used in x and y directions respectively in this case. Moving the stage is needed to stitch the large blocks together since the piezo can write only within a range of about 300*300 μm^2. This results in a digital pattern as shown in figure D.3.The optical image for this is depicted in figure 2.4(a).

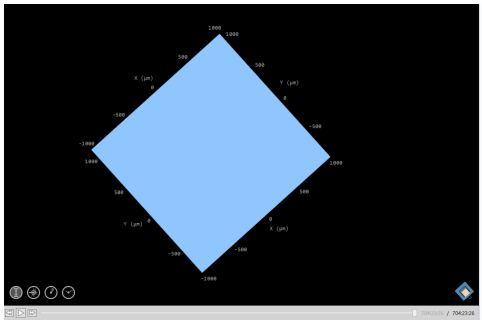

Figure D.3: *Nanoscribe code generated 2 mm×2 mm pattern using stitching patterns over large area. This is done by printing a small area (sub-area) of 100 µm × 100 µm first. While printing this small constituent area, the piezo element is moved in x and y directions. To print a new sub-area, the stage is moved in x and y and the piezo element is brought back to the original (0,0,0) position.*

D.3. Tilt correction in Piezo mode

The tilt measurement involved measuring the interface (z) for points across the x-y plane. It was found that doing so in the *Stage scan mode* allows scanning areas upto 18000×18000 μm^2. To avoid reaching this maximum limit, a 15000×15000 μm^2 was selected. The layout of these points is shown in section 3.2. Figure D.4a depicts the z value of the interface obtained for these points as a function of x and y coordinates. These points were plotted in MATLAB to obtain the surface plot as shown in figure D.4b. The tilt values in excel were obtained by fitting a linear curve to the plotted curves. Looking at figures D.4c and D.4d, one can see that the tilt of the substrate along X, keeping Y constant is different for different Y values. The same holds for traversing along Y for different abscissa. The surface of the substrate is not completely plain according to these measurements. However, this may be caused due to noise in detecting the interface accurately. Therefore necessary tilt compensations are needed using these measurements.

x \ y	0	3000	6000	9000	12000	15000
0	9879.935	9882.399	9885.148	9887.972	9889.924	9891.674
3000	9883.262	9885.285	9887.955	9890.569	9892.231	9893.904
6000	9886.727	9888.516	9890.919	9893.28	9894.828	9896.285
9000	9889.953	9891.615	9893.807	9896.016	9897.341	9898.66
12000	9893.561	9895.025	9897.028	9899.033	9900.148	9901.372
15000	9897.379	9898.424	9899.986	9901.829	9902.803	9903.861

	1	2	3	4	5	6	Average
Slope -x	0.000451	0.000537	0.000599	0.000658	0.00073	0.000801	0.000629
Tilt angle-x	0.02584	0.030768	0.03432	0.037701	0.041826	0.045894	0.036058
Slope -y	0.000816	0.000863	0.000928	0.000993	0.001156	0.001071	0.000971
Tilt angle-y	0.046753	0.049446	0.05317	0.056895	0.066234	0.061364	0.055644

(a) *Z values of interface summarised in an excel file*

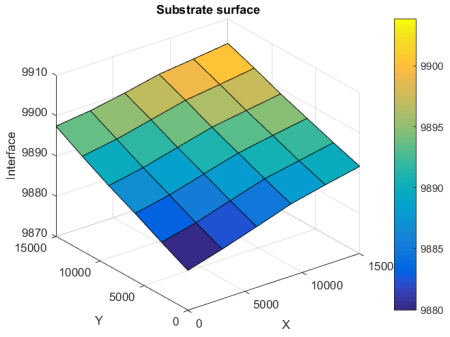

(b) *Plotting the surface using mapped points in MATLAB*

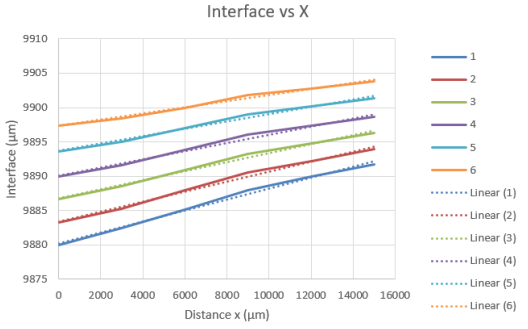

(c) *Tilts along x for various ordinates*

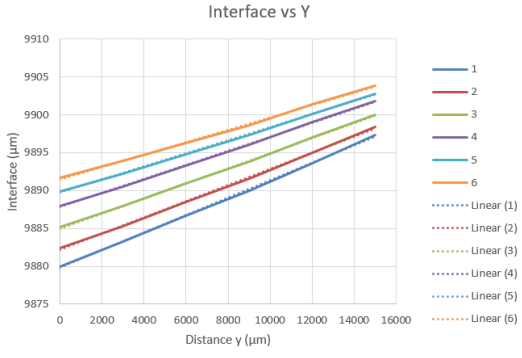

(d) *Tilts along y for various abscissa*

Figure D.4: *Tilt measurement methodology. This firstly involved mapping 36 points and plotting them in Excel or MATLAB, as shown in (a,b). Then the variation of tilt angles is calculated along x for different ordinates and similarly along y for different abscissa (c,d). The average of these tilt values yield the tilt angles inx and y directions.*

E

Other factors affecting bone regeneration

This section systematically discusses the literature on factors other than surface topography that affect bone regeneration.

E.1. Cell types involved

These are cells that are capable of proliferation and are unspecialised [96, 97]. They can differentiate into specific lineages in presence of appropriate cues/signals in their microenvironment, thus making them different from the other cell types [97]. The ease of cell extraction, multipotency, and less stringent rules for their use, make Mesenchymal stem cells (MSCs) the ideal source for bone tissue regeneration. Fig E.1 depicts the differentiation of MSCs into various lineages. MSCs are stimulated to differentiate into pre-osteoblasts using appropriate physical and biochemical cues/factors [3].

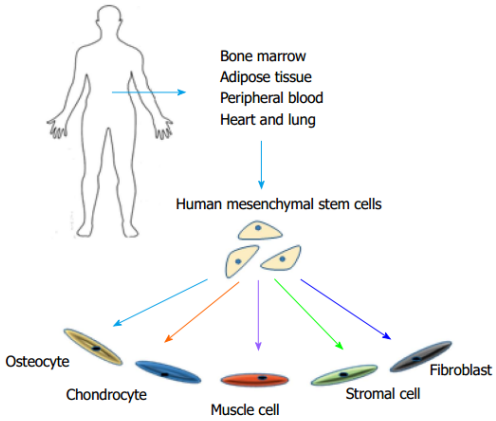

Figure E.1: *Differentiation of Mesenchymal stem cells into different lineages. Reproduced from[54]*

- *Embryonic stem cells:*
  These are derived from the inner mass of the embryo's blastocyst [96]. They are pluripotent and thus can give rise to every other cell type in the human body [98]. These are difficult to obtain and face problems due to ethical reasons.
- *Tissue-specific stem cells:*
  These cells are much more specialised than the embryonic type and give rise to very specific type of lineages [96, 97]. The example of such a type would be the hematopoietic stem cells that can only differentiate into various blood cell types [96].
- *Mesenchymal stem cells:*
  These are multipotent stem cells that are less potent than embryonic stem cells but can differentiate

into osteoblasts (bone cells), chondrocytes (cartilage cells), myocytes (muscle cells), adipocytes (fat cells) or more [13, 26, 99]. They are most commonly employed in bone-regeneration and are usually obtained from the aspirates of bone-marrow, adipose tissue or the umbilical cord tissue [3, 13, 26, 100]. MSCs are commonly used in such studies instead of other stem cell types since they possess the ability to self-renew and proliferate under appropriate conditions. They can be derived from small aspirate volumes from adults [54] and thus involve dealing with lesser ethical concerns and regulations.

- *Induced pluripotent stem cells:*
  These cells are developed by engineering adult cells (such as skin cells) to induce pluripotency by introducing certain genes into the adult cells [96, 98, 101]. These are highly promising due to the ease of obtaining them and lesser ethical concerns surrounding them.

E.2. Biomaterials

The extracellular matrix (mimicked using a scaffold/substrate) acts not only as a material for seeding cells, but also provides with the necessary mechanical and structural properties(cues) for the tissue, the required growth factors for their proliferation and differentiation as well as the signalling molecules for facilitating cell attachment and migration [8]. Some studies also involve the use of decellularised ECM as a biomimicking substrate for cell seeding and is produced by growing cells *in-vitro*, followed by a decellularisation procedure [102–104]. The current generation of biomedical materials aim at achieving bioactivity and(or) bio-resorption and promoting osteoconduction and osteoinduction while being able to mimic the cellular microenvironment. The most commonly used natural polymers for bone regeneration include Collagen type-I, Gelatin (a denatured form of collagen), Silk, Hyaluronic acid, Alginate and chitosan [3]. Owing to its presence as the major component in bone tissue, collagen would probably be the most suitable material for a bone regeneration. This however, is limited due to problems with production, risk of infection and tuning their properties and hence they are usually mixed with or replaced by other natural, synthetic (Polyesters, Copolymers) or inorganic biomaterials (ceramics, metals, composites) to increase strength, tune porosity or load growth factors/signalling molecules onto the substrate [105]. In general, synthetic polymers may be particularly suited in simulating the tissue regeneration microenvironment due the ease of tuning their properties (chemical, physical as well as mechanical), lower risks of degradation/infection and high reproducibility. Incorporating these into a graft would thus allow a systematic variation of the culture conditions [106].

Table E.1: *Different biomaterials and fabrication techniques for bone scaffolds*

Class of Material	**Components**	**Fabrication Techniques**	**Resolution/ Feature size Fabricated**	**References**
Natural Polymer	Collagen	Multi photon polymerisation using photo-initiators such as flavins, modified Benzophenone dimer and Rose Bengal di-isopropyl amine	$1\mu m$ [107], $1.06\mu m$ [87]	[87, 107–109]
		Collagen Hydrogel reinforced with randomly oriented Silk fibroins	Diameter of silk microfibers was $15\mu m$: limited due to fibre production method	[110]
		Low temperature 3D printing	$600\mu m$ rods printed	[111]
		Electrospinning pure collagen fibres	Down to $100nm$ [112, 113]	[112, 113]
		Electrospinning collagen fibres with Chitosan, poly (L-lactic acid-co-ϵ-caprolactone) (P(LLA-CL))	$226nm$ mean diameter based on weight ratios (without tolerances)	[114]
		Lyophization (freeze- drying)	$70\mu m$ mean pore size (based on concentration of collagen in solution)[115]	[115]

Table E.1 – *Continued from previous page*

	Chitosan	Freeze-Drying Chitosan-Alginate solution and cross linking using $CaCl_2$	100 – 300μm pore size	[116, 117]
		Free-drying chitosan-Hydroxyapatite hydrogel and then immersed in RGD solution	400μm pore size	[3, 118]
	Silk	Electrospinning silk fibroins	700nm [119], 800nm [120]	[119, 120]
		Freeze drying silk fibroins dissolved in different solvents and then leaching out NaCl particles	250 – 500μm for aqueous solution pores while 500 – 1000μm pores using hexafluoro-2-propanol (HFIP) solvent	[23]
	Hyaluronic acid	Electrospinning	Few tens of nm (depending on the air blow temperature)	[121]
		Photocuring hyaluronic acid hydrogel loaded with Simvastatin(SIM), an osteogenic agent, 2-aminoethyl methacrylate (AEMA) (a crosslinking agent) and Photocuring agent Irgacure D-2959	Porosity and pore sizes not evaluated but pore sizes increase with increasing AEMA content	[122]
Synthetic Polymer	Polyesters	Particle leaching calcium acetate out of a cross linked formulation of Poly(Propylene Fumarate) and Hydroxyapatite	Not evaluated but increasing porosity with increasing Calcium acetate: Hydroxyapatite ratio	[123, 124]
		Leaching out gelatin from freeze dried Poly(L-lactic acid)/gelatin solution	280 – 450μm pores	[125]
		3D printing Polycaprolactone scaffold, dipped in Platelet rich-plasma and freeze dried	250 – 380μm pores	[19]
	Copolymers	Electrospinning poly (L-lactic acid)-co-poly-(ϵ- caprolactone)/silk fibroin/ascorbic acid/tetracycline hydrochloride (PLACL/SF/AA/TC)	228 ± 62nm minimum fibre diameter, 1.5μm pore size	[126]
		Solutions of Poly(ethylene glycol)-Poly(caprolactone)-Poly(ethylene glycol) or PEG-PCL-PEG triblock copolymer (PECE), collagen and nano-hydroxyapatite mixed to obtain a hydrogel	A few to 40μm pore sizes	[127]

Table E.1 – *Continued from previous page*

Ceramic	Bioglass	Compacting a mixture of 45S5 Bioglass® and porogen Polyvinyl alcohol followed by sintering leading to porous bioglass scaffolds	Porosity and pore sizes undetermined. Presence of macro and micropores with former ranging in hundreds of microns and the latter in order of few tens of microns or lesser (according to SEM images)	[128]
	Coral Hydroxyapatite (CHA)	Hydrothermal conversion of coral skeleton to Hydroxyapatite	$100-600\mu m$ average pore size	[129, 130]
Metal	Magnesium	Compacting Mg powder with volatile spacer materials and sintering to create a Mg foam	Micropores of several microns diameter and macropores of $200-500\mu m$	[131]
	Titanium	Selective Laser Melting (SLM) of Ti6Al4V	$240-730\mu m$ pore size, thickness of 120 and 240 μm in two variants	[132]
	Tantalum	Chemical vapour deposition of Tantalum on a polymeric foam material	$400-700\mu m$ pore size	[133]
Composite	PCL/HA	Electrospinning PCL fibres containing Nano-apatite	$320-430nm$ fibre diameters	[134]
	Collagen/Calcium Phosphate cement	Collagen fibres added to a mixture of Alginate microbeads and Calcium Phosphate cement paste ($Ca_4(PO_4)_2O + CaHPO_4$)	Porosity and pore sizes not determined. Collagen fibre diameters from 0.1 to $3\mu m$, alginate microbeads from $20-100\mu m$	[135]

E.3. Young's Modulus (E)

As the culture substrate is intended to mimic the ECM of the tissue to be regenerated, it should be stiff enough to be able to provide the right microenvironment for the stem cells [26]. The modulus of elasticity affects cell proliferation, attachment, shape, spreading, migration as well as differentiation [136–142]. For bone regeneration, rigid substrates that enhance cell spreading, migration and lead to a well-defined cytoskeleton are preferred [140, 143, 144]. It has been found that soft substrates with modulus in the order of 0.1 to 1 *k*Pa lead to neural differentiation while those from 8-17 *k*Pa lead to myogenic differentiation and those above 34 *k*Pa lead to osteogenic differentiation of MSCs [26, 98, 145–147]. Substrate elasticity also has a more deciding role to play than the addition of appropriate growth factors alone [145]. It would be necessary in the future to analyse that to what extent the substrate's Young's modulus influences bone regeneration in the presence of other physical, mechanical and bio-chemical cues.

E.4. Porosity

Porosity refers to the percentage of void space present in a material [26]. Porosity, pore size as well as pore interconnection have a considerable impact on bone regeneration. A porous structure would allow vascularization, transport of minerals and oxygen, removal of waste products as well as provide an enhanced area to the cells for seeding and migration [148–150]. Porous structures also allow interlocking with the natural bone *in-vivo* especially for implant based applications [148, 151]. The presence of microporosity and nanoporosity within the material also plays a key role by providing a surface for protein adsorption and cell seeding

[148, 152, 153]. Higher scaffold porosity and pore sizes favour bone regeneration through enhanced osteoconduction and capillary formation due to increased surface area [1, 26, 154].
It has been reported that pores smaller than 100 μm in scaffolds hinder vascularisation [1, 155]. Pores even smaller than this may lead to non-mineralization and fibrous tissue formation [148, 155]. Too large pores would however lead to a compromise with the structural stability and reduce the area available for cell attachment [1, 156]. The porosity and pore sizes must be optimised to make sure that the structure is strong enough while its regeneration potential is not compromised with. There is no fixed pore size or porosity value available due to variations in reported values in literature [149]. This is attributed to the different cell types and sources employed as well as various fabrication techniques and biomaterials used in fabrication [26]. For scaffolds, macro as well as micro/nano porosity can be controlled while this is rather difficult for 2D/2.5D cultures.

E.5. Culture medium and growth factors

As mentioned before in section 1.1, the osteoblasts produce the ECM during bone formation constituted mainly by collagen, traces of glycoproteins (such as Alkaline Phosphatase (ALP), Osteopontin (OPN), Osteocalcin (OCN) etc.) and proteoglycans that provide compressive strength and growth factors (such as Bone morphogenic proteins (BMPs), Fibroblast growth factor (FGF), Transforming growth factor- β (TGF-β) etc.) [3]. These growth factors (proteins) can be coated or adsorbed onto the scaffold, incorporated into hydrogels (via diffusion for example) or encapsulated into microparticles [157, 158] to enhance bone regeneration by acting as a biochemical cue. Detection of ALP, OCN and OPN for example is also indicative of osteogenesis during bone regeneration. The solution properties such as its pH has also been identified as a key factor affecting the bone regeneration during fracture healing. An acidic microenvironment (pH = 6.4) for example, leads to the death of osteoblasts while an alkaline environment (pH = 7.4) increased cell viability [159].

The dynamic cell culture medium also exerts a shear force (owing to the laminar flow) onto the cells that acts a mechanical cue influencing their adhesion and morphology [48, 160]. Govey et al. pointed out that cells in bone also experience such a shear stress with at least 75% of the cells experiencing a force of 5 $dynes/cm^2$ [161]. Different mechanical forces acting on the cells within their dynamic microenvironment (including those due to the neighbouring cells, substrate elasticity, topography or fluid flow) affect cell fate or behaviour through various mechanobiological transduction pathways. Yang et al. and Kurth et al. highlighted the use of a microfluidic platform to conveniently control the shear force that acts on the cells as well as integrating this with the micro/nanotopographical cues within the same device [49, 160].

F

More about the 2PP process

F.1. Concept

A monomer along with a photoinitiator is employed in 2PP based fabrication. The photoinitiator upon activation using photons of appropriate energy, forms reactive species. These reactive species combine with the monomer to create polymeric chains, thus propagating the reaction until a saturation point at which the reaction terminates. The concept can be illustrated via the following equations from [79]:

$$PI \xrightarrow{2h\nu} PI^* \rightarrow R\bullet \quad \ldots \text{Initiation}$$

$$R\bullet + M \rightarrow R - M\bullet \quad \ldots \text{Progression}$$

$$RM\bullet + RM\bullet \rightarrow R - M - M - R \quad \ldots \text{Termination}$$

Where PI is the photoinitiator, PI* is the excited state of PI molecule and • is a free radical generated, M is the monomer molecule And '-' symbolises a covalent bond.

F.2. Tuning Young's modulus using 2PP

There is a lack of literature quantifying the mechanical properties of structures fabricated via 2PP. This can probably be attributed to the large number of interdependent parameters(laser, scanning as well as geometrical factors) influencing the structural strength . A few studies have reported the effect of laser power on the *Young's modulus* of the structures [162, 163]. Lemma et al. and LaFratta et al. concluded that an increasing laser power causes the structures to become stiffer (provided it is in the permissible range of fabrication for the resin) [163, 164]. For the IP series of photoresists, it was concluded that the Young's modulus (E) shows a linear dependence on the laser power and produces a hyperelastic respsonse at higher powers for structures with similar dimensions. The linear trend was not seen for ORMOCER and SU8 resists. This is shown in figure F.1. However, the absolute Young's modulus values vary within the literature. For example, Daraio group reported the maximum E for SU8 around 5 GPa while Lemma et al. found the maxima to be around 3 GPa (see figure F.1) [164, 165]. This difference is quite large and thus depicts the lack of reliable E values for such photopolymerisable materials.

F.3. Popular acrylate based resins used in 2PP

Nanoscribe GmbH provides with the following commonly used photoresist materials to fabricate structures. These have been summarised in table F.1.

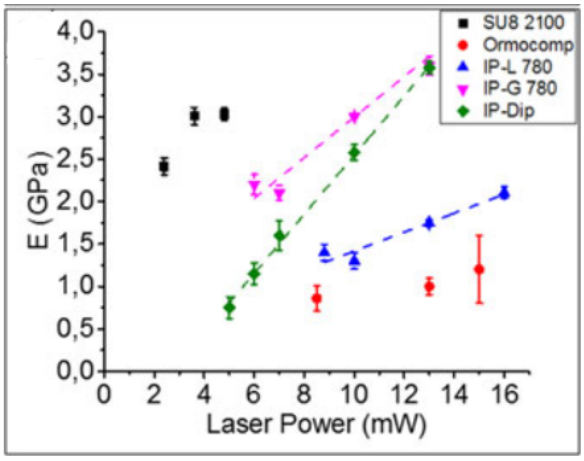

Figure F.1: *The effect of laser power on the material's Young's modulus (E). Reproduced from [164]*

Table F.1: *Commonly used 2PP resins*

Material	**Features**	**Advantages**	**Disadvantages**	**References**
IP-Dip	Liquid resist; used with high aperture objectives; E= 0.5 – 3.5 GPa; used with direct immersion of objective lens	High resolution (sub 100 nm); ready to use; drop casted; good adhesion to glass	Lower E than SU-8, IP-G; moderate shrinkage	[82, 164, 166]
IP-L	Liquid resist, drop casting onto substrate; E = 1-2 GPa; Oil immersion of objective	Low shrinkage; high resolution (sub 100 nm); good adhesion to glass; no pre or post baking needed; low shrinkage; ready to use; drop casted	Low mechanical strength	[82, 164, 166]
IP-S	Liquid negative resist, direct immersion of objective	Low shrinkage; fast structuring of large features; good adhesion to glass	Moderate resolution	[82, 166]
IP-G	Sol-gel resist, high viscosity drop casting; E = 2-3.5 GPa	Low shrinkage; high resolution up to 100 nm resolution; good adhesion to glass; no post baking needed; low thermal stresses; highest E among IP resists; drop cast or spin coat; complex 3D structuring possible	Prebake needed	[82, 164, 166]
SU8	Liquid negative resist; Young's modulus of about 5 GPa (higher than Ormocomp and IP resists)	Ease of availability; Available in different viscosities to tune film thickness; highest E	Spin coating needed; post bake needed	[164, 165]

Table F.1 – *Continued from previous page*

Ormocomp®	Liquid negative resist; E = 1-1.5 GPa	Ready to use; drop cast; highly transparent; good thermal and mechanical stability; Biocompatible	Low mechanical strength; medium shrinkage (5-7%)	[164, 167]

Bibliography

[1] Jan Henkel, Maria A. Woodruff, Devakara R. Epari, Roland Steck, Vaida Glatt, Ian C. Dickinson, Peter F. M. Choong, Michael A. Schuetz, and Dietmar W. Hutmacher. Bone Regeneration Based on Tissue Engineering Conceptions — A 21st Century Perspective. *Bone Research*, 1(3):216–248, 2013. ISSN 2095-4700. doi: 10.4248/BR201303002. URL http://www.nature.com/articles/boneres201317.

[2] Tao Gong, Jing Xie, Jinfeng Liao, Tao Zhang, Shiyu Lin, and Yunfeng Lin. Nanomaterials and bone regeneration. *Bone Research*, 3(July):15029, 2015. ISSN 2095-4700. doi: 10.1038/boneres.2015.29. URL http://www.nature.com/articles/boneres201529.

[3] Liliana Polo-Corrales, Magda Latorre-Esteves, and Jaime E Ramirez-Vick. Scaffold design for bone regeneration. *Journal of nanoscience and nanotechnology*, 14(1):15–56, jan 2014. ISSN 1533-4880. URL http://www.ncbi.nlm.nih.gov/pubmed/24730250http://www.pubmedcentral.nih.gov/articlerender.fcgi?artid=PMC3997175.

[4] M J Grimm and J L Williams. Measurements of permeability in human calcaneal trabecular bone. *Journal of biomechanics*, 30(7):743–5, jul 1997. ISSN 0021-9290. URL http://www.ncbi.nlm.nih.gov/pubmed/9239556.

[5] D M L Cooper, J R Matyas, M A Katzenberg, and B Hallgrimsson. Comparison of Microcomputed Tomographic and Microradiographic Measurements of Cortical Bone Porosity. doi: 10.1007/s00223-003-0071-z. URL https://link.springer.com/content/pdf/10.1007/s00223-003-0071-z.pdf.

[6] BME 332: Bone Structure-Function. URL http://www.umich.edu/{~}bme332/ch9bone/bme332bone.htm.

[7] S C Miller, L de Saint-Georges, B M Bowman, and W S Jee. Bone lining cells: structure and function. *Scanning microscopy*, 3(3):953–60; discussion 960–1, sep 1989. ISSN 0891-7035. URL http://www.ncbi.nlm.nih.gov/pubmed/2694361.

[8] Adele L Boskey. Bone composition: relationship to bone fragility and antiosteoporotic drug effects. *BoneKEy Reports*, 2(DECEMBER):1–11, 2013. ISSN 20476396. doi: 10.1038/bonekey.2013.181. URL http://www.portico.org/Portico/article?article=pgk2ph91gp6.

[9] F Barrère, T A Mahmood, K De Groot, and C A Van Blitterswijk. Advanced biomaterials for skeletal tissue regeneration: Instructive and smart functions. 2008. doi: 10.1016/j.mser.2007.12.001. URL http://www.csun.edu/{~}rdconner/536/additional/adv.biomaterials.tissue.regeneration.pdf.

[10] Rozalia Dimitriou, Elena Jones, Dennis McGonagle, and Peter V Giannoudis. Bone regeneration: current concepts and future directions. *BMC Medicine*, 9(1):66, 2011. ISSN 1741-7015. doi: 10.1186/1741-7015-9-66. URL http://bmcmedicine.biomedcentral.com/articles/10.1186/1741-7015-9-66.

[11] Thomas A. Einhorn. The cell and molecular biology of fracture healing. *Clinical orthopaedics and related research*, 355S(355):86–103, 1998. ISSN 0009-921X. doi: 10.1097/00003086-199810001-00003. URL http://www.ncbi.nlm.nih.gov/pubmed/9917622.

[12] Richard Marsell and Thomas A Einhorn. The biology of fracture healing. *Injury*, 42(6):551–5, jun 2011. ISSN 1879-0267. doi: 10.1016/j.injury.2011.03.031. URL http://www.ncbi.nlm.nih.gov/pubmed/21489527http://www.pubmedcentral.nih.gov/articlerender.fcgi?artid=PMC3105171.

[13] Hossein Ghanbari and Roghayyeh Vakili-Ghartavol. Bone Regeneration: Current Status and Future Prospects. In *Advanced Techniques in Bone Regeneration*. InTech, aug 2016. doi: 10.5772/63912. URL http://www.intechopen.com/books/advanced-techniques-in-bone-regeneration/bone-regeneration-current-status-and-future-prospects.

[14] Laurent Audigé, Damian Griffin, Mohit Bhandari, James Kellam, and Thomas P Rüedi. Path analysis of factors for delayed healing and nonunion in 416 operatively treated tibial shaft fractures. *Clinical orthopaedics and related research*, 438:221–32, sep 2005. ISSN 0009-921X. URL http://www.ncbi.nlm.nih.gov/pubmed/16131895.

[15] Amiethab Aiyer. Fracture Healing. URL https://www.orthobullets.com/basic-science/9009/fracture-healing.

[16] North Broward center for laser periodontics and impalnts. Autogenous Bone Grafts, Allogenic Bone, Xenogenic Bone, Bone Graft Subsitutes. URL http://northbrowardperio.com/services/bone-grafting/about-bone-grafting.

[17] University of Babylon. Biomaterials generations. URL http://www.uobabylon.edu.iq/eprints/publication{_}12{_}1581{_}1707.pdf.

[18] T. Albrektsson and C. Johansson. Osteoinduction, osteoconduction and osseointegration. *European Spine Journal*, 10:S96–S101, 2001. ISSN 09406719. doi: 10.1007/s005860100282.

[19] Junda Li, Meilin Chen, Xiaoying Wei, Yishan Hao, and Jinming Wang. Evaluation of 3D-printed polycaprolactone scaffolds coated with freeze-dried platelet-rich plasma for bone regeneration. *Materials*, 10(7), 2017. ISSN 19961944. doi: 10.3390/ma10070831.

[20] David Lickorish, John a M Ramshaw, Jerome a Werkmeister, Veronica Glattauer, and C Rolfe Howlett. Collagen-hydroxyapatite composite prepared by biomimetic process. *Journal of biomedical materials research. Part A*, 68(1):19–27, 2004. ISSN 1549-3296. doi: 10.1002/jbm.a.20031.

[21] Karen Choong. World ' s largest Science , Technology & Medicine Open Access book publisher c. *RFID Technology, Security Vulnerabilities, and Countermeasures*, 2016. ISSN 9789533070865. doi: 10.5772/711.

[22] Shorouk Fahmy-Garcia, Marjolein van Driel, Janneke Witte-Buoma, Heike Walles, Johannes Ptm van Leeuwen, Gerjo van Osch, and Eric Farrell. Nell-1, HMGB1 and CCN2 enhance migration and vasculogenesis, but not osteogenic differentiation compared to BMP2. *Tissue engineering. Part A*, page ten.TEA.2016.0537, 2017. ISSN 1937-335X. doi: 10.1089/ten.TEA.2016.0537. URL http://online.liebertpub.com/doi/10.1089/ten.TEA.2016.0537{%}0Ahttp://www.ncbi.nlm.nih.gov/pubmed/28463604.

[23] Cristina Correia, Sarindr Bhumiratana, Le-Ping Yan, Ana L. Oliveira, Jeffrey M. Gimble, Danielle Rockwood, David L. Kaplan, Rui A. Sousa, Rui L. Reis, and Gordana Vunjak-Novakovic. Development of silk-based scaffolds for tissue engineering of bone from human adipose-derived stem cells. *Acta Biomaterialia*, 8(7):2483–2492, 2012. ISSN 17427061. doi: 10.1016/j.actbio.2012.03.019. URL http://linkinghub.elsevier.com/retrieve/pii/S1742706112001055.

[24] Larry L Hench and Julia M Polak. Third-generation biomedical materials. *Science (New York, N.Y.)*, 295 (5557):1014–7, feb 2002. ISSN 1095-9203. doi: 10.1126/science.1067404. URL http://www.ncbi.nlm.nih.gov/pubmed/11834817.

[25] Yuqing Wan, Yong Wang, Zhimin Liu, Xue Qu, Buxing Han, Jianzhong Bei, and Shenguo Wang. Adhesion and proliferation of OCT-1 osteoblast-like cells on micro- and nano-scale topography structured poly(l-lactide). *Biomaterials*, 26(21):4453–4459, jul 2005. ISSN 01429612. doi: 10.1016/j.biomaterials.2004.11.016. URL http://www.ncbi.nlm.nih.gov/pubmed/15701374http://linkinghub.elsevier.com/retrieve/pii/S0142961204009986.

[26] Sonja Kress, Anne Neumann, Birgit Weyand, and Cornelia Kasper. Stem Cell Differentiation Depending on Different Surfaces. pages 263–283. Springer, Berlin, Heidelberg, 2011. doi: 10.1007/10_2011_108. URL http://link.springer.com/10.1007/10{_}2011{_}108.

[27] Anh Tuan Nguyen, Sharvari R Sathe, and Evelyn K F Yim. From nano to micro: topographical scale and its impact on cell adhesion, morphology and contact guidance. *Journal of Physics: Condensed Matter*, 28(18):183001, may 2016. ISSN 0953-8984. doi: 10.1088/0953-8984/28/18/183001. URL http://stacks.iop.org/0953-8984/28/i=18/a=183001?key=crossref.2a7e7197b062c2d57bf2acbc71e75ecb.

[28] Laura E. McNamara, Rebecca J. McMurray, Manus J. P. Biggs, Fahsai Kantawong, Richard O. C. Oreffo, and Matthew J. Dalby. Nanotopographical Control of Stem Cell Differentiation. *Journal of Tissue Engineering*, 1(1):120623, jan 2010. ISSN 2041-7314. doi: 10.4061/2010/120623. URL http://www.ncbi.nlm.nih.gov/pubmed/21350640http://www.pubmedcentral.nih.gov/articlerender.fcgi?artid=PMC3042612http://journals.sagepub.com/doi/10.4061/2010/120623.

[29] B Wójciak-Stothard, Zbigniew Madeja, Wlodzimierz Korohoda, Adam Curtis, and Christopher Wilkinson. Activation of macrophage-like cells by multiple grooved substrata. Topographical control of cell behaviour. *Cell Biology International*, 19(6):485–490, jun 1995. ISSN 10656995. doi: 10.1006/cbir.1995.1092. URL http://doi.wiley.com/10.1006/cbir.1995.1092.

[30] Matthew J Dalby, Mathis O Riehle, Stephen J Yarwood, Chris D W Wilkinson, and Adam S G Curtis. Nucleus alignment and cell signaling in fibroblasts: response to a micro-grooved topography. *Experimental cell research*, 284(2):274–82, apr 2003. ISSN 0014-4827. URL http://www.ncbi.nlm.nih.gov/pubmed/12651159.

[31] Sander Dobbenga, Lidy E. Fratila-Apachitei, and Amir A. Zadpoor. Nanopattern-induced osteogenic differentiation of stem cells – A systematic review. *Acta Biomaterialia*, 46:3–14, 2016. ISSN 18787568. doi: 10.1016/j.actbio.2016.09.031. URL http://dx.doi.org/10.1016/j.actbio.2016.09.031.

[32] H Kawahara, Y Soeda, K Niwa, M Takahashi, D Kawahara, and N Araki. In vitro study on bone formation and surface topography from the standpoint of biomechanics. (52):1297–1307. URL https://link.springer.com/content/pdf/10.1007{%}2Fs10856-004-5738-0.pdf.

[33] Junjie Li, Yan Dou, Jun Yang, Yuji Yin, Hong Zhang, Fanglian Yao, Haibin Wang, and Kangde Yao. Surface characterization and biocompatibility of micro- and nano-hydroxyapatite/chitosan-gelatin network films. *Materials Science and Engineering: C*, 29(4):1207–1215, may 2009. ISSN 09284931. doi: 10.1016/j.msec.2008.09.038. URL http://linkinghub.elsevier.com/retrieve/pii/S0928493108002646.

[34] Seunghan Oh, Chiara Daraio, Li-Han Chen, Thomas R. Pisanic, Rita R. Fiñones, and Sungho Jin. Significantly accelerated osteoblast cell growth on aligned TiO2 nanotubes. *Journal of Biomedical Materials Research Part A*, 78A(1):97–103, jul 2006. ISSN 1549-3296. doi: 10.1002/jbm.a.30722. URL http://www.ncbi.nlm.nih.gov/pubmed/16602089http://doi.wiley.com/10.1002/jbm.a.30722.

[35] Stefan Hengsbach and Andrés Díaz Lantada. Rapid prototyping of multi-scale biomedical microdevices by combining additive manufacturing technologies. *Biomedical Microdevices*, 16(4):617–627, 2014. ISSN 15728781. doi: 10.1007/s10544-014-9864-2.

[36] Matthew J. Dalby, Nikolaj Gadegaard, Rahul Tare, Abhay Andar, Mathis O. Riehle, Pawel Herzyk, Chris D. W. Wilkinson, and Richard O. C. Oreffo. The control of human mesenchymal cell differentiation using nanoscale symmetry and disorder. *Nature Materials*, 6(12):997–1003, dec 2007. ISSN 1476-1122. doi: 10.1038/nmat2013. URL http://www.nature.com/doifinder/10.1038/nmat2013.

[37] Penelope M Tsimbouri, Kate Murawski, Graham Hamilton, Pawel Herzyk, Richard O C Oreffo, Nikolaj Gadegaard, and Matthew J Dalby. A genomics approach in determining nanotopographical effects on MSC phenotype. *Biomaterials*, 34:2177–2184, 2013. doi: 10.1016/j.biomaterials.2012.12.019. URL https://ac.els-cdn.com/S0142961212013993/1-s2.0-S0142961212013993-main.pdf?{_}tid=505692c0-bcfb-11e7-9939-00000aacb360{&}acdnat=1509317503{_}622c52c9a2520f413dc9777f357dfde4.

[38] Fahsai Kantawong, Karl E V Burgess, Kamburapola Jayawardena, Andrew Hart, Richard J Burchmore, Nikolaj Gadegaard, Richard O C Oreffo, and Matthew J Dalby. Whole proteome analysis of osteoprogenitor differentiation induced by disordered nanotopography and mediated by ERK signalling. *Biomaterials*, 30:4723–4731, 2009. doi: 10.1016/j.biomaterials.2009.05.040. URL https://ac.els-cdn.com/S0142961209005456/1-s2.0-S0142961209005456-main.pdf?{_}tid=617273c6-bcfb-11e7-86b9-00000aacb361{&}acdnat=1509317531{_}8bdde5e19b61772f15c8e775e6c6acaf.

[39] Jingli Yang, Laura E. McNamara, Nikolaj Gadegaard, Enateri V. Alakpa, Karl V. Burgess, R. M. Dominic Meek, and Matthew J. Dalby. Nanotopographical Induction of Osteogenesis through Adhesion, Bone Morphogenic Protein Cosignaling, and Regulation of MicroRNAs. *ACS Nano*, 8(10):9941–9953, oct 2014. ISSN 1936-0851. doi: 10.1021/nn504767g. URL http://pubs.acs.org/doi/10.1021/nn504767g.

[40] Pierre Layrolle Sandrine Lavenus, Martine Berreur, Valerie Trichet, Paul Pilet, Guy Louran. ADHESION AND OSTEOGENIC DIFFERENTIATION OF HUMAN MESENCHYMAL STEM CELLS ON TITANIUM NANOPORES. *European Cells and Materials*, 22:2011–84, 2011. doi: 10.22203/eCM.v022a07. URL http://www.ecmjournal.org/papers/vol022/pdf/v022a07.pdf.

[41] Terje Sjö Strö M, Matthew J Dalby, Andrew Hart, Rahul Tare, Richard O C Oreffo, and Bo Su. Fabrication of pillar-like titania nanostructures on titanium and their interactions with human skeletal stem cells. 2009. doi: 10.1016/j.actbio.2009.01.007. URL https://ac.els-cdn.com/S1742706109000129/1-s2.0-S1742706109000129-main.pdf?{_}tid=1e7bd23c-bcfc-11e7-9052-00000aacb360{&}acdnat=1509317848{_}5664a20058f6cb1a3fe4fb80d25bc1be.

[42] Laura E Mcnamara, Terje Sjöström, Karl E V Burgess, Joseph J W Kim, Er Liu, Simon Gordonov, Prabhas V Moghe, R M Dominic Meek, Richard O C Oreffo, Bo Su, and Matthew J Dalby. Skeletal stem cell physiology on functionally distinct titania nanotopographies. *Biomaterials*, 32:7403–7410, 2011. doi: 10.1016/j.biomaterials.2011.06.063. URL https://ac.els-cdn.com/S0142961211007435/1-s2.0-S0142961211007435-main.pdf?{_}tid=2d0771d0-bcfc-11e7-8053-00000aacb35d{&}acdnat=1509317873{_}78e3445cea3e8b7b399ae8e25c5048c6.

[43] Terje Sjöström, Laura E. McNamara, R. M. Dominic Meek, Matthew J. Dalby, and Bo Su. 2D and 3D Nanopatterning of Titanium for Enhancing Osteoinduction of Stem Cells at Implant Surfaces. *Advanced Healthcare Materials*, 2(9):1285–1293, sep 2013. ISSN 21922640. doi: 10.1002/adhm.201200353. URL http://doi.wiley.com/10.1002/adhm.201200353.

[44] S. Guvendik, L. Trabzon, and M. Ramazanoglu. The Effect of Si Nano-Columns in 2-D and 3-D on Cellular Behaviour: Nanotopography-Induced CaP Deposition from Differentiating Mesenchymal Stem Cells. *Journal of Nanoscience and Nanotechnology*, 11(10):8896–8902, oct 2011. ISSN 15334880. doi: 10.1166/jnn.2011.3449. URL http://openurl.ingenta.com/content/xref?genre=article{&}issn=1533-4880{&}volume=11{&}issue=10{&}spage=8896.

[45] Joung Hyun Lee, Yexin Gu, Hongjun Wang, and Woo Y. Lee. Microfluidic 3D bone tissue model for high-throughput evaluation of wound-healing and infection-preventing biomaterials. *Biomaterials*, 33(4):999–1006, 2012. ISSN 01429612. doi: 10.1016/j.biomaterials.2011.10.036. URL http://dx.doi.org/10.1016/j.biomaterials.2011.10.036.

[46] Sangeeta N Bhatia and Donald E Ingber. Microfluidic organs-on-chips. *Nature Biotechnology*, 32(8):760–772, 2014. ISSN 1087-0156. doi: 10.1038/nbt.2989. URL http://www.nature.com/doifinder/10.1038/nbt.2989.

[47] Masoomeh Tehranirokh, Abbas Z. Kouzani, Paul S. Francis, and Jagat R. Kanwar. Microfluidic devices for cell cultivation and proliferation. *Biomicrofluidics*, 7(5):051502, sep 2013. ISSN 1932-1058. doi: 10.1063/1.4826935. URL http://aip.scitation.org/doi/10.1063/1.4826935.

[48] K W Kwon, S S Choi, B Kim, S N Lee, M C Park, P Kim, S H Lee, S H Park, and K Y Suh. A microfluidic flow sensor for measuring cell adhesion. *2006 5th IEEE Conference on Sensors*, pages 105–108, 2006. doi: 10.1109/ICSENS.2007.355729.

[49] Yong Yang, Karina Kulangara, Jaren Sia, Lu Wang, and Kam W. Leong. Engineering of a microfluidic cell culture platform embedded with nanoscale features. *Lab on a Chip*, 11(9):1638, 2011. ISSN 1473-0197. doi: 10.1039/c0lc00736f. URL http://xlink.rsc.org/?DOI=c0lc00736f.

[50] Bu Wang, Alex L. Weldon, Pisist Kumnorkaew, Bu Xu, James F. Gilchrist, and Xuanhong Cheng. Effect of surface nanotopography on immunoaffinity cell capture in microfluidic devices. *Langmuir*, 27(17):11229–11237, 2011. ISSN 07437463. doi: 10.1021/la2015868.

[51] Amrita Banerjee, R Perez-Castillejos, D Hahn, Alex I Smirnov, and H Grebel. Microfluidic Channels on Nanopatterned Substrates: Monitoring Protein Binding to Lipid Bilayers with Surface-Enhanced Raman Spectroscopy. *Chemical physics letters*, 489(1-3):121–126, apr 2010. ISSN 0009-2614. doi: 10.1016/j.cplett.2010.02.053. URL http://www.ncbi.nlm.nih.gov/pubmed/24932024http://www.pubmedcentral.nih.gov/articlerender.fcgi?artid=PMC4053208.

[52] J. T. Del Bonis-O'Donnell, W. Reisner, and D. Stein. Pressure-driven DNA transport across an artificial nanotopography. *New Journal of Physics*, 11, 2009. ISSN 13672630. doi: 10.1088/1367-2630/11/7/075032.

[53] Tohid Fatanat Didar and Maryam Tabrizian. Adhesion based detection, sorting and enrichment of cells in microfluidic Lab-on-Chip devices. *Lab on a Chip*, 10(22):3043, 2010. ISSN 1473-0197. doi: 10.1039/c0lc00130a. URL http://xlink.rsc.org/?DOI=c0lc00130a.

[54] Shima Salmasi, Deepak M Kalaskar, Wai-Weng Yoon, Gordon W Blunn, and Alexander M Seifalian. Role of nanotopography in the development of tissue engineered 3D organs and tissues using mesenchymal stem cells. *World journal of stem cells*, 7(2):266–80, 2015. ISSN 1948-0210. doi: 10.4252/wjsc.v7.i2.266. URL http://www.pubmedcentral.nih.gov/articlerender.fcgi?artid=4369486{&}tool=pmcentrez{&}rendertype=abstract.

[55] Jung Yul Lim and Henry J. Donahue. Cell Sensing and Response to Micro- and Nanostructured Surfaces Produced by Chemical and Topographic Patterning. *Tissue Engineering*, 13(8):1879–1891, 2007. ISSN 1076-3279. doi: 10.1089/ten.2006.0154. URL http://www.liebertonline.com/doi/abs/10.1089/ten.2006.0154.

[56] Makiko Goto, Takehiko Tsukahara, Kiichi Sato, and Takehiko Kitamori. Micro- and nanometer-scale patterned surface in a microchannel for cell culture in microfluidic devices. *Analytical and Bioanalytical Chemistry*, 390(3):817–823, 2008. ISSN 16182642. doi: 10.1007/s00216-007-1496-4.

[57] Sun Min Kim, Sung Hoon Lee, and Kahp Yang Suh. Cell research with physically modified microfluidic channels: A review. *Lab on a Chip*, 8(7):1015, 2008. ISSN 1473-0197. doi: 10.1039/b800835c. URL http://xlink.rsc.org/?DOI=b800835c.

[58] C. Vieu, F. Carcenac, A. Pépin, Y. Chen, M. Mejias, A. Lebib, L. Manin-Ferlazzo, L. Couraud, and H. Launois. Electron beam lithography: resolution limits and applications. *Applied Surface Science*, 164(1-4):111–117, sep 2000. ISSN 01694332. doi: 10.1016/S0169-4332(00)00352-4. URL http://linkinghub.elsevier.com/retrieve/pii/S0169433200003524.

[59] Vitor R. Manfrinato, Lihua Zhang, Dong Su, Huigao Duan, Richard G. Hobbs, Eric A. Stach, and Karl K. Berggren. Resolution Limits of Electron-Beam Lithography toward the Atomic Scale. *Nano Letters*, 13(4):1555–1558, apr 2013. ISSN 1530-6984. doi: 10.1021/nl304715p. URL http://pubs.acs.org/doi/10.1021/nl304715p.

[60] Stephen Y Chou, Peter R Krauss, Wei Zhang, Lingjie Guo, and Lei Zhuang. Sub-10 nm imprint lithography and applications. URL https://www.princeton.edu/{~}chouweb/publications/99Chou{_}Sub-10nmapplications{_}JVSTB{_}1997.pdf.

[61] J Damon Hoff, Li-Jing Cheng, Edgar Meyho, L Jay Guo, and Alan J Hunt. Nanoscale Protein Patterning by Imprint Lithography. doi: 10.1021/nl049758x. URL http://pubs.acs.org/doi/pdf/10.1021/nl049758x.

[62] Dengfeng Tan, Yan Li, Fengjie Qi, Hong Yang, Qihuang Gong, Xianzi Dong, and Xuanming Duan. Reduction in feature size of two-photon polymerization using SCR500. *Applied Physics Letters*, 90(7):071106, feb 2007. ISSN 0003-6951. doi: 10.1063/1.2535504. URL http://aip.scitation.org/doi/10.1063/1.2535504.

[63] Xian-Zi Dong, Zhen-Sheng Zhao, and Xuan-Ming Duan. Improving spatial resolution and reducing aspect ratio in multiphoton polymerization nanofabrication. *Applied Physics Letters*, 92(9):091113, mar 2008. ISSN 0003-6951. doi: 10.1063/1.2841042. URL http://aip.scitation.org/doi/10.1063/1.2841042.

[64] Linjie Li and John T Fourkas. Multiphoton polymerization. *Materials Today*, 10:30–37, 2007. doi: 10.1016/S1369-7021(07)70130-X. URL https://ac.els-cdn.com/S136970210770130X/1-s2.0-S136970210770130X-main.pdf?{_}tid=cf661ffa-c2e5-11e7-9595-00000aab0f6b{&}acdnat=1509967974{_}8e84de134c25233b3799dfdf9b51ac2e.

[65] Tushar Kumeria, Abel Santos, and Dusan Losic. Nanoporous Anodic Alumina Platforms: Engineered Surface Chemistry and Structure for Optical Sensing Applications. *Sensors*, 14(7):11878–11918, 2014. ISSN 1424-8220. doi: 10.3390/s140711878. URL http://www.mdpi.com/1424-8220/14/7/11878/.

[66] H. W. Deckman and J. H. Dunsmuir. Natural lithography. *Applied Physics Letters*, 41(4):377–379, aug 1982. ISSN 0003-6951. doi: 10.1063/1.93501. URL http://aip.scitation.org/doi/10.1063/1.93501.

[67] M A Wood. Colloidal lithography and current fabrication techniques producing in-plane nanotopography for biological applications. *Journal of the Royal Society, Interface*, 4(12):1–17, feb 2007. ISSN 1742-5689. doi: 10.1098/rsif.2006.0149. URL http://www.ncbi.nlm.nih.gov/pubmed/17015295http://www.pubmedcentral.nih.gov/articlerender.fcgi?artid=PMC2358954.

[68] Heinz D. Wanzenboeck and Simon Waid. Focused Ion Beam Lithography. *Recent Advances in Nanofabrication Techniques and Applications*, page 27, 2011. doi: 10.5772/22075. URL http://www.sciencedirect.com/science/article/pii/0168583X9390781Z{%}5Cnhttp://www.intechopen.com/books/recent-advances-in-nanofabrication-techniques-and-applications/focused-ion-beam-lithography.

[69] Byron D. Gates, Qiaobing Xu, Michael Stewart, Declan Ryan, , C. Grant Willson, and George M. Whitesides. New Approaches to Nanofabrication:Molding, Printing, and Other Techniques. 2005. doi: 10.1021/CR030076O. URL http://pubs.acs.org/doi/abs/10.1021/cr030076o.

[70] Stefan Walheim, Martin Bo, Ju Ltau, Rgen Mlynek, Georg Krausch, and Ullrich Steiner. Structure Formation via Polymer Demixing in Spin-Cast Films. URL http://pubs.acs.org/doi/pdf/10.1021/ma9619288.

[71] Abhijit Biswas, Ilker S. Bayer, Alexandru S. Biris, Tao Wang, Enkeleda Dervishi, and Franz Faupel. Advances in top–down and bottom–up surface nanofabrication: Techniques, applications & future prospects. *Advances in Colloid and Interface Science*, 170(1-2):2–27, jan 2012. ISSN 00018686. doi: 10.1016/j.cis.2011.11.001. URL http://www.ncbi.nlm.nih.gov/pubmed/22154364http://linkinghub.elsevier.com/retrieve/pii/S0001868611001904.

[72] Juan R. Maldonado and Martin Peckerar. X-ray lithography: Some history, current status and future prospects. *Microelectronic Engineering*, 161:87–93, 2016. ISSN 01679317. doi: 10.1016/j.mee.2016.03.052. URL http://dx.doi.org/10.1016/j.mee.2016.03.052.

[73] Ankit Chaudhari and Musa Ibrahim. Electron Beam and X-Ray Lithography. 2011. URL http://www.ece.umd.edu/class/enee416/GroupActivities/Ebeam.pdf.

[74] Craig J. Hawker and Thomas P. Russell. Block Copolymer Lithography: Merging "Bottom-Up" with "Top-Down" Processes. *MRS Bulletin*, 30(12):952–966, dec 2005. ISSN 0883-7694. doi: 10.1557/mrs2005.249. URL http://www.journals.cambridge.org/abstract{_}S0883769400014263.

[75] Manuela T. Raimondi, Shane M. Eaton, Michele M. Nava, Matteo Laganà, Giulio Cerullo, and Roberto Osellame. Two-photon laser polymerization: from fundamentals to biomedical application in tissue engineering and regenerative medicine. *Journal of Applied Biomaterials & Biomechanics*, 10(1):0–0, 2012. ISSN 1722-6899. doi: 10.5301/JABB.2012.9249. URL http://www.jabb.biz/Navigator.action?cmd=navigate{&}urlkey=Abstract{&}t=JABB{&}UidArticle=447EA945-0C6C-4091-AD05-64C4FB8CCB1D.

[76] Boris N Chichkov and Andreas Ostendorf. Two-Photon Polymerization: A New Approach to Micromachining. *Photonics Spectra*, 40(October):72–79, 2006. ISSN 07311230. doi: 10.1016/j.jphotochem.2006.03.004.

[77] Serge L Li Hoi Foo-gregory. ANALYSIS OF TWO-PHOTON POLYMERIZATION FOR THE DEVELOPMENT OF A RECONFIGURABLE MICRO-DEVICE MANUFACTURING SYSTEM by. 2012.

[78] Qin Hu. Multiphoton Lithography Based 3D Micro/Nano Printing.

[79] Xiaoqin Zhou, Yihong Hou, and Jieqiong Lin. A review on the processing accuracy of two-photon polymerization. *AIP Advances*, 5(3), 2015. ISSN 21583226. doi: 10.1063/1.4916886.

[80] Bo Tan, Krishnan Venkatakrishnan, and Alexander Makaronets. Effects of pulsewidth on two-photon polymerization. *Designed Monomers and Polymers*, 16(2):145–150, 2013. ISSN 1385772X. doi: 10.1080/15685551.2012.705502.

[81] Hong-Bo Sun, Tomokazu Tanaka, and Satoshi Kawata. Three-dimensional focal spots related to two-photon excitation. *APPLIED PHYSICS LETTERS*, 80:3673. doi: 10.1063/1.1478128. URL http://nathan.instras.com/MyDocsDB/doc-710.pdf.

[82] Nanoscribe GmbH. True 3D Laser Lithography. pages 1–16, 2011. URL www.nanoscribe.de/data/Ressources/23{_}1-Nanoscribe{_}GmbH{_}Booklet{_}Version{_}2.2.pdf.

[83] Rainer Wittig, Erik Waller, Georg von Freymann, and Rudolf Steiner. Direct laser writing-mediated generation of standardized topographies for dental implant surface optimization. *Journal of Laser Applications*, 24(4):042011, 2012. ISSN 1042-346X. doi: 10.2351/1.4728135. URL http://lia.scitation.org/doi/10.2351/1.4728135.

[84] Maria Farsari, Maria Vamvakaki, and Boris N Chichkov. Multiphoton polymerization of hybrid materials. *Journal of Optics*, 12(12):124001, 2010. ISSN 2040-8978. doi: 10.1088/2040-8978/12/12/124001. URL http://stacks.iop.org/2040-8986/12/i=12/a=124001?key=crossref.e1b33bb4f31e10ece0358d27c0b392fa.

[85] Barbara Spagnolo, Virgilio Brunetti, Godefroy Leménager, Elisa De Luca, Leonardo Sileo, Teresa Pellegrino, Pier Paolo Pompa, Massimo De Vittorio, and Ferruccio Pisanello. Three-dimensional cage-like microscaffolds for cell invasion studies. *Scientific Reports*, 5(1):10531, 2015. ISSN 2045-2322. doi: 10.1038/srep10531. URL http://www.nature.com/articles/srep10531.

[86] Michele M. Nava, Nunzia Di Maggio, Tommaso Zandrini, Giulio Cerullo, Roberto Osellame, Ivan Martin, and Manuela T. Raimondi. Synthetic niche substrates engineered via two-photon laser polymerization for the expansion of human mesenchymal stromal cells. *Journal of Tissue Engineering and Regenerative Medicine*, (June 2016):2836–2845, 2016. ISSN 19327005. doi: 10.1002/term.2187.

[87] Swarna Basu, Lawrence P. Cunningham, George D. Pins, Katie A. Bush, Rosa Taboada, Amy R. Howell, Jun Wang, and Paul J. Campagnola. Multiphoton excited fabrication of collagen matrixes cross-linked by a modified benzophenone dimer: Bioactivity and enzymatic degradation. *Biomacromolecules*, 6(3):1465–1474, 2005. ISSN 15257797. doi: 10.1021/bm049258y.

[88] Attilio Marino, Gianni Ciofani, Carlo Filippeschi, Mario Pellegrino, Monica Pellegrini, Paolo Orsini, Massimo Pasqualetti, Virgilio Mattoli, and Barbara Mazzolai. Two-photon polymerization of submicrometric patterned surfaces: Investigation of cell-substrate interactions and improved differentiation of neuron-like cells. *ACS Applied Materials and Interfaces*, 5(24):13012–13021, 2013. ISSN 19448244. doi: 10.1021/am403895k.

[89] A. Ovsianikov, M. Malinauskas, S. Schlie, B. Chichkov, S. Gittard, R. Narayan, M. Löbler, K. Sternberg, K. P. Schmitz, and A. Haverich. Three-dimensional laser micro- and nano-structuring of acrylated poly(ethylene glycol) materials and evaluation of their cytoxicity for tissue engineering applications. *Acta Biomaterialia*, 7(3):967–974, 2011. ISSN 17427061. doi: 10.1016/j.actbio.2010.10.023. URL http://dx.doi.org/10.1016/j.actbio.2010.10.023.

[90] Mincho Kavaldzhiev, Jose Efrain Perez, Yurii Ivanov, Andrea Bertoncini, Carlo Liberale, and Jürgen Kosel. Biocompatible 3D printed magnetic micro needles. *Biomedical Physics & Engineering Express*, 3(2):1–9, 2017. ISSN 2057-1976. doi: 10.1088/2057-1976/aa5ccb. URL http://dx.doi.org/10.1088/2057-1976/aa5ccb.

[91] Michele M. Nava, Alessio Piuma, Marina Figliuzzi, Irene Cattaneo, Barbara Bonandrini, Tommaso Zandrini, Giulio Cerullo, Roberto Osellame, Andrea Remuzzi, and Manuela T. Raimondi. Two-photon polymerized "nichoid" substrates maintain function of pluripotent stem cells when expanded under feeder-free conditions. *Stem Cell Research & Therapy*, 7(1):132, 2016. ISSN 1757-6512. doi: 10.1186/s13287-016-0387-z. URL http://stemcellres.biomedcentral.com/articles/10.1186/s13287-016-0387-z.

[92] Yih-Lin Cheng, Yi-Wen Chen, Kan Wang, and Ming-You Shie. Enhanced adhesion and differentiation of human mesenchymal stem cell inside apatite-mineralized/poly(dopamine)-coated poly(ϵ-caprolactone) scaffolds by stereolithography. *Journal of Materials Chemistry B*, 4(38):6307–6315, sep 2016. ISSN 2050-750X. doi: 10.1039/C6TB01377E. URL http://xlink.rsc.org/?DOI=C6TB01377E.

[93] Srinath Satyanarayana, Rohit N Karnik, and Arunava Majumdar. Stamp-and-Stick Room-Temperature Bonding Technique for Microdevices. *JOURNAL OF MICROELECTROMECHANICAL SYSTEMS*, 14 (2), 2005. doi: 10.1109/JMEMS.2004.839334. URL http://www-mtl.mit.edu/researchgroups/mems-salon/Stamp-Stick-Bonding-Technique.pdf.

[94] Nanoscribe. Nanoscribe Photonics Professional GT Manual. Technical Report September, Nanoscribe GmbH, 2013. URL https://snf.stanford.edu/SNF/equipment/nSiL/nanoscribe-photonics-professional-gt/nanoscribe-photonics-professional-gt-manual/view.

[95] Refractive index database. URL https://refractiveindex.info/.

[96] International Society for Stem Cell Research. Types of Stem Cells. URL http://www.closerlookatstemcells.org/learn-about-stem-cells/types-of-stem-cells.

[97] Stem Cell Basics I. | stemcells.nih.gov. URL https://stemcells.nih.gov/info/basics/1.htm.

[98] Michele M. Nava, Manuela T. Raimondi, and Riccardo Pietrabissa. Controlling self-renewal and differentiation of stem cells via mechanical cues. *Journal of Biomedicine and Biotechnology*, 2012, 2012. ISSN 11107243. doi: 10.1155/2012/797410.

[99] Malcolm. Alison, Anna M. Wobus, and Kenneth R. Boheler. *Stem cells*. Springer, 2006. ISBN 3540778551. URL https://books.google.nl/books?id=aGyqLIoP1kUC{&}pg=PA248{&}redir{_}esc=y.

[100] Ralf Hass, Cornelia Kasper, Stefanie Böhm, and Roland Jacobs. Different populations and sources of human mesenchymal stem cells (MSC): A comparison of adult and neonatal tissue-derived MSC. *Cell communication and signaling : CCS*, 9:12, may 2011. ISSN 1478-811X. doi: 10.1186/1478-811X-9-12. URL http://www.ncbi.nlm.nih.gov/pubmed/21569606http://www.pubmedcentral.nih.gov/articlerender.fcgi?artid=PMC3117820.

[101] Kazutoshi Takahashi and Shinya Yamanaka. Induction of Pluripotent Stem Cells from Mouse Embryonic and Adult Fibroblast Cultures by Defined Factors. *Cell*, 126(4):663–676, aug 2006. ISSN 00928674. doi: 10.1016/j.cell.2006.07.024. URL http://linkinghub.elsevier.com/retrieve/pii/S0092867406009767.

[102] Marta Baroncelli, Bram C. van der Eerden, Yik Yang Kan, Rodrigo D. Alves, Jeroen A. Demmers, Jeroen van de Peppel, and Johannes P. van Leeuwen. Comparative proteomic profiling of human osteoblast-derived extracellular matrices identifies proteins involved in mesenchymal stromal cell osteogenic differentiation and mineralization. *Journal of Cellular Physiology*, (March):1–9, 2017. ISSN 10974652. doi: 10.1002/jcp.25898.

[103] Lindsay E Fitzpatrick and Todd C McDevitt. Cell-derived matrices for tissue engineering and regenerative medicine applications. *Biomaterials science*, 3(1):12–24, jan 2015. ISSN 2047-4849. doi: 10.1039/C4BM00246F. URL http://www.ncbi.nlm.nih.gov/pubmed/25530850http://www.pubmedcentral.nih.gov/articlerender.fcgi?artid=PMC4270054.

[104] Hongxu Lu, Takashi Hoshiba, Naoki Kawazoe, Ichie Koda, Minghui Song, and Guoping Chen. Cultured cell-derived extracellular matrix scaffolds for tissue engineering. *Biomaterials*, 32(36):9658–9666, dec 2011. ISSN 01429612. doi: 10.1016/j.biomaterials.2011.08.091. URL http://www.ncbi.nlm.nih.gov/pubmed/21937104http://linkinghub.elsevier.com/retrieve/pii/S0142961211010398.

[105] Chanjuan Dong and Yonggang Lv. Application of collagen scaffold in tissue engineering: Recent advances and new perspectives. *Polymers*, 8(2):1–20, 2016. ISSN 20734360. doi: 10.3390/polym8020042.

[106] Lidy Fratila. REGENERATIVE MEDICINE Lecture 3 Biomaterials for RM Biomaterials for RM.

[107] Alex Bell, Matthew Kofron, and Vasile Nistor. Multiphoton crosslinking for biocompatible 3D printing of type I collagen. *Biofabrication*, 7(3):035007, 2015. ISSN 1758-5090. doi: 10.1088/1758-5090/7/3/035007. URL http://stacks.iop.org/1758-5090/7/i=3/a=035007?key=crossref.db71617abd8f44585648c88cd067af9c.

[108] J Pitts, a Howell, R Taboada, I Banerjee, J Wang, S Goodman, and P Campagnola. New Photoactivators for Multiphoton Excited Three-dimensional Submicron Cross-linking of Proteins: Bovine Serum Albumin and Type 1 Collagen¶†. *Photochemistry and photobiology*, 76(2):135–144, 2002. ISSN 0031-8655. doi: 10.1562/0031-8655(2002)076<0135:npfmet>2.0.co;2. URL http://eutils.ncbi.nlm.nih.gov/entrez/eutils/elink.fcgi?dbfrom=pubmed{&}id=12194208{&}retmode=ref{&}cmd=prlinks{%}5Cnfile:///Users/Eric/Library/ApplicationSupport/Papers2/Articles/Photochemistryandphotobiology/2002/Pitts-NewPhotoactivatorsforMultiphotonExc.

[109] Sheldon J. J. Kwok, Ivan A. Kuznetsov, Moonseok Kim, Myunghwan Choi, Giuliano Scarcelli, and Seok Hyun Yun. Selective two-photon collagen crosslinking in situ measured by Brillouin microscopy. *Optica*, 3(5):469, 2016. ISSN 2334-2536. doi: 10.1364/OPTICA.3.000469. URL https://www.osapublishing.org/optica/abstract.cfm?URI=optica-3-5-469{%}5Cnhttps://www.osapublishing.org/abstract.cfm?URI=optica-3-5-469.

[110] Mariana Agostini de Moraes, Estelle Paternotte, Diego Mantovani, and Marisa Masumi Beppu. Mechanical and Biological Performances of New Scaffolds Made of Collagen Hydrogels and Fibroin Microfibers for Vascular Tissue Engineering. *Macromolecular Bioscience*, 12(9):1253–1264, sep 2012. ISSN 16165187. doi: 10.1002/mabi.201200060. URL http://doi.wiley.com/10.1002/mabi.201200060.

[111] Kai Feng Lin, Shu He, Yue Song, Chun Mei Wang, Yi Gao, Jun Qin Li, Peng Tang, Zheng Wang, Long Bi, and Guo Xian Pei. Low-Temperature Additive Manufacturing of Biomimic Three-Dimensional Hydroxyapatite/Collagen Scaffolds for Bone Regeneration. *ACS Applied Materials and Interfaces*, 8(11):6905–6916, 2016. ISSN 19448252. doi: 10.1021/acsami.6b00815.

[112] † Jamil A. Matthews, ‡ Gary E. Wnek, , § David G. Simpson, and ‖ Gary L. Bowlin*. Electrospinning of Collagen Nanofibers. 2002. doi: 10.1021/BM015533U. URL http://pubs.acs.org/doi/abs/10.1021/bm015533u.

[113] Scott A Sell, Michael J Mcclure, Koyal Garg, Patricia S Wolfe, and Gary L Bowlin. Electrospinning of collagen/biopolymers for regenerative medicine and cardiovascular tissue engineering. *Advanced Drug Delivery Reviews*, 61:1007–1019, 2009. doi: 10.1016/j.addr.2009.07.012. URL https://ac.els-cdn.com/S0169409X09002257/1-s2.0-S0169409X09002257-main.pdf?{_}tid=e4c52584-b9db-11e7-8c31-00000aab0f6b{&}acdnat=1508974157{_}32a9a3d16748d59258205527716973d4.

[114] Anlin Yin, Kuihua Zhang, Michael J. McClure, Chen Huang, Jinglei Wu, Jun Fang, Xiumei Mo, Gary L. Bowlin, Salem S. Al-Deyab, and Mohamed El-Newehy. Electrospinning collagen-chitosan poly(L -lactic acid-caprolactone) to form a vascular graft: Mechanical and biological characterization. *Journal of Biomedical Materials Research Part A*, 101A(5):1292–1301, may 2013. ISSN 15493296. doi: 10.1002/jbm.a.34434. URL http://www.ncbi.nlm.nih.gov/pubmed/23065755http://doi.wiley.com/10.1002/jbm.a.34434.

[115] Giovanni S. Offeddu, Jennifer C. Ashworth, Ruth E. Cameron, and Michelle L. Oyen. Multi-scale mechanical response of freeze-dried collagen scaffolds for tissue engineering applications. *Journal of the Mechanical Behavior of Biomedical Materials*, 42:19–25, feb 2015. ISSN 17516161. doi: 10.1016/j.jmbbm.2014.10.015. URL http://www.ncbi.nlm.nih.gov/pubmed/25460922http://linkinghub.elsevier.com/retrieve/pii/S1751616114003397.

[116] Zhensheng Li, Hassna R. Ramay, Kip D. Hauch, Demin Xiao, and Miqin Zhang. Chitosan–alginate hybrid scaffolds for bone tissue engineering. *Biomaterials*, 26(18):3919–3928, jun 2005. ISSN 01429612. doi: 10.1016/j.biomaterials.2004.09.062. URL http://www.ncbi.nlm.nih.gov/pubmed/15626439http://linkinghub.elsevier.com/retrieve/pii/S0142961204009032.

[117] Stephen J. Florczyk, Matthew Leung, Zhensheng Li, Jerry I. Huang, Richard A. Hopper, and Miqin Zhang. Evaluation of three-dimensional porous chitosan-alginate scaffolds in rat calvarial defects for bone regeneration applications. *Journal of Biomedical Materials Research Part A*, 101(10):2974–2983,

oct 2013. ISSN 15493296. doi: 10.1002/jbm.a.34593. URL http://www.ncbi.nlm.nih.gov/pubmed/23737120http://doi.wiley.com/10.1002/jbm.a.34593.

[118] Zhiwei Qu, Jinglong Yan, Baoqiang Li, Jinpeng Zhuang, and Yanming Huang. Improving bone marrow stromal cell attachment on chitosan/hydroxyapatite scaffolds by an immobilized RGD peptide. *Biomedical Materials*, 5(6):065001, dec 2010. ISSN 1748-6041. doi: 10.1088/1748-6041/5/6/065001. URL http://www.ncbi.nlm.nih.gov/pubmed/20924135http://stacks.iop.org/1748-605X/5/i=6/a=065001?key=crossref.334be182745f08c70555f7cca1f00c27.

[119] Hyoung-Joon Jin, Jingsong Chen, Vassilis Karageorgiou, Gregory H Altman, and David L Kaplan. Human bone marrow stromal cell responses on electrospun silk fibroin mats. *Biomaterials*, 25(6):1039–47, mar 2004. ISSN 0142-9612. URL http://www.ncbi.nlm.nih.gov/pubmed/14615169.

[120] Mao Wang, Hyoung-Joon Jin, David L. Kaplan, and Gregory C. Rutledge. Mechanical Properties of Electrospun Silk Fibers. 2004. doi: 10.1021/MA048988V. URL http://pubs.acs.org/doi/abs/10.1021/ma048988v.

[121] In Chul Um, Dufei Fang, Benjamin S Hsiao, Akio Okamoto, and Benjamin Chu. Electro-Spinning and Electro-Blowing of Hyaluronic Acid. doi: 10.1021/bm034539b. URL http://pubs.acs.org/doi/pdf/10.1021/bm034539b.

[122] Min Soo Bae, Dae Hyeok Yang, Jung Bok Lee, Dong Nyoung Heo, Yong-Dae Kwon, In Chan Youn, Kuiwon Choi, Jong Hyun Hong, Gye Tae Kim, Yong Suk Choi, Eui Hwan Hwang, and Il Keun Kwon. Photo-cured hyaluronic acid-based hydrogels containing simvastatin as a bone tissue regeneration scaffold. *Biomaterials*, 32(32):8161–8171, nov 2011. ISSN 01429612. doi: 10.1016/j.biomaterials.2011.07.045. URL http://www.ncbi.nlm.nih.gov/pubmed/21821281http://linkinghub.elsevier.com/retrieve/pii/S0142961211008283.

[123] F Kurtis Kasper, Kazuhiro Tanahashi, John P Fisher, and Antonios G Mikos. Synthesis of poly(propylene fumarate). *Nature protocols*, 4(4):518–25, 2009. ISSN 1750-2799. doi: 10.1038/nprot.2009.24. URL http://www.ncbi.nlm.nih.gov/pubmed/19325548http://www.pubmedcentral.nih.gov/articlerender.fcgi?artid=PMC3076598.

[124] K U Lewandrowski, J D Gresser, S P Bondre, A E Silva, D L Wise, and D J Trantolo. Developing porosity of poly(propylene glycol-co-fumaric acid) bone graft substitutes and the effect on osteointegration: A preliminary histology study in rats. *Journal of Biomaterials Science, Polymer Edition*, 11(8):879–889, 2000. ISSN 0920-5063. doi: 10.1163/156856200744075. URL http://www.scopus.com/inward/record.url?eid=2-s2.0-0034534282{&}partnerID=40{&}md5=d86b2303d22b99c772df89291f350039.

[125] Yihong Gong, Zuwei Ma, Qingliang Zhou, Jun Li, Changyou Gao, and Jiacong Shen. Poly(lactic acid) scaffold fabricated by gelatin particle leaching has good biocompatibility for chondrogenesis. *Journal of biomaterials science. Polymer edition*, 19(2):207–21, 2008. ISSN 0920-5063. doi: 10.1163/156856208783432453. URL http://www.ncbi.nlm.nih.gov/pubmed/18237493.

[126] Chinnasamy Gandhimathi, Jayarama Reddy Venugopal, Allister Yingwei Tham, Seeram Ramakrishna, and Srinivasan Dinesh Kumar. Biomimetic hybrid nanofibrous substrates for mesenchymal stem cells differentiation into osteogenic cells. *Materials Science and Engineering C*, 49:776–785, 2015. ISSN 09284931. doi: 10.1016/j.msec.2015.01.075. URL http://dx.doi.org/10.1016/j.msec.2015.01.075.

[127] Shaozhi Fu, Peiyan Ni, Beiyu Wang, Bingyang Chu, Lan Zheng, Feng Luo, Jingcong Luo, and Zhiyong Qian. Injectable and thermo-sensitive PEG-PCL-PEG copolymer/collagen/n-HA hydrogel composite for guided bone regeneration. 2012. doi: 10.1016/j.biomaterials.2012.03.040. URL https://ac.els-cdn.com/S0142961212003274/1-s2.0-S0142961212003274-main.pdf?{_}tid=133543ce-ba6b-11e7-b309-00000aacb35f{&}acdnat=1509035651{_}26d31510fc8a93a0602a52c7daac80aa.

[128] Sanjukta Deb, Ramin Mandegaran, and Lucy Di Silvio. A porous scaffold for bone tissue engineering/45S5 Bioglass® derived porous scaffolds for co-culturing osteoblasts and endothelial cells. *Journal of Materials Science: Materials in Medicine*, 21(3):893–905, mar 2010. ISSN 0957-4530. doi: 10.1007/s10856-009-3936-5. URL http://link.springer.com/10.1007/s10856-009-3936-5.

[129] Lei Cai, Qian Wang, Congmin Gu, Jingguo Wu, Jian Wang, Ning Kang, Jiewei Hu, Fang Xie, Li Yan, Xia Liu, Yilin Cao, and Ran Xiao. Vascular and micro-environmental influences on MSC-coral hydroxyapatite construct-based bone tissue engineering. *Biomaterials*, 32(33):8497–8505, nov 2011. ISSN 01429612. doi: 10.1016/j.biomaterials.2011.07.087. URL http://www.ncbi.nlm.nih.gov/pubmed/21855129http://linkinghub.elsevier.com/retrieve/pii/S0142961211008842.

[130] E Damien and P A Revell. Coralline hydroxyapatite bone graft substitute: A review of experimental studies and biomedical applications. *Journal of applied biomaterials & biomechanics : JABB*, 2(2):65–73. ISSN 1722-6899. URL http://www.ncbi.nlm.nih.gov/pubmed/20803439.

[131] C E Wen, M Mabuchi, Y Yamada, K Shimojima, Y Chino, and T Asahina. Processing of biocompatible porous Ti and Mg. URL https://ac.els-cdn.com/S1359646201011320/1-s2.0-S1359646201011320-main.pdf?{_}tid=53bb9de8-ba67-11e7-976f-00000aacb35e{&}acdnat=1509034041{_}facbc83a0fd1a597f1af5fcce78f0339.

[132] Johan Van der Stok, Olav P. Van der Jagt, Saber Amin Yavari, Mirthe F. P. De Haas, Jan H. Waarsing, Holger Jahr, Esther M. M. Van Lieshout, Peter Patka, Jan A. N. Verhaar, Amir A. Zadpoor, and Harrie Weinans. Selective laser melting-produced porous titanium scaffolds regenerate bone in critical size cortical bone defects. *Journal of Orthopaedic Research*, 31(5):792–799, may 2013. ISSN 07360266. doi: 10.1002/jor.22293. URL http://doi.wiley.com/10.1002/jor.22293.

[133] J D Bobyn, G J Stackpool, S A Hacking, Meng J J Krygier, Cet Jo Miller, M Tanzer, and J J Krygier. Characteristics of bone ingrowth and interface mechanics of a new porous tantalum biomaterial. *Bone Joint Surg [Br]*, 81(5):907–14, 1999. URL http://bjj.boneandjoint.org.uk/content/jbjsbr/81-B/5/907.full.pdf.

[134] Fang Yang, Sanne K Both, Xuechao Yang, X Frank Walboomers, and John A Jansen. Development of an electrospun nano-apatite/PCL composite membrane for GTR/GBR application. 2009. doi: 10.1016/j.actbio.2009.05.023. URL https://ac.els-cdn.com/S1742706109002281/1-s2.0-S1742706109002281-main.pdf?{_}tid=0cc56b5a-ba6f-11e7-a1fe-00000aacb35f{&}acdnat=1509037358{_}330936bd7f5dca859e9c84fa84800f72.

[135] WahWah Thein-Han and Hockin H.K. Xu. Collagen-Calcium Phosphate Cement Scaffolds Seeded with Umbilical Cord Stem Cells for Bone Tissue Engineering. *Tissue Engineering Part A*, 17(23-24):2943–2954, dec 2011. ISSN 1937-3341. doi: 10.1089/ten.tea.2010.0674. URL http://www.ncbi.nlm.nih.gov/pubmed/21851269http://www.pubmedcentral.nih.gov/articlerender.fcgi?artid=PMC3226062http://www.liebertonline.com/doi/abs/10.1089/ten.tea.2010.0674.

[136] ND Evans, C Minelli, E Gentleman, V LaPointe, SN Patankar, M Kallivretaki, X Chen, CJ Roberts, and MM Stevens. Substrate stiffness affects early differentiation events in embryonic stem cells. *European Cells and Materials*, 18:1–14, sep 2009. doi: 10.22203/eCM.v018a01. URL http://ecmjournal.org/journal/papers/vol018/pdf/v018a01.pdf.

[137] P. M. Gilbert, K. L. Havenstrite, K. E. G. Magnusson, A. Sacco, N. A. Leonardi, P. Kraft, N. K. Nguyen, S. Thrun, M. P. Lutolf, and H. M. Blau. Substrate Elasticity Regulates Skeletal Muscle Stem Cell Self-Renewal in Culture. *Science*, 329(5995):1078–1081, aug 2010. ISSN 0036-8075. doi: 10.1126/science.1191035. URL http://www.ncbi.nlm.nih.gov/pubmed/20647425http://www.pubmedcentral.nih.gov/articlerender.fcgi?artid=PMC2929271http://www.sciencemag.org/cgi/doi/10.1126/science.1191035.

[138] R J Pelham and Y l Wang. Cell locomotion and focal adhesions are regulated by substrate flexibility. *Proceedings of the National Academy of Sciences of the United States of America*, 94(25):13661–5, dec 1997. ISSN 0027-8424. URL http://www.ncbi.nlm.nih.gov/pubmed/9391082http://www.pubmedcentral.nih.gov/articlerender.fcgi?artid=PMC28362.

[139] Aurore Schneider, Grégory Francius, Rodolphe Obeid, Pascale Schwinté, Joseph Hemmerlé, Benoît Frisch, Pierre Schaaf, Jean-Claude Voegel, Bernard Senger, and Catherine Picart. Polyelectrolyte Multilayers with a Tunable Young's Modulus: Influence of Film Stiffness on Cell Adhesion. *Langmuir*, 22(3):1193–1200, jan 2006. ISSN 0743-7463. doi: 10.1021/la0521802. URL http://www.ncbi.nlm.nih.gov/pubmed/16430283http://pubs.acs.org/doi/abs/10.1021/la0521802.

[140] Rowena McBeath, Dana M Pirone, Celeste M Nelson, Kiran Bhadriraju, and Christopher S Chen. Cell shape, cytoskeletal tension, and RhoA regulate stem cell lineage commitment. *Developmental cell*, 6 (4):483–95, apr 2004. ISSN 1534-5807. URL http://www.ncbi.nlm.nih.gov/pubmed/15068789.

[141] H B Wang, M Dembo, and Y L Wang. Substrate flexibility regulates growth and apoptosis of normal but not transformed cells. *American journal of physiology. Cell physiology*, 279(5):C1345–50, nov 2000. ISSN 0363-6143. URL http://www.ncbi.nlm.nih.gov/pubmed/11029281.

[142] Tony Yeung, Penelope C. Georges, Lisa A. Flanagan, Beatrice Marg, Miguelina Ortiz, Makoto Funaki, Nastaran Zahir, Wenyu Ming, Valerie Weaver, and Paul A. Janmey. Effects of substrate stiffness on cell morphology, cytoskeletal structure, and adhesion. *Cell Motility and the Cytoskeleton*, 60(1):24–34, jan 2005. ISSN 0886-1544. doi: 10.1002/cm.20041. URL http://www.ncbi.nlm.nih.gov/pubmed/15573414http://doi.wiley.com/10.1002/cm.20041.

[143] Tao Zhang, Shiyu Lin, Xiaoru Shao, Sirong Shi, Qi Zhang, Changyue Xue, Yunfeng Lin, Bofeng Zhu, and Xiaoxiao Cai. Regulating Osteogenesis and Adipogenesis in Adipose-Derived Stem Cells by Controlling Underlying Substrate Stiffness. *Journal of Cellular Physiology*, sep 2017. ISSN 00219541. doi: 10.1002/jcp.26193. URL http://www.ncbi.nlm.nih.gov/pubmed/28926111http://doi.wiley.com/10.1002/jcp.26193.

[144] Nick J. Walters and Eileen Gentleman. Evolving insights in cell–matrix interactions: Elucidating how non-soluble properties of the extracellular niche direct stem cell fate. *Acta Biomaterialia*, 11:3–16, jan 2015. ISSN 17427061. doi: 10.1016/j.actbio.2014.09.038. URL http://linkinghub.elsevier.com/retrieve/pii/S1742706114004292.

[145] Adam J. Engler, Shamik Sen, H. Lee Sweeney, and Dennis E. Discher. Matrix Elasticity Directs Stem Cell Lineage Specification. *Cell*, 126(4):677–689, aug 2006. ISSN 00928674. doi: 10.1016/j.cell.2006.06.044. URL http://www.ncbi.nlm.nih.gov/pubmed/16923388http://linkinghub.elsevier.com/retrieve/pii/S0092867406009615.

[146] A. S. Rowlands, P. A. George, and J. J. Cooper-White. Directing osteogenic and myogenic differentiation of MSCs: interplay of stiffness and adhesive ligand presentation. *AJP: Cell Physiology*, 295(4):C1037–C1044, oct 2008. ISSN 0363-6143. doi: 10.1152/ajpcell.67.2008. URL http://www.ncbi.nlm.nih.gov/pubmed/18753317http://ajpcell.physiology.org/cgi/doi/10.1152/ajpcell.67.2008.

[147] Akhilesh Banerjee, Manish Arha, Soumitra Choudhary, Randolph S Ashton, Surita R Bhatia, David V Schaffer, and Ravi S Kane. The influence of hydrogel modulus on the proliferation and differentiation of encapsulated neural stem cells. *Biomaterials*, 30(27):4695–9, sep 2009. ISSN 1878-5905. doi: 10.1016/j.biomaterials.2009.05.050. URL http://www.ncbi.nlm.nih.gov/pubmed/19539367http://www.pubmedcentral.nih.gov/articlerender.fcgi?artid=PMC2743317.

[148] Vassilis Karageorgiou and David Kaplan. Porosity of 3D biomaterial scaffolds and osteogenesis. *Biomaterials*, 26(27):5474–5491, 2005. ISSN 01429612. doi: 10.1016/j.biomaterials.2005.02.002.

[149] Sara M. Mantila Roosa, Jessica M. Kemppainen, Erin N. Moffitt, Paul H. Krebsbach, and Scott J. Hollister. The pore size of polycaprolactone scaffolds has limited influence on bone regeneration in an in vivo model. *Journal of Biomedical Materials Research Part A*, 92A(1):359–368, jan 2010. ISSN 15493296. doi: 10.1002/jbm.a.32381. URL http://www.ncbi.nlm.nih.gov/pubmed/19189391http://doi.wiley.com/10.1002/jbm.a.32381.

[150] Y. Kuboki, H. Takita, D. Kobayashi, E. Tsuruga, M. Inoue, M. Murata, N. Nagai, Y. Dohi, and H. Ohgushi. BMP-Induced osteogenesis on the surface of hydroxyapatite with geometrically feasible and nonfeasible structures: Topology of osteogenesis. *Journal of Biomedical Materials Research*, 39(2):190–199, feb 1998. ISSN 0021-9304. doi: 10.1002/(SICI)1097-4636(199802)39:2<190::AID-JBM4>3.0.CO;2-K. URL http://doi.wiley.com/10.1002/{%}28SICI{%}291097-4636{%}28199802{%}2939{%}3A2{%}3C190{%}3A{%}3AAID-JBM4{%}3E3.0.CO{%}3B2-K.

[151] B J Story, W R Wagner, D M Gaisser, S D Cook, and A M Rust-Dawicki. In vivo performance of a modified CSTi dental implant coating. *The International journal of oral & maxillofacial implants*, 13(6):749–57. ISSN 0882-2786. URL http://www.ncbi.nlm.nih.gov/pubmed/9857585.

[152] J Vlacic-Zischke, S M Hamlet, T Friis, M S Tonetti, and S Ivanovski. The influence of surface microroughness and hydrophilicity of titanium on the up-regulation of TGFβ/BMP signalling in osteoblasts. *Biomaterials*, 32(3):665–71, jan 2011. ISSN 1878-5905. doi: 10.1016/j.biomaterials.2010.09.025. URL http://www.ncbi.nlm.nih.gov/pubmed/20933273.

[153] O. Chan, M.J. Coathup, A. Nesbitt, C.-Y. Ho, K.A. Hing, T. Buckland, C. Campion, and G.W. Blunn. The effects of microporosity on osteoinduction of calcium phosphate bone graft substitute biomaterials. *Acta Biomaterialia*, 8(7):2788–2794, jul 2012. ISSN 17427061. doi: 10.1016/j.actbio.2012.03.038. URL http://www.ncbi.nlm.nih.gov/pubmed/22475784http://linkinghub.elsevier.com/retrieve/pii/S174270611200133X.

[154] Philip Kasten, Ingo Beyen, Philipp Niemeyer, Reto Luginbühl, Marc Bohner, and Wiltrud Richter. Porosity and pore size of β-tricalcium phosphate scaffold can influence protein production and osteogenic differentiation of human mesenchymal stem cells: An in vitro and in vivo study. *Acta Biomaterialia*, 4(6):1904–1915, nov 2008. ISSN 17427061. doi: 10.1016/j.actbio.2008.05.017. URL http://www.ncbi.nlm.nih.gov/pubmed/18571999http://linkinghub.elsevier.com/retrieve/pii/S1742706108001608.

[155] S. F. Hulbert, F. A. Young, R. S. Mathews, J. J. Klawitter, C. D. Talbert, and F. H. Stelling. Potential of ceramic materials as permanently implantable skeletal prostheses. *Journal of Biomedical Materials Research*, 4(3):433–456, sep 1970. ISSN 0021-9304. doi: 10.1002/jbm.820040309. URL http://doi.wiley.com/10.1002/jbm.820040309.

[156] A. K. M. B. Khoda, Ibrahim T Ozbolat, and Bahattin Koc. Engineered Tissue Scaffolds With Variational Porous Architecture. *Journal of Biomechanical Engineering*, 133(1):011001, dec 2010. ISSN 0148-0731. doi: 10.1115/1.4002933. URL http://www.ncbi.nlm.nih.gov/pubmed/21186891http://biomechanical.asmedigitalcollection.asme.org/article.aspx?doi=10.1115/1.4002933.

[157] Serge Kobsa and W Mark Saltzman. Bioengineering Approaches to Controlled Protein Delivery PROBLEMS EXIST IN DELIVERY OF BIOACTIVE AGENTS. URL https://www.nature.com/pr/journal/v63/n5/pdf/pr2008103a.pdf?origin=ppub.

[158] Soo-Hong Lee and Heungsoo Shin. Matrices and scaffolds for delivery of bioactive molecules in bone and cartilage tissue engineering. 2007. doi: 10.1016/j.addr.2007.03.016. URL https://ac.els-cdn.com/S0169409X07000324/1-s2.0-S0169409X07000324-main.pdf?{_}tid=81c67390-b8ee-11e7-896d-00000aab0f27{&}acdnat=1508872199{_}cfd04919f7fcc7c97da011b6731f63af.

[159] Zhichao Zhang, Qingguo Lai, Yanan Li, Chao Xu, Xiaopeng Tang, Jiangbo Ci, Shaolong Sun, Bingbing Xu, and Yan Li. Acidic pH environment induces autophagy in osteoblasts. *Scientific Reports*, 7(April):1–9, 2017. ISSN 20452322. doi: 10.1038/srep46161. URL http://dx.doi.org/10.1038/srep46161.

[160] Felix Kurth, Klaus Eyer, Alfredo Franco-Obregón, and Petra S. Dittrich. A new mechanobiological era: Microfluidic pathways to apply and sense forces at the cellular level. *Current Opinion in Chemical Biology*, 16(3-4):400–408, 2012. ISSN 13675931. doi: 10.1016/j.cbpa.2012.03.014.

[161] Peter M. Govey, Alayna E. Loiselle, and Henry J. Donahue. Biophysical regulation of stem cell differentiation. *Current Osteoporosis Reports*, 11(2):83–91, 2013. ISSN 15441873. doi: 10.1007/s11914-013-0138-3.

[162] Shoji Maruo and John T. Fourkas. Recent progress in multiphoton microfabrication. *Laser and Photonics Reviews*, 2(1-2):100–111, 2008. ISSN 18638880. doi: 10.1002/lpor.200710039.

[163] Christopher N. LaFratta and Tommaso Baldacchini. Two-photon polymerization metrology: Characterization methods of mechanisms and microstructures. *Micromachines*, 8(4), 2017. ISSN 2072666X. doi: 10.3390/mi8040101.

[164] Enrico Domenico Lemma, Francesco Rizzi, Tommaso Dattoma, Barbara Spagnolo, Leonardo Sileo, Antonio Qualtieri, Massimo De Vittorio, and Ferruccio Pisanello. Mechanical Properties Tunability of Three-Dimensional Polymeric Structures in Two-Photon Lithography. *IEEE Transactions on Nanotechnology*, 16(1):23–31, 2017. ISSN 1536125X. doi: 10.1109/TNANO.2016.2625820.

[165] Daraio Research Group at Caltech. URL http://www.daraio.caltech.edu/facilities.html.

[166] IP Photoresists - Nanoscribe GmbH. URL https://www.nanoscribe.de/en/products/ip-photoresists/.

[167] Charalampos Schizas and Dimitris Karalekas. Mechanical characteristics of an Ormocomp® biocompatible hybrid photopolymer. *Journal of the Mechanical Behavior of Biomedical Materials*, 4(1):99–106, jan 2011. ISSN 17516161. doi: 10.1016/j.jmbbm.2010.09.010. URL http://www.ncbi.nlm.nih.gov/pubmed/21094483http://linkinghub.elsevier.com/retrieve/pii/S1751616110001335.